Title

Functional genomic and profiling approaches to characterize mammalian immunity

Permalink

https://escholarship.org/uc/item/5hn3w7t2

Author

Mowery, Cody

Publication Date

2023

Peer reviewed|Thesis/dissertation

Functional genomic and profiling approaches to characterize mammalian immunity

by
Cody Mowery

DISSERTATION
Submitted in partial satisfaction of the requirements for degree of
DOCTOR OF PHILOSOPHY

in

Biomedical Sciences

in the

GRADUATE DIVISION
of the
UNIVERSITY OF CALIFORNIA, SAN FRANCISCO

Approved:

DocuSigned by:

Mark Anderson
657D61B3C699406...

Mark Anderson

Chair

DocuSigned by:

Alexander Marson
...C4A8...

Alexander Marson

DocuSigned by:

Chun Ye
...429...

Chun Ye

DocuSigned by:

Matthew Spitzer
4793AE6232BE479...

Matthew Spitzer

Committee Members

Dedication

This dissertation is as much my family's as it is my own.

In memory of my father, Don R. Mowery, whose wonder and curiosity in the natural world gave

root to mine.

Acknowledgements

There are innumerable people to thank for supporting and sustaining me at various stages of my training. First, I am eternally grateful to Alexander Marson MD PhD and Jimmie Ye PhD for jointly serving as my PhD advisors. Even before I started my PhD and committed to train in their respective labs, both Alex and Jimmie availed themselves for career mentorship and advice. Then, they formally welcomed me – a trainee with little experience directly relevant to either of their research programs – into their labs and supported my (often scattered) scientific interests. Both have built communities of incredible scientists who strive to understand human immunity and inspire new immunotherapeutics through deep molecular understanding of relevant immunological and genetic processes. By fostering such collegial scientific environments, both Alex and Jimmie provided me with the opportunity to explore my scientific curiosities; challenged me to rethink my assumptions; inspired me to strive for deeper understanding; and encouraged me to do so with rigor, integrity, and open collaboration. Importantly, they reminded me to have fun along the way. Thank you both.

I also want to thank the remainder of my thesis committee: Matthew Spitzer PhD and my thesis chair Mark Anderson MD PhD. I wholly appreciate their time, feedback, and inspiration through the entirety of my PhD, even before formally serving on my committee. Matt is amongst the most supportive and encouraging mentors I've ever had. Mark helped contextualize my graduate training within my broader MD/PhD path and did so with deep care and compassion. Furthermore, as MSTP Director through the first half of my training, Mark played a central role in my matriculation at UCSF. I will forever be grateful to him and the remainder of the admissions committee for giving me the opportunity to realize my dream of becoming a physician-scientist. Lastly, I would like to thank Qizhi Tang PhD and Luke Gilbert PhD for serving on my qualifying committee, helping me establish a firm foundation from which the rest of my graduate training would subsequently develop.

To my family, old and new… Although we lost him decades ago, my dad was with me every day of my PhD. His perseverance, insatiable hunger for understanding, and ability to find joy in the seemingly unenjoyable underlie my own. Whenever I was tired or uninspired, I looked to my mom for inspiration. No dissertation of infinite length could accommodate the tome of recognition she deserves, so I'll keep it brief… Thank you mom for your spirit, support, and demonstration of human kindness that I will forever strive to match. I am grateful to my brothers, Corey and Casey, for their unyielding support and regular reminder that I should graduate already. I am also grateful to those who my brothers have brought into our family – Brittany and Amy – for providing additional love and energy. To my niece, Kaylynn: I hope this degree inspires you to pursue your own goals (no matter how many years of schooling might be required) and make the world a better place along the way. I am grateful to Stan and the rest of the Jones family for further enriching my own. Lastly, I thank Lisa, Angelo, and Chris Vlessis for welcoming me into their family with love, open arms, great wine, and rainbow Crocs.

To Kate: I am disappointed I will never be able to fully convey my love, respect, and appreciation for you. I count myself lucky to be able to rely on you for more than I – one who prides himself in independence and self-sufficiency – would care to admit. Your brilliance and perspective have kept me going, so this degree is as much yours as it is mine. Every part of my life is better with you in it, from the mundane to the most exciting, so I cannot wait to see what comes next.

Contributions to Presented Works

This dissertation was prepared under the direct supervision and guidance of Alexander Marson MD PhD and Jimmie Ye PhD. Dr. Marson, Dr. Ye and I secured funding for this work, with additional funding sources and contributions noted in their respective chapters below.

Chapter 2 is published as **Cody T. Mowery***, Jeffrey D. Whitman*, Joseph Hiatt*, Brian R. Shy*, Ruby Yu*, Tori N. Yamamoto, Ujjwal Rathore, Gregory M. Goldgof, Caroline Whitty, Jonathan M. Woo, Antonia E. Gallman, Tyler E. Miller, Andrew G. Levine, David N. Nguyen, Sagar P. Bapat, Joanna Balcerek, Sophia A. Bylsma, Ana M. Lyons, Stacy Li, Allison Wai-yi Wong, Eva Mae Gillis-Buck, Zachary B. Steinhart, Youjin Lee, Ryan Apathy, Mitchell J. Lipke, Jennifer Anne Smith, Tina Zheng, Ian C. Boothby, Erin Isaza, Jackie Chan, Dante D. Acenas, Jinwoo Lee, Trisha A. Macrae, Than S. Kyaw, David Wu, Dianna L. Ng, Wei Gu, Vanessa A. York, Haig Alexander Eskandarian, Perri C. Callaway, Lakshmi Warrier, Mary E. Moreno, Justine Levan, Leonel Torres, Lila A. Farrington, Rita P. Loudermilk, Kanishka Koshal, Kelsey C. Zorn, Wilfredo F. Garcia-Beltran, Diane Yang, Michael G. Astudillo, Bradley E. Bernstein, Jeffrey A. Gelfand, Edward T. Ryan, Richelle C. Charles, A. John Iafrate, Jochen K. Lennerz, Steve Miller , Charles Y. Chiu, Susan L. Stramer, Michael R. Wilson, Aashish Manglik, Chun Jimmie Ye, Nevan J. Krogan, Mark S. Anderson, Jason G. Cyster, Joel D. Ernst, Alan H. B. Wu , Kara L. Lynch, Caryn Bern[#], Patrick D. Hsu[#] and Alexander Marson[#]. Evaluation of SARS-CoV-2 serology assays reveals a range of test performance. *Nature Biotechnology*, 2020. C.T.M is a co-first author together with J.D.W., J.H., B.R.S., and R.Y. All co-first authors collaboratively led study design, acquisition of serology tests, data collection and analysis, and manuscript preparation. A.M. and P.D.H conceptualized the study. A.M., P.D.H, and C.B. supervised the work, including manuscript preparation, and contributed funding. T.N.Y, U.R., C.W., J.M.W., A.E.G., S.A.B., A.M.L., S.L., A.W.W., E.M.G.B., Z.B.S., Y.L., R.A., M.J.L., J.A.S., T.Z., I.C.B., E.I, J.C., D.D.A, J.L., T.A.M., T.S.K., D.W., D.L.N., W.G., V.A.Y., H.A.E., P.C.C., L.W., M.E.M, J.L., L.T., L.F., R.L. K.K., and K.C.Z. were involved in

data collection. G.M.G., A.G.L., D.N.N., S.P.B., J.B., S.B. contributed chart review. S.M., C.Y.C., S.L.S., M.R.W., A.M., C.J.Y., N.J.K., M.S.A., J.G.C, J.D.E., A.H.B.W, and K.L.L. supervised UCSF co-authors. T.E.M., W.F.G.B., D.Y., M.G.A., B.E.B, J.A.G, E.T.R, R.C.C., A.J.I., and J.K.L. contributed to study design, data collection, and analysis of the portion of this work performed at Massachusetts General Hospital. All authors reviewed the manuscript.

Chapter 3 is publicly available as **Cody T. Mowery,** Alexander Marson, Yun S. Song, Chun Jimmie Ye. Improved COVID-19 Serology Test Performance by Integrating Multiple Lateral Flow Assays using Machine Learning. *medRxiv,* 2020. C.T.M., Y.S.S., and C.J.Y. conceptualized the study. C.T.M. and Y.S.S. performed the computational analyses. A.M., Y.S.S., and C.J.Y. supervised the data analysis and provided funding. C.T.M., A.M., Y.S.S., and C.J.Y. prepared the manuscript.

Chapter 4 is under review as **Cody T. Mowery**, Jacob W. Freimer, Zeyu Chen, Salvador Casaní-Galdón, Christian M. Garrido, Benjamin G. Gowen, Vinh Nguyen, Dimitre R. Simeonov, Gemma L. Curie, Jennifer M. Umhoefer, Ralf Schmidt, Zachary Steinhart, Maya M. Arce, Jacob E. Corn, Bradley E. Bernstein, Chun Jimmie Ye & Alexander Marson. Systematic decoding of *cis* gene regulation defines context-dependent control of the multi-gene costimulatory receptor locus in human T cells. C.T.M. and A.M. conceptualized the study. C.T.M. conducted all CRISPRi screens with support from J.M.U., R.S., Z.S., M.M.A., and V.N. J.W.F. and C.M.G. performed *trans* regulator screens, and C.T.M. and J.W.F. performed the subsequent data analyses. Z.C. and S.C-G. performed the 4C-Seq data collection and analysis. B.G.G., D.R.S., and G.L.C. designed and cloned the tiling sgRNA library. C.T.M. performed all other experimentation. J.E.C., B.E.B., C.J.Y., and A.M. supervised authors and provided funding and resources. C.T.M. prepared the manuscript. C.T.M., C.J.Y., and A.M. reviewed and edited the manuscript.

The impulses, ambitions, fantasies, and desires that drive human history are, at least in part, encoded in the human genome. And human history has, in turn, selected genomes that carry these impulses, ambitions, fantasies, and desires. This self-fulfilling circle of logic is responsible for some of the most magnificent and evocative qualities in our species, but also some of the most reprehensible. It is far too much to ask ourselves to escape the orbit of this logic, but recognizing its inherent circularity, and being skeptical of its overreach, might protect the weak from the will of the strong, and the 'mutant' from being annihilated by the 'normal.'

– Siddhartha Mukherjee, *The Gene: An Intimate History*

Functional genomic and profiling approaches to characterize mammalian immunity

Cody T. Mowery

Abstract

The immune system persists in a sensitive equilibrium, necessarily avoiding overreaction to illegitimate threats while watchfully waiting for any *bona fide* harms that might come along. Fortunately, myriad cell extrinsic and intrinsic mechanisms have evolved to fortify this steady state. Amongst these regulatory forces, three distinct yet interdependent signals lie at the heart of immune activation. The first signal – engagement of the B or T cell receptor by cognate antigen – has significant diagnostic and therapeutic potential. After the emergence of SARS-CoV-2 and its associated clinical syndrome, COVID-19, we led a nationwide, multi-disciplinary scientific and clinical team to systematically benchmark numerous serological assays testing for effective "signal 1" responsiveness to SARS-CoV-2-associated antigens. Establishing accuracy of these tests had significant implications on governmental policies relating to the pandemic, as well as efforts to employ these serology tests to understand COVID-19 seroprevalence and protective immunity. Next, we applied computational tools to improve the performance of these serological tests through combinatorial application and companion analyses. Lastly, we followed these studies of serology diagnostics (corresponding to signal 1) with systematic molecular studies of costimulation: the second signal influencing T cell activation. This critical next step is indispensable to immune responsiveness, but the intricacies of regulatory factors influencing each step have yet to be systematically studied. Our labs have pioneered the use of functional genomic screening using CRISPR/Cas9 to thoroughly explore the regulatory landscape of various immunological phenotypes. Thus, we leveraged recent molecular advances to functionally define the *cis* and *trans* regulators converging on the human costimulatory locus harboring *CD28*, *CTLA4*, and *ICOS* at scale. This work uncovered gene-, cell subset-, and stimulation-specific *cis*-regulatory elements (CREs) bound by validated *trans* regulators to influence costimulatory gene expression. Finally, deep characterization of genomic architecture in the locus defined critical insulator elements

reinforcing CRE activation of true targets while also preventing spurious activation of flanking genes. Ultimately, similar demonstrations of collaborative science to study the human immune system whether in the form of fundamental genomic immunology or translational immune diagnostics will aid our collective transition to the next generation of more precise biomedicine.

Table of Contents

<h1 style="text-align: center">List of Figures</h1>

List of Tables

Chapter 1: Introduction

When I first started my graduate training in 2018, scientific fields like immunology and genomics were rarely featured in public discourse. This was little more than five years ago, but one pandemic separates then and now. After the global emergence of and wreaking havoc by SARS-CoV-2 – the virus that causes COVID-19 – lay discussions about "IgG" and "PCR assays" and "serology tests" abound. Three years and more than 6.5 million tragic deaths later[1], the public's relationship with science has taken a new form. Scientific innovation and advancement, as demonstrated by the rapid development of mRNA-based primary and booster vaccines[2], can be largely credited with protecting the more than 670 million people who survived SARS-CoV-2 infection[1]. At the same time, this shared global experience revealed just how much the scientific community has yet to fully understand about human (and non-human) biology. Provided its centrality in defending against pathogens like SARS-CoV-2, the immune system has been largely center stage in this discussion.

1.1: The role of immunity in maintaining host homeostasis

Immunology Is Where Intuition Goes to Die

– Ed Yong, The Atlantic

The immune system acquired inconceivable complexity as a byproduct of its evolution to fend off an exceedingly diverse array of physiologic threats – complexity that underlies refrains like Ed Yong's above. This intricacy takes many forms, from innumerous cell types engaged in infinite intercellular interactions, to the tremendous number of cell receptors and secreted signaling proteins (all with obligatorily obscure names) that mediate these interactions. However, scientists – graduate students and more trained professionals, alike – are charged with simultaneously adding to this complexity via discovery of new immunological intricacies while also reducing the confusion through principled, mechanistic characterization of relevant biological

1

processes. Yet, the very best and most impactful scientific projects answer some questions while illuminating untold others, sustaining this cycle of unknowing and discovery in perpetuity.

In its simplest form, the immune system is often reduced to a security force that protects the body from foreign organisms like viruses (like SARS-CoV-2) and bacteria[3]. However, there is growing appreciation for the immune system's role in clearing other threats like malignant[4] and aging[5] cells as well. Regardless of the threat at hand, the immune system exerts its effects through the concerted and highly orchestrated effort of myriad cell types: from "innate" cells like macrophages and dendritic cells, to B and T cells of the "adaptive" immune system. Consider what happens when someone is infected with SARS-CoV-2 and goes on to develop COVID-19. Innate cells are first to respond, critically sopping up any competent virus and viral-associated antigens floating around. In parallel, innate cells release chemokine signals to recruit adaptive cells to come and bolster the defenses[3]. The intricacies of these processes are beyond the scope of this dissertation, other than to emphasize that we simultaneously understand a lot and exceedingly little.

Of the multitude of scientific problems one can tackle in graduate school, the labyrinthine processes of the adaptive immune system generated the strongest gravitational force that ultimately drew me in. We know this subset of immunity serves myriad roles, from providing immunological backup to innate cells to also establishing "memory" for more rapid and robust response to the same pathogen in any future reencounter[3], but we have yet to fully understand how they do so with sufficient sensitivity, specificity, and control. To this end, my graduate work was dedicated to better understanding the functioning and molecular regulation of the adaptive immune system.

1.2: T and B cell receptor analyses to understand immune function

Cells interact with their environment via a multitude of cell surface receptors. Adaptive immune cells like B and T cells are no exception, with their aptly named B and T cell receptors

(or BCRs and TCRs, respectively) serving the critical role of reserving immune activation for only select stimuli that warrant response. The beauty of biological intricacy is on full display with BCR and TCR development and functioning. DNA mutations often have deleterious effects, disrupting gene expression in ways that can induce cellular dysfunction and/or oncogenesis, but adaptive immune cells are a unique exception: they *intentionally* rearrange their genomes to alter their respective receptors through a process functionally distinct from the acquisition of pathogenic DNA mutations (although mutations in these cells outside the BCR/TCR loci can cause B or T cell cancers). These self-improvement processes enhance the ability of B and T cells to target biological abnormalities sensitively and specifically[6] (e.g., microbe-infected cells, tumor cells, etc.), picking up where the innate immune system left off.

Since their discovery and molecular cloning in the 1980's, T and B cell receptors (as well as the optimized and secreted form of BCRs, known as antibodies) have yielded tremendous scientific and therapeutic value. Efforts to better understand fundamental T and B cell receptor biology, as well as developing methods to engineer these receptors for greater curative potential, remain exciting scientific arenas I hope to explore in the future. In particular, I am motivated to build molecular tools to meet the growing demand for functional screening of B and T cell receptors as brought upon us by single cell RNA sequencing methodologies with TCR and BCR characterization[7], of which the Ye Lab is particularly well known for. Scalable methods to molecularly construct BCR/TCR libraries would enable high-throughput screening to answer fundamental biological questions with significant potential for clinical translational impact. While select methods have been published to this end[8,9], they are insufficient in either their throughput or ability to select specific receptor sets for follow up screening. Both T cell receptors and antibody-derived chimeric antigen receptors (CARs) have given hope to cancer patients who had thus far failed conventional treatments[10,11], though significant work remains to both optimize and democratize these novel therapeutics. Thus, future work in molecular methods for immune

repertoire discovery, characterization, and therapeutic engineering could usher in the next generation of immunotherapeutics for a variety of clinical indications.

Other opportunities besides engineered cell therapies exist to leverage immune repertoire characterization for clinical utility. For example, the exquisite sensitivity of antibodies to bind and (ideally) neutralize a specific foreign antigen can be leveraged for diagnostic assays. Thus, quantitative and/or qualitative serology assays that detect antigen-specific antibodies in patients' blood are helpful to infer whether a patient might be protected from the specific antigenic threat of interest. These assays took center-stage for a period early in the COVID-19 pandemic. Prior to the authorization of vaccines for public use[12], many hoped that prior infection with SARS-CoV-2 would confer immunity that would enable protected citizens' reentry into a society still largely plagued by the viral threat. At this time, shelter-in-place orders and workplace restrictions kept all but the most essential workers largely confined to our homes. **Chapter 2** describes collaborative work I co-led to benchmark an array of blood tests rapidly developed to determine individuals' antibody protection against SARS-CoV-2, a readout that many hoped would enable their safe return to normalcy. Whereas much of our basic science research takes decades (optimistically) to translate to patient care, this work had more immediate impact: it was cited by the House Oversight Committee in their investigation into the FDA's handling of SARS-CoV-2 serology test authorization[13], was directly responsible for the withdrawal of a number of underperforming tests from the market[14], and served as a framework for the FDA's serology testing effort moving forward[15]. We built on this work by examining combinatorial test pairs with ML-enabled analysis, as outlined in **Chapter 3**. In addition to my volunteering at the Chan-Zuckerberg BioHub's CLIA lab for SARS-CoV-2 infection testing[16,17], the work presented in **Chapters 2 and 3** were welcomed opportunities to contribute to our collective, global response to this unprecedented pandemic. These works also serve to reaffirm the power of team science, with our projects bringing together groups from UCSF, Zuckerberg San Francisco General Hospital, UC Berkeley, and Massachusetts General Hospital to conduct the work and inform serology testing efforts moving

forward. Lastly, while these works were translational in nature, they are predicated on the basic facts of fundamental immunology: the adaptive immune system is so sensitive, so finely tuned to specific target antigens, that we can leverage molecular and biochemical assays to measure patients' immune responsiveness to pathogenic threats.

1.3: Functional genomic approaches to characterize immune gene regulation

While the B and T cell receptors are critical gatekeepers to immune activation, the maintenance of immune homeostasis more broadly is largely governed by other factors. In T cells, significant regulatory activity is exerted by the CD28-family members CD28, CTLA4, and ICOS[18]. CD28 engagement by its ligands, CD80 and CD86, constitutes a co-stimulatory "signal 2" to drive activation alongside TCR signaling. Conversely, CTLA4 exerts a negative effect on T cell costimulation via increased affinity, and thus competition, for CD80 and CD86. Lastly, ICOS offers an orthogonal yet insufficient activating signal that influences T cell differentiation upon binding of its distinct ligand (ICOSL). The integration of these three signals largely dictates the functional outcome of TCR engagement, from reversion to an anergic state to full activation. Fascinatingly, these three genes are believed to have emerged through evolutionary duplication of a single ancestral *CD28* gene[19]. Evolutionary pressures are constantly shaping the human genome[20], altering the distribution of genetic variations both small and large that shape gene expression more broadly. Given the critical immune function of the CD28 gene family, particularly how its regulatory activities are wholly intertwined with TCR functioning, we wanted to systematically characterize how *CD28*, *CTLA4*, and *ICOS* are regulated.

My fascination in gene regulation arose from the fundamentality of it, with the dogmatic procession of DNA deriving RNA which is translated into protein lying at the core of all of biology. Although there are select exceptions to this Central Dogma[21] of biology (namely, retroviruses that convert RNA genomes to DNA ones[22]), the DNA genome encodes the full instruction manual for life. In one form, the protein encoded by one gene can alter the expression of another gene in

trans. These transcription factors are largely responsible for cell-specific transcriptional programs that shape function, stimuli response, and other cellular activities[23]. Interestingly, nearby DNA regions can alter gene expression in *cis*[24]. This enigmatic biological phenomenon has long held my interest, driving my curiosity how the >98% of the DNA genome that does not encode the instructions to make functional proteins influences the remaining <2% that does. Non-coding DNA regions like enhancers interact with gene target(s) via complex 3D looping of the genome within topologically associating domains (TADs) that are structurally confined by insulating protein complexes composed of CTCF and cohesin[25]. This multi-layered organization of gene regulation critically governs which enhancers interact with which genes[26]. Perturbation of *cis* and/or *trans* regulatory factors can precipitate human disease[27,28], so it is important to understand the complexities of collaborative gene regulatory processes in order to better understand (and ultimately correct) the molecular bases of human disease.

Fortunately, an expansive genomic toolkit has been developed to study these intricate biological processes from the ground up. Whereas parts of the genome irrelevant to a given cell's function are effectively "turned OFF" via tight condensation of the DNA around structural proteins called histones, other genomic regions actively participating in regulation or expression of genes are largely devoid of histone occupancy and thus more free to function[29]. Methods like the assay for transposase-accessible chromatin using sequencing (ATAC-seq) are incredibly powerful to map genomic activity by systematically charting DNA accessibility[30]. Similarly, methods like chromatin immunoprecipitation with sequencing (ChIP-seq), cleavage under targets and release using nuclease (CUT&RUN), and newer variations thereof allow for detection and localization of histone modifications indicative of specific genomic features (e.g., H3K27 Acetylation marking enhancer elements)[31]. While such methods can provide rich maps of candidate regulatory features, they are limited in their observational nature because they (1) do not directly measure the functionality of genomic regions and (2) fall short of associating candidate regulatory features

6

with their gene target(s). Consequently, other methods are necessary to more resolutely identify regulatory elements controlling specific target genes.

In a twist of fate, one of our most powerful tools to study the immune system – genome editing with CRISPR/Cas9 – was derived from one of the main sources of immunological terror: bacteria[32]. Significant investment in developing engineered CRISPR systems for more precise and varied forms of genome editing has generated a multitude of tools that bestow the ability to do large-scale genetic screens[33] as well as therapeutic genetic interventions[34]. The Marson Lab has adapted these innovative genomic tools that disrupt gene expression through targeted DNA damage to study genetic processes directly in primary human T cells for a number of biological outputs[35–38], including systematic examination of *trans*-regulatory networks influencing immune disease-causing genes[39].

Other CRISPR systems have been engineered to inhibit (termed CRISPR Interference, or CRISPRi[40]) or activate (termed CRISPR Activation, or CRISPRa[41]) transcriptional activity rather than knockout genes. Whereas aforementioned genomic methods like ATAC- and ChIP-seq fall short of identifying functional *cis*-regulatory elements and associating the elements with their target gene(s), functional genomic screens with CRISPRi/a can do just that. The Marson Lab previously employed these tools to discover the *cis*-regulatory code governing expression of target genes in immortalized immune cell lines[42], using CRISPRa to identify regions sufficient to turn on gene expression. However, this work was performed before efficient protocols existed to deploy these CRISPR systems directly in primary T cells from patients. Recently, our lab reported systematic workflow optimizations that enabled CRISPRa and CRISPRi delivery into primary cells to study *trans* gene regulation[43]. With the newfound ability to conduct these screens, we set out to study systematically how the CD28 family of genes including *CD28*, *CTLA4*, and *ICOS* are genomically regulated. **Chapter 4** outlines how we use CRISPRi to functionally map the *cis*-regulatory elements influencing gene expression in the chr2q33.2 locus harboring our three genes of interest. This work builds on decades of study of gene regulation, demonstrating how our ever-

expanding genomic tool kit can be applied directly in primary cells to study complex genetic phenomena, from multi-gene co-regulation to insulation of one gene from the regulator of another.

1.4: Implications of Immunology on Human Health.

The immune system is omnipresent in the body: its cells course through the vasculature, permeate all human tissues, and retreat via lymphatics to specialized lymphoid organs. Innate cells are permanently embedded in tissues; others are under constant surveillance through circulation; more reside in specialized immune organs to aid the development, activation, and mobilization of adaptive immune cells. The complexity of the integrated immune response to pathogenic threats may transcend human logic for now, but we will continue to employ the most innovative scientific tools (genomic and otherwise) to understand its most convoluted intricacies. Well beyond protecting from pathogens like viruses and bacteria, the immune system plays an integral role in defending against tumors before they can take hold; pathogenically mediating both localized (e.g., rheumatoid arthritis) and systemic (e.g., lupus erythematosus) autoimmunity; and even affecting aging. Investments into immunology are investments into human health. Thus, the work presented here is but a small part of advancing biomedicine through enhanced understanding of the immune system in its various forms.

1.5: References

1. COVID-19 Data Explorer. *Our World in Data* https://ourworldindata.org/explorers/coronavirus-data-explorer.

2. Pardi, N., Hogan, M. J., Porter, F. W. & Weissman, D. mRNA vaccines - a new era in vaccinology. *Nat. Rev. Drug Discov.* **17**, 261–279 (2018).

3. Murphy, K. & Weaver, C. *Janeway's Immunobiology*. (Garland Science, 2016).

4. Waldman, A. D., Fritz, J. M. & Lenardo, M. J. A guide to cancer immunotherapy: from T cell basic science to clinical practice. *Nat. Rev. Immunol.* **20**, 651–668 (2020).

5. Burton, D. G. A. & Stolzing, A. Cellular senescence: Immunosurveillance and future immunotherapy. *Ageing Res. Rev.* **43**, 17–25 (2018).

6. Chi, X., Li, Y. & Qiu, X. V(D)J recombination, somatic hypermutation and class switch recombination of immunoglobulins: mechanism and regulation. *Immunology* **160**, 233–247 (2020).

7. Yamawaki, T. M. *et al.* Systematic comparison of high-throughput single-cell RNA-seq methods for immune cell profiling. *BMC Genomics* **22**, 66 (2021).

8. Hu, Z. *et al.* A cloning and expression system to probe T-cell receptor specificity and assess functional avidity to neoantigens. *Blood* **132**, 1911–1921 (2018).

9. Spindler, M. J. *et al.* Massively parallel interrogation and mining of natively paired human TCRαβ repertoires. *Nat. Biotechnol.* **38**, 609–619 (2020).

10. Shafer, P., Kelly, L. M. & Hoyos, V. Cancer Therapy With TCR-Engineered T Cells: Current Strategies, Challenges, and Prospects. *Front. Immunol.* **13**, 835762 (2022).

11. Sterner, R. C. & Sterner, R. M. CAR-T cell therapy: current limitations and potential strategies. *Blood Cancer J.* **11**, 69 (2021).

12. Li, M. *et al.* COVID-19 vaccine development: milestones, lessons and prospects. *Signal Transduct Target Ther* **7**, 146 (2022).

13. Subcommittee Demands FDA Comply with Investigation into Administration's Handling of Serology Testing. *House Committee on Oversight and Reform* https://oversightdemocrats.house.gov/news/press-releases/subcommittee-demands-fda-comply-with-investigation-into-administration-s (2020).

14. Hale, C. FDA names 28 antibody tests to be taken off the market. https://www.fiercebiotech.com/medtech/fda-names-28-antibody-tests-to-be-taken-off-market-after-increasing-oversight (2020).

15. Center for Devices & Radiological Health. EUA Authorized Serology Test Performance. *U.S. Food and Drug Administration* https://www.fda.gov/medical-devices/coronavirus-disease-2019-covid-19-emergency-use-authorizations-medical-devices/eua-authorized-serology-test-performance.

16. UCSF, the Chan Zuckerberg Initiative, CZ Biohub, and the State of California Partner to Expand and Utilize Clinical Testing Capacity for COVID-19. *CZ Biohub* https://www.czbiohub.org/ucsf-the-chan-zuckerberg-initiative-the-chan-zuckerberg-biohub-and-the-state-of-california-partner-to-expand-and-utilize-clinical-testing-capacity-for-covid-19/ (2021).

17. Crawford, E. D. *et al.* Rapid deployment of SARS-CoV-2 testing: The CLIAHUB. *PLoS Pathog.* **16**, e1008966 (2020).

18. Chen, L. & Flies, D. B. Molecular mechanisms of T cell co-stimulation and co-inhibition. *Nat. Rev. Immunol.* **13**, 227–242 (2013).

19. Bernard, D. *et al.* Costimulatory receptors in jawed vertebrates: conserved CD28, odd CTLA4 and multiple BTLAs. *Dev. Comp. Immunol.* **31**, 255–271 (2007).

20. Benton, M. L. *et al.* The influence of evolutionary history on human health and disease. *Nat. Rev. Genet.* **22**, 269–283 (2021).

21. Ille, A. M., Lamont, H. & Mathews, M. B. The Central Dogma revisited: Insights from protein synthesis, CRISPR, and beyond. *Wiley Interdiscip. Rev. RNA* **13**, e1718 (2022).

22. Retrovirus. *Genome.gov* https://www.genome.gov/genetics-glossary/Retrovirus.

23. Spitz, F. & Furlong, E. E. M. Transcription factors: from enhancer binding to developmental control. *Nat. Rev. Genet.* **13**, 613–626 (2012).

24. Wittkopp, P. J. & Kalay, G. Cis-regulatory elements: molecular mechanisms and evolutionary processes underlying divergence. *Nat. Rev. Genet.* **13**, 59–69 (2011).

25. Merkenschlager, M. & Nora, E. P. CTCF and Cohesin in Genome Folding and Transcriptional Gene Regulation. *Annu. Rev. Genomics Hum. Genet.* **17**, 17–43 (2016).

26. Pachano, T., Haro, E. & Rada-Iglesias, A. Enhancer-gene specificity in development and disease. *Development* **149**, (2022).

27. van der Lee, R., Correard, S. & Wasserman, W. W. Deregulated Regulators: Disease-Causing cis Variants in Transcription Factor Genes. *Trends Genet.* **36**, 523–539 (2020).

28. Epstein, D. J. Cis-regulatory mutations in human disease. *Brief. Funct. Genomic. Proteomic.* **8**, 310–316 (2009).

29. Klemm, S. L., Shipony, Z. & Greenleaf, W. J. Chromatin accessibility and the regulatory epigenome. *Nat. Rev. Genet.* **20**, 207–220 (2019).

30. Grandi, F. C., Modi, H., Kampman, L. & Corces, M. R. Chromatin accessibility profiling by ATAC-seq. *Nat. Protoc.* **17**, 1518–1552 (2022).

31. Bannister, A. J. & Kouzarides, T. Regulation of chromatin by histone modifications. *Cell Res.* **21**, 381–395 (2011).

32. Jinek, M. *et al.* A programmable dual-RNA-guided DNA endonuclease in adaptive bacterial immunity. *Science* **337**, 816–821 (2012).

33. Adli, M. The CRISPR tool kit for genome editing and beyond. *Nat. Commun.* **9**, 1911 (2018).

34. Sharma, G., Sharma, A. R., Bhattacharya, M., Lee, S.-S. & Chakraborty, C. CRISPR-Cas9: A Preclinical and Clinical Perspective for the Treatment of Human Diseases. *Mol. Ther.* **29**, 571–586 (2021).

35. Roth, T. L. *et al.* Pooled Knockin Targeting for Genome Engineering of Cellular Immunotherapies. *Cell* **181**, 728–744.e21 (2020).

36. Cortez, J. T. *et al.* CRISPR screen in regulatory T cells reveals modulators of Foxp3. *Nature* **582**, 416–420 (2020).

37. Schumann, K. *et al.* Functional CRISPR dissection of gene networks controlling human regulatory T cell identity. *Nat. Immunol.* **21**, 1456–1466 (2020).

38. Shifrut, E. *et al.* Genome-wide CRISPR Screens in Primary Human T Cells Reveal Key Regulators of Immune Function. *bioRxiv* 384776 (2018) doi:10.1101/384776.

39. Freimer, J. W. *et al.* Systematic discovery and perturbation of regulatory genes in human T cells reveals the architecture of immune networks. *Nat. Genet.* (2022) doi:10.1038/s41588-022-01106-y.

40. Kampmann, M. CRISPRi and CRISPRa Screens in Mammalian Cells for Precision Biology and Medicine. *ACS Chem. Biol.* **13**, 406–416 (2018).

41. Gilbert, L. A. *et al.* CRISPR-mediated modular RNA-guided regulation of transcription in eukaryotes. *Cell* **154**, 442–451 (2013).

42. Simeonov, D. R. *et al.* Discovery of stimulation-responsive immune enhancers with CRISPR activation. *Nature* **549**, 111–115 (2017).

43. Schmidt, R. *et al.* CRISPR activation and interference screens decode stimulation responses in primary human T cells. *Science* **375**, eabj4008 (2022).

Chapter 2: Evaluation of SARS-CoV-2 serology assays reveals a range of test performance.

This Chapter is published as:

Cody T. Mowery*, Jeffrey D. Whitman*, Joseph Hiatt*, Brian R. Shy*, Ruby Yu*, Tori N. Yamamoto, Ujjwal Rathore, Gregory M. Goldgof, Caroline Whitty, Jonathan M. Woo, Antonia E. Gallman, Tyler E. Miller, Andrew G. Levine, David N. Nguyen, Sagar P. Bapat, Joanna Balcerek, Sophia A. Bylsma, Ana M. Lyons, Stacy Li, Allison Wai-yi Wong, Eva Mae Gillis-Buck, Zachary B. Steinhart, Youjin Lee, Ryan Apathy, Mitchell J. Lipke, Jennifer Anne Smith, Tina Zheng, Ian C. Boothby, Erin Isaza, Jackie Chan, Dante D. Acenas, Jinwoo Lee, Trisha A. Macrae, Than S. Kyaw, David Wu, Dianna L. Ng, Wei Gu, Vanessa A. York, Haig Alexander Eskandarian, Perri C. Callaway, Lakshmi Warrier, Mary E. Moreno, Justine Levan, Leonel Torres, Lila A. Farrington, Rita P. Loudermilk, Kanishka Koshal, Kelsey C. Zorn, Wilfredo F. Garcia-Beltran, Diane Yang, Michael G. Astudillo, Bradley E. Bernstein, Jeffrey A. Gelfand, Edward T. Ryan, Richelle C. Charles, A. John Iafrate, Jochen K. Lennerz, Steve Miller , Charles Y. Chiu, Susan L. Stramer, Michael R. Wilson, Aashish Manglik, Chun Jimmie Ye, Nevan J. Krogan, Mark S. Anderson, Jason G. Cyster, Joel D. Ernst, Alan H. B. Wu , Kara L. Lynch, Caryn Bern[#], Patrick D. Hsu[#] and Alexander Marson[#]. Evaluation of SARS-CoV-2 serology assays reveals a range of test performance. *Nature Biotechnology*, 2020. [* and [#] denote equal contribution]

2.1: Abstract

Appropriate use and interpretation of serological tests for assessments of severe acute respiratory syndrome coronavirus 2 (SARS-CoV-2) exposure, infection and potential immunity require accurate data on assay performance. We conducted a head-to-head evaluation of ten point-of-care-style lateral flow assays (LFAs) and two laboratory-based enzyme-linked immunosorbent assays to detect anti-SARS-CoV-2 IgM and IgG antibodies in 5-d time intervals from symptom onset and studied the specificity of each assay in pre-coronavirus disease 2019 specimens. The percent of seropositive individuals increased with time, peaking in the latest time interval tested (>20d after symptom onset). Test specificity ranged from 84.3% to 100.0% and was predominantly affected by variability in IgM results. LFA specificity could be increased by considering weak bands as negative, but this decreased detection of antibodies (sensitivity) in a subset of SARS-CoV-2 real-time PCR-positive cases. Our results underline the importance of seropositivity threshold determination and reader training for reliable LFA deployment. Although there was no standout serological assay, four tests achieved more than 80% positivity at later time points tested and more than 95% specificity.

2.2: Main

To date, hundreds of thousands of deaths have been attributed to coronavirus disease 2019 (COVID-19)[1]. Millions of infections by SARS-CoV-2, the virus responsible for COVID-19, have been reported, although its full extent has yet to be determined owing to limited testing[2]. Government interventions to slow viral spread have disrupted daily life and economic activity for billions of people. Strategies to ease restraints on human mobility and interaction without provoking a major resurgence of transmission and mortality will depend on accurate estimates of population levels of infection and immunity[3]. Current testing for the virus largely depends on labor-intensive molecular techniques[4]. Individuals with positive molecular tests represent only a small

fraction of all infections, given limited deployment and the brief time window when real-time (RT)–PCR testing has the highest sensitivity[5,6,7]. The proportion of undocumented cases in the original epidemic focus was estimated to be as high as 86%[8], and asymptomatic infections are suspected to play a substantial role in transmission[9,10,11,12,13,14].

Widely available, reliable antibody detection assays would enable more accurate estimates of SARS-CoV-2 prevalence and incidence. On February 4, 2020, the Secretary of the US Department of Health and Human Services issued an emergency use authorization (EUA) for the diagnosis of SARS-CoV-2[15], allowing nucleic acid detection and immunoassay tests to be offered based on manufacturer-reported data without formal US Food and Drug Administration (FDA) clearance[16]. In response, dozens of companies began to market laboratory-based immunoassays and point-of-care (POC) tests. Rigorous, comparative performance data are crucial to inform clinical care and public health responses.

We conducted a head-to-head comparison of serology tests available to our group in early April, comprising ten immunochromatographic LFAs and two enzyme-linked immunosorbent assays (ELISAs) (for details, see Supplementary Table 2.1). Specimens were obtained from patients with SARS-CoV-2 that was confirmed by RT–PCR, contemporaneous patients with other respiratory pathogen testing and/or without SARS-CoV-2 by RT–PCR and blood donor specimens collected before 2019. We included analyses of performance by time from symptom onset and disease severity. Our goal was to provide well-controlled performance data to help guide the use of serology in the response to COVID-19.

2.3: Results

Study Population
This study included 128 plasma or serum specimens from 79 individuals who tested positive for SARS-CoV-2 and who were diagnosed in the University of California, San Francisco (UCSF) hospital system and Zuckerberg San Francisco General (ZSFG) Hospital. Patients

ranged from 22 to over 90 years of age (Table 2.1). Most patients were Hispanic/Latinx (68%),

reflecting the ZSFG patient population and demographics of the epidemic in San Francisco[17,18].

Most presented with cough (91%) and fever (86%). Chronic medical conditions, such as

hypertension, type 2 diabetes mellitus, obesity and chronic kidney disease, were frequent. Of the

79 individuals, 18% were not admitted, 46% were inpatients without intensive care unit (ICU) care

and 37% required ICU care. There were no reported deaths at the time of chart review.

Test Performance

Because we lacked a gold standard against which to benchmark the 12 tests in our study,

we assessed the positive percent agreement (positivity) compared with the RT–PCR assay. The

percentage of specimens testing positive rose with increasing time from symptom onset (Table

2.2 and Fig 2.1a), reaching the highest levels in the 16–20-d and >20-d time intervals. The highest

detection rate was achieved by combining IgM and IgG results (Fig 2.1b). However, 95%

confidence intervals (CIs) for later time intervals showed substantial overlap with those for earlier

intervals (Fig 2.1b). Four assays (Bioperfectus, Premier, Wondfo and in-house ELISA) achieved

more than 80% positivity in the later two time intervals (16–20 d and >20 d) while maintaining

more than 95% specificity. Some tests were not performed on a subset of specimens owing to

exhausted sample material, which might have affected reported percent positivity; the sample

size tested is reflected in 95% CIs. IgM detection was less consistent than IgG for nearly all

assays. Kappa agreement statistic ranged from 0.95 to 0.99 for IgG and from 0.81 to 1.00 for IgM

for standardized intensity score (Supplementary Table 2.2 and Supplementary Fig 2.2). Details

on establishing intensity score values and reader training are available in the

'Immunochromatographic LFAs' section within Methods. Although mean band intensities varied

among different assays, the approximate rate of sample positivity was generally consistent (Fig

2.2). For ELISA tests, a normalized value of sample optical density at 450 nm (OD450) divided

by calculated cutoff (signal-to-cutoff (S/CO)) was used to capture quantitative data about antibody

levels for each specimen. S/CO values provide a quantitative value comparable between plates.

Our ability to perform end-point dilutions was limited by specimen and assay availability.

We observed a trend toward higher percent positivity by LFA for patients admitted to the ICU compared to those having milder disease, but the specimen numbers per time interval were low, limiting statistical power (Supplementary Fig 2.3).

Test specificity in 108 pre-COVID-19 blood donor plasma samples ranged from 84.3% to 100.0%, with 39 samples demonstrating false-positive results by at least one LFA (Table 2.2 and Fig 2.2b). Of the false-positive results, 61.5% (24/39) had a weak intensity score of 1. Intensity scores of 2–3 were seen in 30.8% (12/39), and scores of 4–6 were seen in 7.7% (3/39).

We evaluated the tradeoff between percent positivity in samples from RT–PCR-positive individuals and specificity as a function of LFA reader score. RT–PCR measures the presence of viral nucleotides. Individuals with RT–PCR-proven SARS-CoV-2 infection are expected to seroconvert and develop anti-SARS-CoV-2 antibodies, although frequency and kinetics of seroconversion can vary[5,6,19,20,21,22]. We, therefore, assessed percent positivity at various time intervals after onset of symptoms. Changing the positive LFA threshold from 1 to 2 decreased the mean overall percent positivity across tests from 67.2% (range, 57.9–75.4%) to 57.8% (range, 44.7–65.6%) and increased the average specificity from 94.2% (range, 84.3–100.0%) to 98.1% (range, 94.4–100.0%) (Fig 2.3).

An independent study at Massachusetts General Hospital (MGH) compared three LFAs, of which BioMedomics was also assessed in the current study (Supplementary Table 2.3). Although study design and methods differed between sites, precluding direct comparison of results (see 'Study design' in Methods), test validation efforts at another site provided additional useful data. Overall, both studies showed a trend for increased detection of SARS-CoV-2-specific antibodies with increased time from symptom onset. However, the MGH study displayed increased specificity with lower percent positivity at early time points after symptom onset. MGH positivity thresholds were set higher to prioritize test specificity (Fig 2.3b,c).

A set of specimens collected during the COVID-19 outbreak that had negative SARS-CoV-

17

2 RT–PCR testing and/or alternative respiratory pathogen testing demonstrated higher numbers of positive results compared to the pre-COVID-19 sample set (Fig 2.2c). Five specimens had positive results by more than three tests, all with respiratory symptoms and concurrent negative or un-performed SARS-CoV-2 RT–PCR testing (Fig 2.2c, arrows). One patient was positive on eight different tests, including the in-house ELISA. In this limited panel, no consistent pattern of cross-reactivity was identified with non-SARS-CoV-2 respiratory viruses, including two strains of seasonal coronavirus (one coronavirus OC43 and three coronavirus HKU1).

Agreement among results of LFAs with those of IgG and IgM Epitope ELISAs ranged from 75.7% to 85.6%, whereas agreement with the in-house ELISA ranged from 83.5% to 94.8% (Fig 2.4a). LFA band intensity scores showed a direct correlation with ELISA S/CO values (Fig 2.4b).

2.4: Discussion

This study describes test performance for 12 COVID-19 serology assays on a panel of 128 samples from 79 individuals with RT–PCR-confirmed SARS-CoV-2 infection and 108 pre-COVID-19 specimens. In April 2020, when we performed this analysis, there was no assay with sufficient performance data for use as a proven reference standard; only three serological assays had an FDA EUA[23]; and anti-SARS-CoV-2 IgM and IgG kinetics were poorly understood. We, therefore, chose a specimen set covering the first several weeks after illness onset in patients with SARS-CoV-2 proven by RT–PCR to avoid the potential bias of assuming superiority of one assay over the others. To date, no single assay or combination of assays has been accepted as a gold standard comparator for antibody testing. Additionally, we surveyed 51 specimens from individuals who were tested for other respiratory viral pathogens and/or had negative molecular testing for SARS-CoV-2 to evaluate potential cross-reactivity or infections detected only by serology. Our data are also available on a dedicated website (https://covidtestingproject.org). We hope these data will inform the use of serology by the medical and public health communities and

provide feedback to test developers about areas of success and necessary improvement.

We focused on comparisons of percent positivity by time interval, rather than reporting the 'sensitivity' of each assay, both because of the lack of a gold standard to test against and our expectation that percent positivity would rise with increasing time after symptom onset[5,6,19,20,21,22,24,25]. Percent positivity above 80% was not reached until at least 2 weeks into clinical illness; diagnosis early in the course of illness remains dependent on viral detection methods. Our data are consistent with growing evidence that IgM and IgG tend to rise around the same time in COVID-19[5,19]. The assays showed a trend to higher positive rates within time intervals for more severe disease, but this finding should be interpreted with caution, owing to the limited data from ambulatory cases. Most samples more than 20 d after symptom onset had detectable anti-SARS-CoV-2 antibodies, suggesting good to excellent sensitivity for all evaluated tests in hospitalized patients three or more weeks into their disease course. Additional studies assessing frozen versus fresh specimens and matrix effects between serum versus plasma will be useful in understanding potential limitations of our current test performance evaluations. Looking forward, well-powered studies testing ambulatory or asymptomatic individuals, including LFA performance with fresh capillary blood, will be essential to guide appropriate use of serology.

Our data demonstrate specificity of more than 95% for most tests evaluated and more than 99% for two LFAs (Wondfo and Sure Biotech) and the in-house ELISA (adapted from Amanat et al., 2020)[26]. We observed moderate to strong positive bands in several pre-COVID-19 blood donor specimens, some of them positive by multiple assays, suggesting the possibility of non-specific binding of plasma proteins, non-specific antibodies (potentially including auto-antibodies) or cross-reactivity with antibodies against other viruses. Three of the pre-COVID-19 specimens (2.8%) were scored positive by more than three assays. Intriguingly, the fraction of positive tests was higher in a set of recent specimens obtained during the COVID-19 outbreak from individuals undergoing respiratory infection workup, many with negative SARS-CoV-2 RT–PCR. Five of these (9.8%) had positive results by more than three assays, without relation to a specific viral

pathogen, suggesting non-specific reactivity and/or missed COVID-19 diagnosis. Recent reports demonstrate that RT–PCR from nasopharyngeal swabs might yield false-negative results in over 20% of cases[5,27], and co-infection with other respiratory pathogens might be significantly higher than previously anticipated[28]. One specimen was positive by 8 of 12 assays, including the in-house ELISA. The patient was over 90 years old and presented with altered mental status, fever and ground glass opacities on chest radiological imaging. SARS-CoV-2 RT–PCR was negative, and ancillary laboratory testing suggested a urinary tract infection. This case could represent COVID-19 not detected by RT–PCR, reinforcing the importance of caution in interpreting negative molecular results as ruling out the infection. Appropriate algorithms for serology testing, including confirmatory or reflexive testing, have yet to be determined. These algorithms will be affected by test performance characteristics and prevalence of disease, as well as pre-test probability of infection.

Importantly, we still do not know the extent to which positive results by serology reflect a protective immune response, nor how long such protection might last[29]. Neutralization assays measure the ability of blood-derived samples to prevent viral (most commonly pseudovirus) infection of cultured cells in vitro[30,31]. Although these assays provide information on the functional capabilities of an individual's antibodies, their correlation with total IgG antibodies to serological test antigens (primarily spike and nucleocapsid proteins) is not well established. Additionally, most antibody neutralization assays are research laboratory based with limited test performance data and inter-lab standardization measures. Antibody neutralization assays should be harmonized across laboratories to establish the extent to which conventional serology assays correlate with neutralization. Further studies are needed to assess the relationships among positive serological testing, in vitro viral neutralization results and clinical protection from future SARS-CoV-2 infection and transmission. Epidemiological data and results from convalescent plasma treatment trials should help guide clinical and public health policies for use of serological testing.

High specificity testing is crucial in low-prevalence settings. One approach to increase

specificity would employ confirmatory testing with an independent assay (perhaps recognizing a distinct epitope or antigen). Our comparison of UCSF and MGH data suggests that reclassifying faint bands as 'negative' or 'inconclusive' can change test performance characteristics by increasing specificity, albeit at the expense of sensitivity. However, the subjectivity of calling faint bands by individual readers might be difficult to standardize without specific control materials, operator training and/or objective methods of analyzing LFAs. In the clinical setting, these parameters and protocols should be independently assessed and validated by clinical laboratories for operation under the Clinical Laboratory Improvement Amendments[32].

Objective methods to standardize LFA reading, such as digital image analysis, are potentially attractive. Image analysis tools can be benchtop or mobile (for example, smartphone applications). However, introduction of a separate device for reading LFAs will require specific validation. Variables, including lighting, camera quality, image compression and quantification algorithms, must all be assessed rigorously to ensure accuracy and precision.

A consensus has emerged that serological testing provides an essential tool in the pandemic response, but inadequate data on test performance characteristics in some early surveys and important gaps in immunological knowledge have impeded agreement on appropriate implementation strategies[33,34]. Our study highlights the need for rigorous assay validation using standardized sample sets with: 1) known positives from individuals with a range of clinical presentations at multiple time points after onset of symptoms; 2) pre-COVID-19 outbreak samples for specificity; and 3) samples from individuals with other viral and inflammatory illnesses as cross-reactivity controls. Coordinated efforts to ensure widespread availability of validated sample sets would facilitate data-driven decisions on the use of serology. The updated guidance released by the FDA in early May 2020[35] and the initiative recently launched by the FDA and the US National Cancer Institute/National Institutes of Health[36] to systematize data generation for EUAs are substantive steps toward this goal and will help build the essential evidence base to guide serological testing during the COVID-19 pandemic.

2.5: Methods

Ethical approvals
This study was approved by institutional review boards at the UCSF/ZSFG and MGH.

Study design

The study population included individuals with symptomatic infection and positive SARS-CoV-2 RT–PCR testing of nasopharyngeal or oropharyngeal swabs who had remnant serum and plasma specimens in clinical laboratories serving the UCSF and ZSFG medical center networks. All samples were obtained from venous blood draws, with serum being collected in either uncoated or serum separator tubes and plasma from lithium heparin tubes depending on other ancillary testing orders. All samples were drawn in an outpatient or hospital setting, professionally couriered to the clinical laboratory and acquisitioned for routine testing within the clinical laboratory within the same day. Samples were stored at 4˚C and aliquoted for freezing at −20 °C within 1 week of the initial blood draw. Serum and plasma were used interchangeably. All but one assay (Epitope ELISA) noted that either specimen type could be used. We included multiple specimens per individual but no more than one sample per time interval (1–5, 6–10, 11–15, 16–20 and >20 d after symptom onset). If an individual had more than one specimen for a given time interval, only the later specimen was included. For specificity, we included 108 pre-COVID-19 plasma specimens from eligible blood donors collected before July 2018[37]. We assessed detection of SARS-CoV-2 antibodies in 51 specimens from 2020: 49 with test results for detection of other respiratory viruses (BioFire FilmArray, BioFire Diagnostics) and 31 with negative results by SARS-CoV-2 RT–PCR. For these specimens, the median days from symptom onset was four with a range of 0–107 d, the latter end of the range owing to unresolving respiratory viral infection in the setting of HIV infection.

We based minimum sample size calculations on expected binomial exact 95% confidence limits. A total of 287 samples were included in the final analysis, including 128 from 79 individuals

who tested positive for SARS-CoV-2 by RT–PCR. Some specimens were exhausted during the analysis and were not included in all tests. Data obtained from serial specimens that did not conform to our study design were excluded.

Clinical data were extracted from electronic health records and entered in a Health Insurance Portability and Accountability Act-secure REDCap database hosted by UCSF. Data included demographic information, major comorbidities, patient-reported symptom onset date, symptoms and indicators of severity.

Independent data from testing efforts at MGH, with slight deviations in methods, are included as Supplementary Data (Supplementary Fig 2.3). Briefly, 48 heat-inactivated serum/plasma samples from 44 individuals who tested positive for SARS-CoV-2 by RT–PCR were included. For specificity, the MGH study included 60 heat-inactivated pre-COVID-19 samples from 30 asymptomatic adults and 30 individuals admitted with febrile and/or respiratory illness with a confirmed pathogen.

Sample preparation

Samples from UCSF and ZSFG were assigned a random well position in one of four 96-well plates. Samples were thawed at 37 °C, and up to 200 µl was transferred to the assigned well without heat inactivation. Samples were then sub-aliquoted (12.5 µl) to replica plates for testing. Replica plates were stored at −20 °C until needed and then thawed for 10 min at room temperature and briefly centrifuged before testing. All sample handling followed UCSF biosafety committee-approved practices.

For the MGH study, samples were heat inactivated at 56 °C for 60 min, aliquoted and stored at 4 °C and −20 °C. Samples stored at 4 °C were used within 7 d. Frozen aliquots were stored until needed with only a single freeze-thaw cycle for any sample. All samples were brought to room temperature and briefly centrifuged before adding the recommended volume to the LFA cartridge.

Immunochromatographic LFAs

Ten LFAs were evaluated (Supplementary Table 2.1). At the time of testing, cartridges were labeled by randomized sample location (plate and well). The appropriate sample volume was transferred from the plate to the indicated sample port, followed by provided diluent, following manufacturer instructions. The lateral flow cartridges were incubated for the recommended time at room temperature before readings. Each cartridge was assigned an integer score (0 for negative, 1–6 for positive) for test line intensity by two independent readers blinded to specimen status and to each other's scores (Supplementary Fig 2.1). Readers were trained to score intensity from images representative of each value from a previous LFA test performance evaluation[37]. Test line scoring was performed for research purposes to capture semi-quantitative data about the LFA readout and reproducibility of subjective interpretation, considering that these are the major analytical factors that affect test performance. These tests are prescribed to be interpreted qualitatively, and test performance characteristics in this report are derived from qualitative scoring of any interpreted band color. For some cartridges (DeepBlue, UCP and Bioperfectus), the positive control indicator failed to appear after addition of diluent in a significant fraction of tests. For these tests, two further drops of diluent were added to successfully recover control indicators in all affected tests. These results were included in analyses. During testing, two plates were transposed 180°, and assays were run in the opposite order from the wells documented on cartridges. These data were corrected, and accuracy was confirmed by empty well position and verification of a subset of results.

ELISAs

Epitope Diagnostics assays were carried out according to manufacturer instructions with minor deviations, including the mixed use of plasma and serum specimens (instead of serum only), use of frozen specimens (versus same day), blanking all specimens and controls instead of using raw OD450 values and performing samples in singlicate for three of four 96-well plates (instead of duplicate). Plate 4 was run in duplicate owing to availability of samples and assay

24

wells. For IgM detection, 100 µl of control samples or 10 µl of patient serum and 100 µl of sample diluent were added to indicated wells. Plates were incubated for 30 min at 37 °C and manually washed five times in provided Wash Buffer. Each well received 100 µl of horseradish peroxidase (HRP)-labeled COVID-19 antigen, was incubated for 30 min at 37 °C and was manually washed five times in provided Wash Buffer. Each well then received 100 µl of colorimetric substrate, was incubated for 20 min and then received 100 µl of Stop Solution. The OD450 was measured using a Synergy H1 Microplate Reader (BioTek Instruments) within 10 min of adding Stop Solution. Positive cutoff for IgM detection was calculated as described in the Epitope Diagnostics protocol: IgM positive cutoff = 1.1 × ((average of negative control readings) + 0.10). Values less than or equal to the positive cutoff were interpreted as negative. For IgG detection, 1 µl of serum was diluted 1:100 in Sample Diluent and loaded into designated wells. Plates were incubated for 30 min at room temperature and manually washed five times in provided Wash Buffer. Each well received 100 µl of provided HRP-labeled COVID-19 Tracer Antibody; plates were incubated for 30 min at room temperature and manually washed five times in provided Wash Buffer. Then, each well received 100 µl of Substrate, was incubated for 20 min and then received 100 µl of Stop Solution. The absorbance at OD450 was measured using a Synergy H1 Microplate Reader (BioTek Instruments) within 10 min of adding Stop Solution. Positive cutoffs for IgG detection were calculated as described in the Epitope Diagnostics protocol: IgG positive cutoff = 1.1 × ((average of negative control readings) + 0.18). Values less than or equal to the positive cutoff were interpreted as negative.

An in-house receptor binding domain (RBD)-based ELISA was performed with minor deviations from a published protocol (Amanat et al.[26], Krammer Lab, Mount Sinai School of Medicine). SARS-CoV-2 RBD protein was produced using the published construct (NR-52306, BEI Resources) by Aashish Manglik (UCSF). Next, 96-well plates (3855, Thermo Fisher Scientific) were coated with 2 µg ml−1 RBD protein and stored at 4 °C for up to 5 d before use. Specimen aliquots (12 µl) were diluted 1:5 in 1× phosphate-buffered saline (PBS) (10010-023, Gibco), mixed

and heat inactivated at 56 °C for 1 h. RBD-treated plates were washed three times with PBS-Tween (PBST, BP337-500, Fisher Bioreagents) using a 405 TS Microplate Washer (BioTek Instruments) and blocked with PBST-Milk (3% wt/vol, AB10109-01000, AmericanBio) for 1 h at 20 °C. Samples were further diluted 1:10 (1:50 final) in PBST-Milk (1% wt/vol), and 100 µl was transferred to the blocked ELISA plates in duplicate plates. Samples were incubated for 2 h at 20 °C and washed three times with PBST. The peroxidase AffiniPure Goat Anti-human IgG (F(ab′)20-specific) secondary antibody (109-035-097, lot 146576, Jackson ImmunoResearch) used in this study binds the IgG light chain and has some reactivity for other isotypes (IgM and IgA). This secondary antibody was diluted 1:750 in PBST-Milk (1% wt/vol), 50 µl was added to each sample well and samples were incubated for 1 h at 20 °C. Plates were subsequently washed three times with PBST. We dispensed 100 µl of 1× SigmaFast OPD Solution (P9187, Sigma-Aldrich) to each sample well and incubated plates for 10 min at room temperature. We added 50 µl of 3M HCl (A144-212, Fisher Chemical) to stop the reaction and immediately read the optical density at 490 nm (OD490) using a Synergy H1 Microplate Reader (BioTek Instruments). OD490 values were corrected for each plate by subtracting the mean value of each plate's blank wells. To determine a cutoff for positive values, we calculated the mean value of negative wells for each plate, plus three standard deviations.

Data analysis

For LFA testing, the second reader's scores were used for performance calculations, and the first reader's scores were used to calculate inter-reader agreement statistics. Percent seropositivity among RT–PCR-confirmed cases was calculated by time interval from symptom onset. Specificity was based on results in pre-COVID-2019 samples. Binomial exact 95% CIs were calculated for all estimates. Analyses were conducted in R (3.6.3) and SAS (9.4).

Acknowledgements

Disclosures

2.6: Tables & Figures

Table 2.1: Demographics and clinical characteristics of patients who tested positive for SARS-CoV-2 by RT–PCR

Variable	All patients (n = 79)	0–5 d (n = 28)	6–10 d (n = 36)	11–15 d (n = 34)	16–20 d (n = 19)	>20 d (n = 11)
Age, mean (s.d.)	52.9 (15)	48.2 (15.0)	53.3 (15.1)	58.1 ± 15.1	56.6 (13.2)	55.5 (14.8)
Male sex (%)	54 (68)	15 (54)	24 (67)	21 (62)	12 (63)	8 (73)
Racial or ethnic group						
Hispanic/Latinx (%)	54 (68)	18 (64)	29 (81)	23 (68)	12 (63)	7 (64)
Asian (%)	7 (9)	3 (11)	2 (6)	4 (12)	3 (16)	0 (0)
White (%)	7 (9)	3 (11)	1 (3)	2 (6)	2 (11)	0 (0)
Black (%)	6 (8)	2 (7)	3 (8)	4 (12)	1 (5)	2 (18)
Other/not reported (%)	5 (6)	2 (7)	1 (3)	1 (3)	1 (5)	2 (18)
Presenting symptoms						
Cough (%)	72 (91)	24 (86)	33 (92)	31 (91)	17 (89)	9 (82)
Fever (%)	68 (86)	23 (82)	30 (83)	29 (85)	17 (89)	9 (82)
Myalgia (%)	29 (37)	8 (29)	12 (33)	13 (38)	8 (42)	3 (27)
Chest pain (%)	20 (25)	5 (18)	8 (22)	7 (21)	5 (26)	4 (36)
Headache (%)	20 (25)	4 (14)	11 (31)	9 (26)	6 (32)	4 (36)
Chills (%)	19 (24)	5 (18)	9 (25)	7 (21)	7 (37)	2 (18)
Sore throat (%)	19 (24)	4 (14)	11 (31)	8 (24)	5 (26)	3 (27)
Malaise (%)	17 (22)	4 (14)	7 (19)	9 (26)	4 (21)	1 (9)
Diarrhea (%)	13 (16)	4 (14)	7 (19)	6 (18)	4 (21)	1 (9)
Anorexia (%)	8 (10)	2 (7)	1 (3)	2 (6)	4 (21)	1 (9)
Nausea and/or vomiting (%)	8 (10)	2 (7)	2 (6)	2 (6)	2 (11)	1 (9)
Anosmia and/or dysgeusia (%)	4 (5)	1 (4)	1 (3)	2 (6)	0 (0)	1 (9)
Chronic medical conditions						
Hypertension (%)	36 (46)	11 (39)	17 (47)	21 (62)	11 (58)	6 (55)
Type 2 diabetes mellitus (%)	33 (42)	11 (39)	17 (47)	19 (56)	8 (42)	6 (55)
Obesity (%)	19 (24)	7 (25)	9 (25)	11 (32)	6 (32)	6 (55)
Chronic kidney disease (%)	10 (13)	4 (14)	3 (8)	6 (18)	4 (21)	3 (27)
Hypothyroid (%)	6 (8)	3 (11)	3 (8)	3 (9)	0 (0)	0 (0)
Solid organ transplant (%)	6 (8)	2 (7)	0 (0)	2 (6)	2 (11)	2 (18)
Coronary artery disease (%)	5 (6)	1 (4)	1 (3)	2 (6)	2 (11)	3 (27)
Asthma (%)	4 (5)	1 (4)	1 (3)	3 (9)	2 (11)	0 (0)
Congestive heart failure (%)	3 (4)	2 (7)	2 (6)	2 (6)	1 (5)	0 (0)
Liver disease (%)	3 (4)	0 (0)	1 (3)	2 (6)	1 (5)	1 (9)
Malignancy (%)	3 (4)	1 (4)	2 (6)	1 (3)	2 (11)	0 (0)
Emphysema (%)	2 (3)	0 (0)	1 (3)	1 (3)	1 (5)	1 (9)
Prior stroke (%)	2 (3)	1 (4)	0 (0)	0 (0)	0 (0)	1 (9)
HIV (%)	1 (1)	1 (4)	0 (0)	0 (0)	0 (0)	0 (0)
Other immune-compromised condition[b] (%)	5 (6)	1 (4)	1 (3)	3 (9)	2 (11)	1 (9)
Highest level of care						
Ambulatory[c] (%)	14 (18)	9 (32)	2 (6)	3 (9)	0 (0)	0 (0)
Admitted (%)	36 (46)	11 (39)	19 (53)	12 (35)	5 (26)	4 (36)
ICU (%)	29 (37)	8 (29)	15 (42)	19 (56)	14 (74)	7 (64)

[a]Baseline demographic characteristics, presenting symptoms, chronic medical conditions, initial disposition and highest-level outcome for all participants whose samples were included in each time interval for serological testing. Only one sample per patient was included in each time interval, and some individuals are represented by multiple samples in different time intervals. In total, we tested 128 samples taken from 79 patients who tested positive for SARS-CoV-2 by RT–PCR. [b]Other immune-compromised condition includes rheumatology patients (rheumatoid arthritis, psoriasis, Crohn's disease, ankylosing spondylitis and reactive arthritis), all of whom were taking immune modulating/suppressing therapies. [c]Ambulatory care includes outpatients as well as patients seen in the emergency department and not admitted.

Table 2.2: Summary statistics for immunochromatographic LFAs and ELISAs

	Percentage of positive specimens from patients who tested positive for SARS-CoV-2 by RT–PCR											
	IgM				IgG				IgM or IgG			
Assay	Total *n*	Positive	%	95% CI	Total *n*	Positive	%	95% CI	Total *n*	Positive	%	95% CI
Immunochromatographic LFAs												
Biomedomics												
1–5 d	27	7	25.9	11.1–46.3	27	6	22.2	8.6–42.3	27	8	29.6	13.8–50.2
6–10 d	36	22	61.1	43.5–76.9	36	19	52.8	35.5–69.6	36	23	63.9	46.2–79.2
11–15 d	33	25	75.8	57.7–88.9	33	23	69.7	51.3–84.4	33	26	78.8	61.1–91.0
16–20 d	19	16	84.2	60.4–96.6	19	14	73.7	48.8–90.9	19	17	89.5	66.9–98.7
>20 d	11	9	81.8	48.2–97.7	11	9	81.8	48.2–97.7	11	9	81.8	48.2–97.7
Bioperfectus												
1–5 d	28	11	39.3	21.5–59.4	28	7	25.0	10.7–44.9	28	11	39.3	21.5–59.4
6–10 d	35	26	74.3	56.7–87.5	35	23	65.7	47.8–80.9	35	27	77.1	59.9–89.6
11–15 d	34	28	82.4	65.5–93.2	34	27	79.4	62.1–91.3	34	30	88.2	72.5–96.7
16–20 d	19	16	84.2	60.4–96.6	19	14	73.7	48.8–90.9	19	17	89.5	66.9–98.7
>20 d	10	10	100.0	69.2–100.0	10	9	90.0	55.5–99.7	10	10	100.0	69.2–100.0
DecomBio												
1–5 d	26	8	30.8	14.3–51.8	26	7	26.9	11.6–47.8	26	8	30.8	14.3–51.8
6–10 d	36	24	66.7	49.0–81.4	36	24	66.7	49.0–81.4	36	24	66.7	49.0–81.4
11–15 d	33	29	87.9	71.8–96.6	33	29	87.9	71.8–96.6	33	29	87.9	71.8–96.6
16–20 d	18	14	77.8	52.4–93.6	18	14	77.8	52.4–93.6	18	14	77.8	52.4–93.6
>20 d	11	10	90.9	58.7–99.8	11	10	90.9	58.7–99.8	11	10	90.9	58.7–99.8
DeepBlue												
1–5 d	28	12	42.9	24.5–62.8	28	6	21.4	8.3–41.0	28	12	42.9	24.5–62.8
6–10 d	36	28	77.8	60.8–89.9	36	18	50.0	32.9–67.1	36	28	77.8	60.8–89.9
11–15 d	34	28	82.4	65.5–93.2	34	21	61.8	43.6–77.8	34	28	82.4	65.5–93.2
16–20 d	19	16	84.2	60.4–96.6	19	15	78.9	54.4–93.9	19	17	89.5	66.9–98.7
>20 d	11	10	90.9	58.7–99.8	11	9	81.8	48.2–97.7	11	10	90.9	58.7–99.8
Innovita												
1–5 d	27	4	14.8	4.2–33.7	27	7	25.9	11.1–46.3	27	7	25.9	11.1–46.3
6–10 d	36	12	33.3	18.6–51.0	36	17	47.2	30.4–64.5	36	20	55.6	38.1–72.1
11–15 d	31	12	38.7	21.8–57.8	32	25	78.1	60.0–90.7	32	25	78.1	60.0–90.7
16–20 d	13	4	30.8	9.1–61.4	13	9	69.2	38.6–90.9	13	9	69.2	38.6–90.9
>20 d	6	1	16.7	0.4–64.1	6	4	66.7	22.3–95.7	6	5	83.3	35.9–99.6
Premier												
1–5 d	28	10	35.7	18.6–55.9	28	6	21.4	8.3–41.0	28	10	35.7	18.6–55.9
6–10 d	35	25	71.4	53.7–85.4	35	18	51.4	34.0–68.6	35	25	71.4	53.7–85.4
11–15 d	34	28	82.4	65.5–93.2	34	22	64.7	46.5–80.3	34	29	85.3	68.9–95.0
16–20 d	19	16	84.2	60.4–96.6	19	14	73.7	48.8–90.9	19	17	89.5	66.9–98.7
>20 d	11	10	90.9	58.7–99.8	11	9	81.8	48.2–97.7	11	10	90.9	58.7–99.8
Sure												
1–5 d	28	3	10.7	2.3–28.2	28	5	17.9	6.1–36.9	28	5	17.9	6.1–36.9
6–10 d	35	15	42.9	26.3–60.6	35	19	54.3	36.6–71.2	35	19	54.3	36.6–71.2
11–15 d	34	22	64.7	46.5–80.3	34	25	73.5	55.6–87.1	34	25	73.5	55.6–87.1
16–20 d	19	14	73.7	48.8–90.9	19	14	73.7	48.8–90.9	19	15	78.9	54.4–93.9
>20 d	11	8	72.7	39.0–94.0	11	10	90.9	58.7–99.8	11	10	90.9	58.7–99.8
UCP												
1–5 d	28	7	25.0	10.7–44.9	28	7	25.0	10.7–44.9	28	7	25.0	10.7–44.9
6–10 d	36	21	58.3	40.8–74.5	36	18	50.0	32.9–67.1	36	21	58.3	40.8–74.5

Continued

	IgM				IgG				IgM or IgG			
Assay	**Total *n***	**Positive**	**%**	**95% CI**	**Total *n***	**Positive**	**%**	**95% CI**	**Total *n***	**Positive**	**%**	**95% CI**
11–15 d	34	26	**76.5**	58.8–89.3	34	25	**73.5**	55.6–87.1	34	27	**79.4**	62.1–91.3
16–20 d	19	15	**78.9**	54.4–93.9	19	14	**73.7**	48.8–90.9	19	15	**78.9**	54.4–93.9
>20 d	11	10	**90.9**	58.7–99.8	11	9	**81.8**	48.2–97.7	11	10	**90.9**	58.7–99.8
VivaChek												
1–5 d	25	7	**28.0**	12.1–49.4	25	7	**28.0**	12.1–49.4	25	7	**28.0**	12.1–49.4
6–10 d	35	22	**62.9**	44.9–78.5	35	22	**62.9**	44.9–78.5	35	22	**62.9**	44.9–78.5
11–15 d	30	26	**86.7**	69.3–96.2	30	25	**83.3**	65.3–94.4	30	26	**86.7**	69.3–96.2
16–20 d	19	15	**78.9**	54.4–93.9	19	14	**73.7**	48.8–90.9	19	15	**78.9**	54.4–93.9
>20 d	10	9	**90.0**	55.5–99.7	10	9	**90.0**	55.5–99.7	10	9	**90.0**	55.5–99.7
Wondfo												
1–5 d									26	10	**38.5**	20.2–59.4
6–10 d									36	24	**66.7**	49.0–81.4
11–15 d									32	27	**84.4**	67.2–94.7
16–20 d									19	17	**89.5**	66.9–98.7
>20 d									11	9	**81.8**	48.2–97.7
ELISAs												
Epitope												
1–5 d	28	5	**17.9**	6.1–36.9	28	11	**39.3**	21.5–59.4	28	11	**39.3**	39.3–21.5
6–10 d	36	19	**52.8**	35.5–69.6	36	28	**77.8**	60.8–89.9	36	29	**80.6**	80.6–64.0
11–15 d	34	27	**79.4**	62.1–91.3	34	31	**91.2**	76.3–98.1	34	31	**91.2**	91.2–76.3
16–20 d	19	14	**73.7**	48.8–90.9	19	16	**84.2**	60.4–96.6	19	17	**89.5**	89.5–66.9
>20 d	11	9	**81.8**	48.2–97.7	11	10	**90.9**	58.7–99.8	11	10	**90.9**	90.9–58.7
In-house[a]												
1–5 d									28	10	**35.7**	18.6–55.9
6–10 d									36	26	**72.2**	54.8–85.8
11–15 d									34	32	**94.1**	80.3–99.3
16–20 d									19	17	**89.5**	66.9–98.7
>20 d									11	9	**81.8**	48.2–97.7

<div align="center">Specificity in 108 blood donor plasma specimens collected before July 2018</div>

	IgM				IgG				IgM or IgG			
Assay	**Total *n***	**Positive**	**Specificity (%)**	**95% CI**	**Total *n***	**Positive**	**Specificity (%)**	**95% CI**	**Total *n***	**Positive**	**Specificity (%)**	**95% CI**
Immunochromatographic LFAs												
Biomedomics	107	13	**87.9**	80.1–93.4	107	4	**96.3**	90.7–99.0	107	14	**86.9**	79.0–92.7
Bioperfectus	104	3	**97.1**	91.8–99.4	104	2	**98.1**	93.2–99.8	104	5	**95.2**	89.1–98.4
DecomBio	107	10	**90.7**	83.5–95.4	107	9	**91.6**	84.6–96.1	107	11	**89.7**	82.3–94.8
DeepBlue	108	17	**84.3**	76.0–90.6	108	1	**99.1**	94.9–100.0	108	17	**84.3**	76.0–90.6
Innovita	108	4	**96.3**	90.8–99.0	108	0	**100.0**	96.6–100.0	108	4	**96.3**	90.8–99.0
Premier	108	2	**98.1**	93.5–99.8	108	1	**99.1**	94.9–100.0	108	3	**97.2**	92.1–99.4
Sure	108	0	**100.0**	96.6–100.0	108	0	**100.0**	96.6–100.0	108	0	**100.0**	96.6–100.0
UCP	107	2	**98.1**	93.4–99.8	107	2	**98.1**	93.4–99.8	107	2	**98.1**	93.4–99.8
VivaChek	99	5	**94.9**	88.6–98.3	99	4	**96.0**	90.0–98.9	99	5	**94.9**	88.6–98.3
Wondfo									106	1	**99.1**	94.9–100.0
ELISAs												
Epitope	108	3	**97.2**	92.1–99.4	108	10	**90.7**	83.6–95.5	108	11	**89.8**	82.5–94.8
In-house[b]									108	1	**99.1**	94.9–100.0

Percentage of positive specimens from individuals who tested positive for non-SARS-CoV-2 viral infections and/or tested negative for SARS-CoV-2 by RT–PCR

Assay	IgM				IgG				IgM or IgG			
	Total *n*	Positive	%	95% CI	Total *n*	Positive	%	95% CI	Total *n*	Positive	%	95% CI
Immunochromatographic LFA												
Biomedomics	51	8	**15.7**	7.0–28.6	51	4	**7.8**	2.2–18.9	51	11	**21.6**	11.3–35.3
Bioperfectus	45	5	**11.1**	3.7–24.1	45	6	**13.3**	5.1–26.8	45	8	**17.8**	8.0–32.1
DecomBio	51	5	**9.8**	3.3–21.4	51	2	**3.9**	0.5–13.5	51	6	**11.8**	4.4–23.9
DeepBlue	51	14	**27.5**	15.9–41.7	51	7	**13.7**	5.7–26.3	51	14	**27.5**	15.9–41.7
Innovita	28	2	**7.1**	0.9–23.5	28	2	**7.1**	0.9–23.5	28	3	**10.7**	2.3–28.2
Premier	51	0	**0.0**	0.0–7.0	51	1	**2.0**	0.0–10.4	51	2	**3.9**	0.5–13.5
Sure	51	0	**0.0**	0.0–7.0	51	0	**0.0**	0.0–7.0	51	0	**0.0**	0.0–7.0
UCP	51	3	**5.9**	1.2–16.2	51	2	**3.9**	0.5–13.5	51	3	**5.9**	1.2–16.2
VivaChek	48	4	**8.3**	2.3–20.0	48	1	**2.1**	0.1–11.1	48	4	**8.3**	2.3–20.0
WondFo									41	0	**0.0**	0.0–8.6
ELISAs												
Epitope	51	2	**3.9**	0.5–13.5	51	7	**13.7**	5.7–26.3	51	8	**15.7**	7.0–28.6
In-house[b]									51	7	**13.7**	5.7–26.3

[a]Samples are binned by time after patient-reported symptom onset for SARS-CoV-2 RT–PCR-positive cases. Percent of seropositivity assessed by each assay in SARS-CoV-2 RT–PCR-positive samples is reported with 95% CIs. The column 'IgM or IgG' refers to positivity of either isotype. Specificity is determined relative to pre-COVID-19 negative control serum samples. Percent of seropositivity assessed by each assay is reported with 95% CIs for samples from individuals who tested positive for non-SARS-CoV-2 viral infections and/or tested negative for SARS-CoV-2 by RT–PCR. [b]In-house ELISA secondary antibody is directed against human IgG F(ab')₂. Per the manufacturer, some cross-reactivity with IgM and IgA isotypes cannot be excluded.
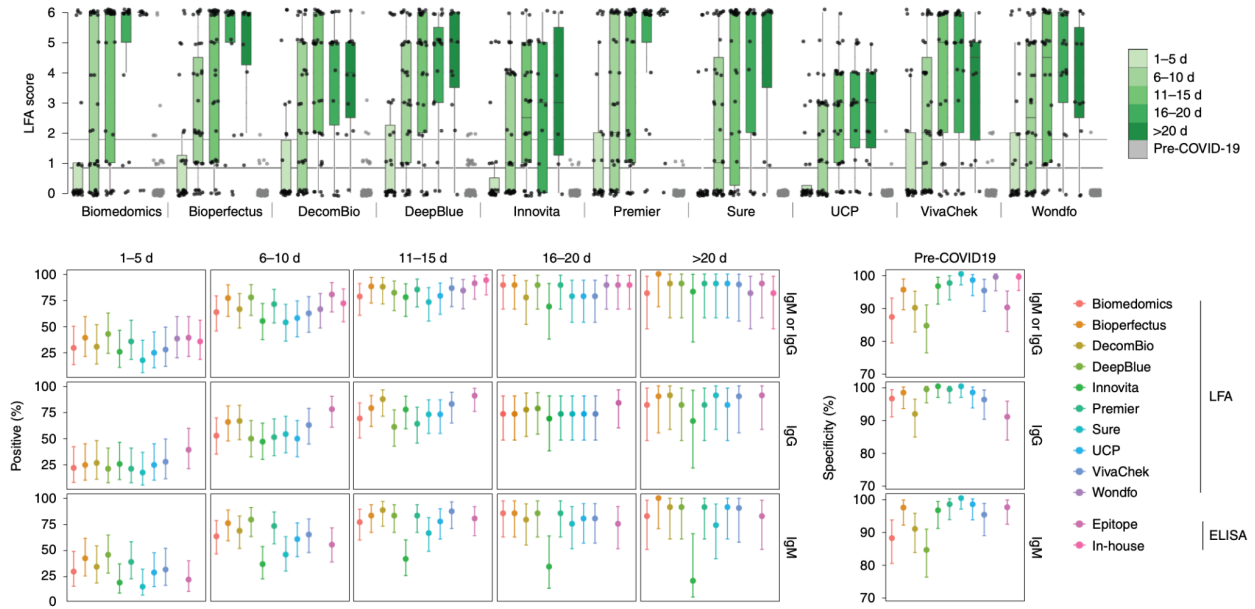
Figure 2.1: Performance data for immunochromatographic LFAs.
a, The second reader's score (0–6 based on band intensity) is reported for each assay, binned by time after patient-reported symptom onset. Biologically independent samples for each test are as follows: n= 126, Biomedomics; n= 126, Bioperfectus; n= 124, DecomBio; n= 128, DeepBlue; n= 114, Innovita; n= 127, Premier; n= 127, Sure; n= 128, UCP; n= 119, VivaChek; n= 124, Wondfo. The second reader's score for pre-COVID-19 samples is also displayed (n= 107, Biomedomics; n= 104, Bioperfectus; n= 107, DecomBio; n= 108, DeepBlue; n= 108, Innovita; n= 108, Premier; n= 108, Sure; n= 107, UCP; n= 99, VivaChek; n= 106, Wondfo). For tests with separate IgG and IgM bands, the higher score is reported. Joint IgM/IgG signal is represented by a single band in Wondfo. The lower, dark gray line refers to the positivity threshold (score greater than or equal to 1) used in this study. The upper, light gray line refers to an alternative positivity threshold (score greater than or equal to 2) discussed in the text and Fig 2.3. Box spans 25th to 75th percentiles with median indicated by the black bar; whiskers show maximum and minimum value within 1.5× the interquartile range from the box. b, Percent of SARS-CoV-2 RT–PCR-positive samples testing positive by each LFA and ELISA are plotted relative to time after patient-reported symptom onset (n= 126, Biomedomics; n= 126, Bioperfectus; n= 124, DecomBio; n= 128, DeepBlue; n= 114, Innovita; n= 127, Premier; n= 127, Sure; n= 128, UCP; n= 119, VivaChek; n= 124, Wondfo; n= 128, Epitope; n= 128, in-house). The 'IgM or IgG' category refers to positivity of either isotype. c, Specificity is plotted for each test using pre-COVID-19 negative control samples (n= 107, Biomedomics; n= 104, Bioperfectus; n= 107, DecomBio; n= 108, DeepBlue; n= 108, Innovita; n= 108, Premier; n= 108, Sure; n= 107, UCP; n= 99, VivaChek; n= 106, Wondfo; n= 108, Epitope; n= 108, in-house). For b and c, all nodes refer to the calculated percent positivity or specificity, respectively. Error bars signify 95% CIs.
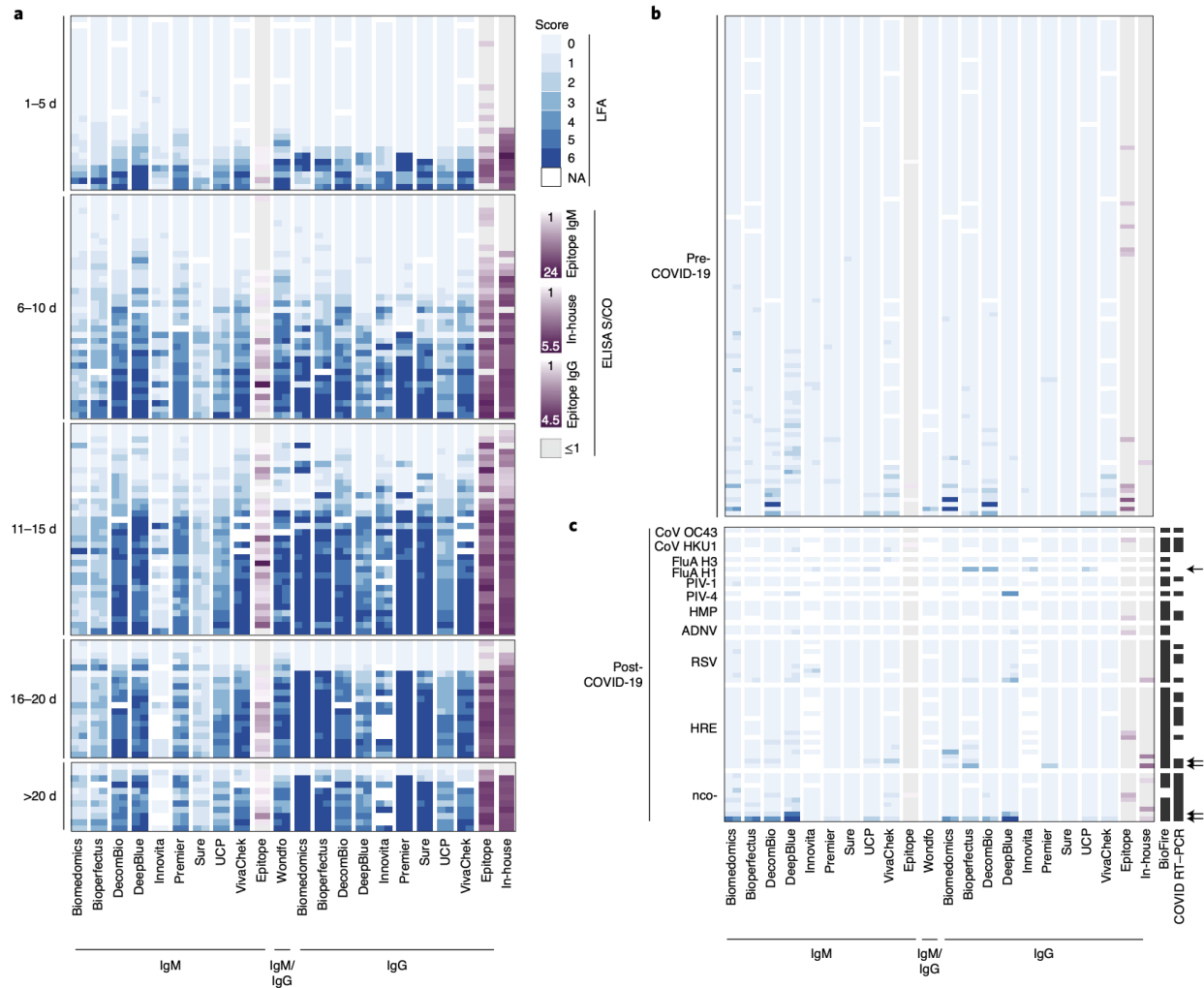
Figure 2.2: LFA and ELISA values by serological assay.

a, LFA scores for each of two readers (blue) and mean ELISA S/CO (purple) for each specimen are grouped by binned time after patient-reported symptom onset and plotted by assay. White cells indicate samples not run with the corresponding assay. For ELISAs, gray indicates S/CO less than or equal to 1. The same legend applies to b and c. The F(ab′)2 specific secondary antibody used in our in-house ELISA preferentially binds the IgG light chain but per the manufacturer has some reactivity for other isotypes (IgM and IgA). b, LFA score and ELISA S/CO values are plotted for pre-COVID-19 historical control serum samples to determine assay specificity. c, LFA score and ELISA S/CO values are plotted for serum samples obtained from 51 individuals after the emergence of COVID-19 (post-COVID-19), some of which received BioFire FilmArray (BioFire Diagnostics) and/or SARS-CoV-2 RT–PCR testing (all negative) as indicated (black cells) in the appropriate columns. Arrows highlight specimens from five individuals with moderate to strong band intensity further discussed in the text. Specimens are grouped by positive testing for coronavirus HKU1 (CoV HKU1), coronavirus OC43 (CoV OC43), influenza A virus A/H3 (FluA H3), influenza A virus A/H1 2009 (FluA H1), parainfluenza type 1 virus (PIV-1), parainfluenza type 4 virus (PIV-4), human metapneumovirus (HMP), adenovirus (ADNV), respiratory syncytial virus (RSV), human rhinovirus/enterovirus (HRE) or negative testing for SARS-CoV-2 and other viruses (nco-).
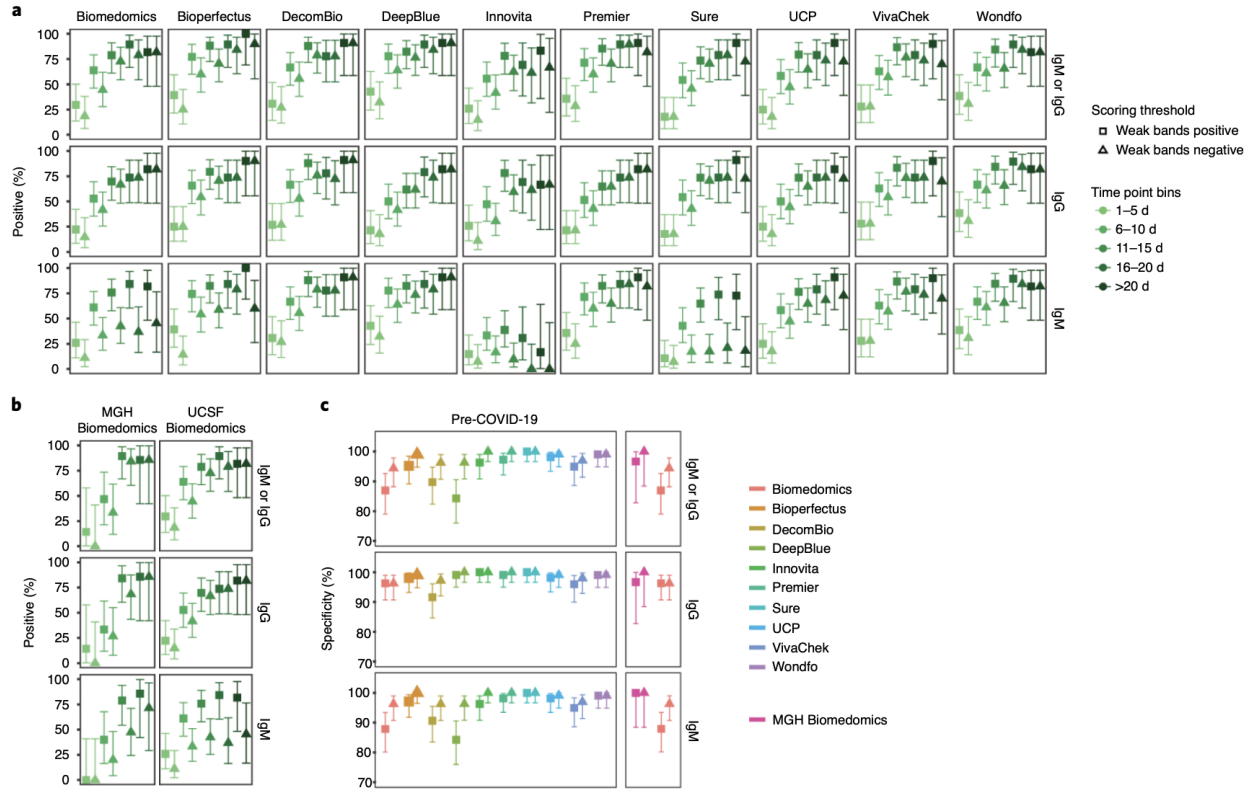
Figure 2.3: Comparison of the effect of different positivity thresholds on percent positivity and specificity.

a, The percent positivity of each assay tested on serum from patients who tested positive for SARS-CoV-2 by RT–PCR is plotted by time after patient-reported symptom onset. Biologically independent samples for each test are as follows: n= 126, Biomedomics; n= 126, Bioperfectus; n= 124, DecomBio; n= 128, DeepBlue; n= 114, Innovita; n= 127, Premier; n= 127, Sure; n= 128, UCP; n= 119, VivaChek; n= 124, Wondfo. Squares indicate percent positivity using reader score >0 ('Weak bands positive') as the positivity threshold. Triangles indicate percent positivity using reader score >1 ('Weak bands negative') as the positivity threshold. 'IgM or IgG' signifies detection of either isotype. Wondfo reports a single band for IgM and IgG together, and the results are plotted here as both 'IgM' and 'IgG' for horizontal comparison across assays. b, Comparison of percent positivity at each timepoint for BioMedomics assay at either the MGH (left, n= 48) or UCSF (right, n= 126) study site using low (square) or high (triangle) positivity thresholds. Note that a weak score at MGH is not directly equivalent to a 1 at UCSF owing to differences in reader training. c, The specificity of all assays on historical pre-COVID-19 serum using low (square) or high (triangle) positivity thresholds. UCSF BioMedomics data are plotted again in the right subpanel column for direct comparison to MGH BioMedomics data. All nodes refer to the calculated percent positivity or specificity (as designated), and all error bars indicate 95% CIs.

35
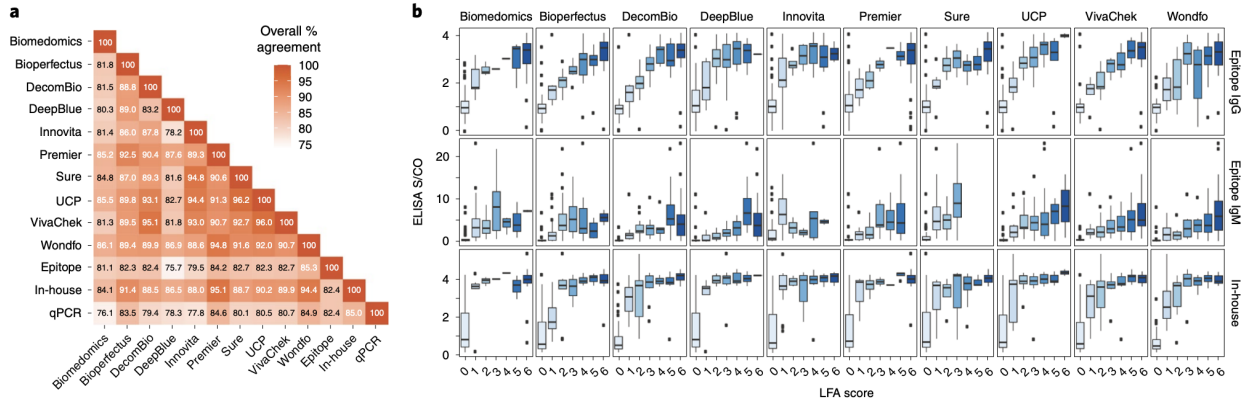
Figure 2.4: Agreement of serological assays for SARS-CoV-2.

a, Percent agreement is plotted across all assay combinations, and values signify the binomial regression of the two assays across all tests. Samples were labeled 'positive' if any antibody isotype was detected for each assay. b, IgM or IgG LFA scores for each assay are compared to S/CO from three different ELISAs for all SARS-CoV-2 RT–PCR-positive samples. Biologically independent samples for each test are as follows: n= 126, Biomedomics; n= 126, Bioperfectus; n= 124, DecomBio; n= 128, DeepBlue; n= 114, Innovita; n= 127, Premier; n= 127, Sure; n= 128, UCP; n= 119, VivaChek; n= 124, Wondfo. Joint IgM/IgG signal is represented by a single band in Wondfo, so data were plotted as IgM or IgG depending on ELISA comparison. The F(ab′)2-specific secondary antibody used in our in-house ELISA preferentially binds the IgG light chain but per the manufacturer contains some reactivity for other isotypes (IgM and IgA); it is compared in b to IgG band intensity. For b, the box spans the 25th to 75th percentiles with median indicated by the black bar; whiskers show maximum and minimum value within 1.5× the interquartile range from the box.

Table S2.1: Immunoassay Kit and Manufacturer Information. Bold signifies labels used in text and figures.

Assay	Supplier	Product	Antigen*	Format**	Lot(s)	Product Number	Distributor	Kit Acquisition for Study	Performance Notes
LFAs	**BioMedomics** Inc, Morrisville, NC, USA	COVID-19 IgM-IgG Rapid Test	RBD	1	20200 32103	51-002-20	Henry Schein, Melville, NY, USA	Provided by Distributor Free of Charge	Some control band inconsistency
	Bioperfectus Technologies Co Ltd, Jiangsu, China	PerfectPOC Novel Corona Virus (SARS-CoV-2) IgM/IgG Rapid Test Kit	NP, SP	1	20200 313, 20200 313, 20210 312	SC30201 W	--------	Provided by Supplier Free of Charge	Extra diluent necessary
	Decombio Biotechnology Co Ltd, Beijing, China	Novel Coronavirus (SARS-CoV-2) IgM/IgG Combo Rapid Test-Cassette	--------	1	--------	--------	--------	Provided by Supplier Free of Charge	Some control band inconsistency
	DeepBlue Medical Technology Co Ltd, Anhui, China	COVID-19 (SARS-CoV-2) IgG/IgM Antibody Test Kit (Colloidal Gold)	--------	1	20200 305	--------	--------	Donated by John Hering, who purchased from supplier	Extra diluent necessary, Some control band inconsistency
	Innovita Biological Technology Co Ltd, Qian'an, China	Novel Coronavirus (2019-nCoV) Ab Test (Colloidal Gold)	NP, SP	2	20200 304	--------	20/20 GeneSystems, Rockville, MD, USA	Purchased from Distributor	Some band smearing
	Premier Biotech, Minneapolis, MN, USA	COVID-19 IgG/IgM Rapid Test Cassette	--------	1	COV2 00300 71	INGM-MC42S	--------	Purchased from Supplier	Some band smearing
	Sure Biotech, New York, NY, USA; Wan Chai, Hong Kong	SARS-CoV-2 IgM/IgG Antibody Rapid Test	NP, SP	1	COV1 25200 3B	VC01210 3	--------	Provided by Supplier Free of Charge	--------
	UCP Biosciences, San Jose, CA, USA	Coronavirus IgG/IgM Antibody (COVID-19) Test Cassette	--------	1	SMP2 02003 12, SMP2 02003 13	U-CoV-102	--------	Provided by Supplier Free of Charge	Extra diluent necessary
	VivaChek Biotech Co, Hangzhou, China	VivaDiag™ SARS-CoV-2 IgM/IgG Rapid Test (COVID-19 IgM/IgG Rapid Test)	--------	1	E2003 002	VID35-08-011	Everest Links Pte Ltd, Singapore	Purchased from Distributor	Some band smearing
	Wondfo Biotech Co Ltd, Guangzhou, China	SARS-CoV-2 Antibody Test (Lateral Flow Method)	--------	3	W195 00318	W195	--------	Donated by David Friedberg, who purchased from supplier	Some band smearing
MGH LFAs	**SD Biosensor**, Suwon-si, Gyeonggi-doz, Republic of Korea	STANDARD Q COVID-19 IgM/IgG Duo	NP	2	QCO1 02000 6	Q-NCOV-01D	Henry Schein, Melville, NY, USA	Provided by Distributor Free of Charge	--------
	Biolidics Limited, Mapex, Singapore	2019-nCoV IgG/IgM antibody detection kit	NP, RBD	1	V2020 0330	CBB-F015016-V	--------	Purchased from Supplier	--------
	Biomedomics Inc, Morrisville, NC, USA	COVID-19 IgM and IgG Rapid Test	RBD	1	20200 22702 20200 32103	51-002-20	Henry Schein, Melville, NY, USA	Lot 1 provided by Distributor Free of Charge; Lot 2 purchased from Supplier	--------
ELISAs	**Epitope** Diagnostics, San Diego, CA, USA	KT-1033 EDI™ Novel Coronavirus COVID-19 **IgM** ELISA Kit	NP	--	P630C	KT-1032	--------	Purchased from Supplier	--------
	Epitope Diagnostics, San Diego, CA, USA	KT-1032 EDI™ Novel Coronavirus COVID-19 **IgG** ELISA Kit	NP	--	P637U	KT-1033	--------	Purchased from Supplier	--------
	In-House ELISA	Peroxidase AffiniPure Goat Anti-human IgG (F(ab')2 specific) secondary antibody (Jackson ImmunoResearch)	RBD	--	14657 6	109-035-097	Adapted from Krammer Lab, Icahn School of Medicine at Mt. Sinai, New York, NY, USA	Lab-developed test	--------

*Antigen:
NP = Nucleocapsid protein
SP = Spike protein
RBD = Receptor binding domain, Spike protein
**LFA Test Cartridge Format:
1: Single lane, separate IgM and IgG bands
2: Separate IgM and IgG lanes
3: Single lane, single band for both IgM and IgG

Table S2.2: Reader Agreement on Immunochromatographic Lateral Flow Assays (LFAs).
Cohen's Kappa correlations were calculated for scores of the IgG band (left) and IgM band (right) of each LFA. The LFA manufactured by Wondfo has a single band for IgG and IgM detection and is displayed here as IgG for convenience. Positive Kappa Correlation: unweighted inter-reader agreement on positive (LFA score > 0) vs. negative (LFA score = 0) reads. Weighted Kappa Correlation: inter-reader agreement on LFA score (0-6), weighted by the square of the difference in reads. All correlations were calculated with the irr package version 0.84.1 in R version 3.6.1 using RStudio.

		IgG			IgM	
Supplier	n	Positive Kappa Correlation	Weighted Kappa Correlation	n	Positive Kappa Correlation	Weighted Kappa correlation
BioMedomics	284	0.9649	0.9580	284	0.8238	0.8253
Bioperfectus	275	0.9586	0.9488	275	0.9130	0.8631
DecomBio	282	0.9761	0.9529	282	0.9845	0.9660
DeepBlue	287	0.9547	0.8971	287	0.9213	0.9377
Innovita	250	0.9588	0.8490	249	0.8084	0.8029
Premier	286	0.9718	0.9880	286	0.9680	0.9340
Sure	286	0.9908	0.9665	286	0.9300	0.7967
UCP	286	0.9565	0.9574	286	1.0000	0.9484
VivaChek	266	0.9912	0.9669	266	0.9332	0.9439
Wondfo*	271	0.9916	0.9542	-	-	-

*Wondfo kits detect combined IgG and IgM.

Table S2.3: Assay performance on validation cohort performed at MGH using positivity thresholds based on concordance studies to an MGH-group in-house ELISA.

Comparison of MGH and UCSF percent positivity at different positivity thresholds is performed in Supplementary Figure 2.4. Note, the one negative patient included in the >16-day timepoint was immunocompromised.

Assay	Total N	IgM positive	%	95% CI Lower	95% CI Upper	Total N	IgG positive	%	95% CI Lower	95% CI Upper	Total N	IgM or IgG positive	%	95% CI Lower	95% CI Upper
LFAs															
SD Biosensor															
1-5 days	7	0	0.00	0.00	40.96	7	1	14.29	0.36	57.87	7	1	14.29	0.36	57.87
6-10 days	15	6	40.00	16.34	67.71	15	5	33.33	11.82	61.62	15	7	46.67	21.27	73.41
11-15 days	19	15	78.95	54.43	93.95	19	16	84.21	60.42	96.62	19	17	89.47	66.86	98.70
>16 days	7	6	85.71	42.13	99.64	7	6	85.71	42.13	99.64	7	6	85.71	42.13	99.64
Pre-COVID-19	60	0				60	1				60	1			
Biolidics															
1-5 days	7	0	0.00	0.00	40.96	7	0	0.00	0.00	40.96	7	0	0.00	0.00	40.96
6-10 days	15	2	13.33	1.66	40.46	15	8	53.33	26.59	78.73	15	8	53.33	26.59	78.73
11-15 days	19	9	47.37	24.45	71.14	19	16	84.21	60.42	96.62	19	16	84.21	60.42	96.62
>16 days	7	4	57.14	18.41	90.10	7	6	85.71	42.13	99.64	7	6	85.71	42.13	99.64
Pre-COVID-19	60	0				60	0				60	0			
BioMedomics															
1-5 days	7	1	14.29	0.36	57.87	7	0	0.00	0.00	40.96	7	1	14.29	0.36	57.87
6-10 days	15	6	40.00	16.34	67.71	15	6	40.00	16.34	67.71	15	7	46.67	21.27	73.41
11-15 days	19	14	73.68	48.80	90.85	19	14	73.68	48.80	90.85	19	15	78.95	54.43	93.95
>16 days	7	6	85.71	42.13	99.64	7	6	85.71	42.13	99.64	7	6	85.71	42.13	99.64
Pre-COVID-19	60	0				60	0				60	0			
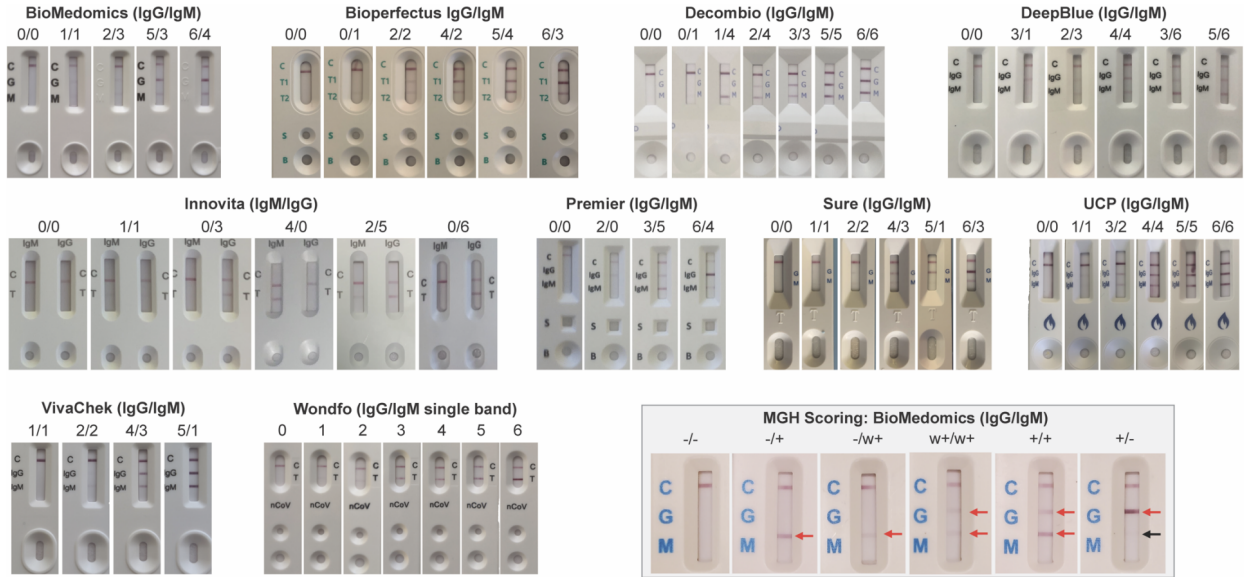
Figure S2.1: Representative images of LFA scoring.

The intensity score is noted at the top of each image for IgG and IgM separately (unless stated otherwise).
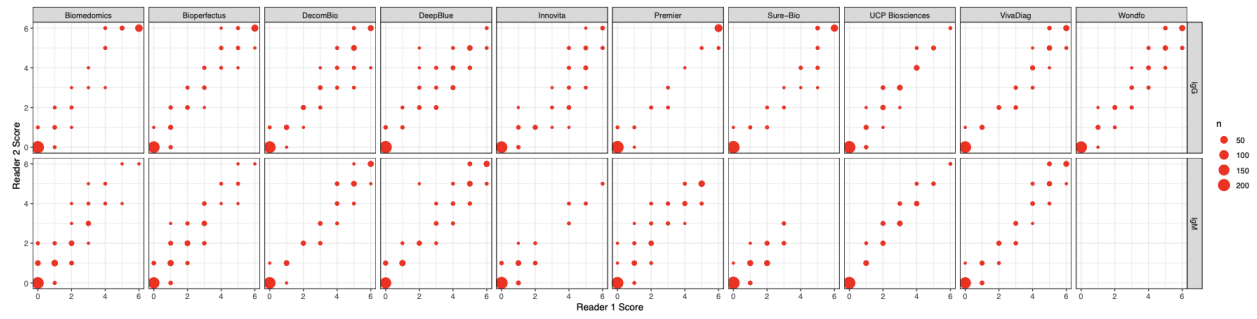
Figure S2.2: Comparison of Reader 1 and Reader 2 LFA scores.
The size of each point signifies the number of tests with the indicated reader 1-to-reader 2 score combination. The LFA manufactured by Wondfo has a single band for IgG and IgM detection and is displayed here as IgG for convenience.
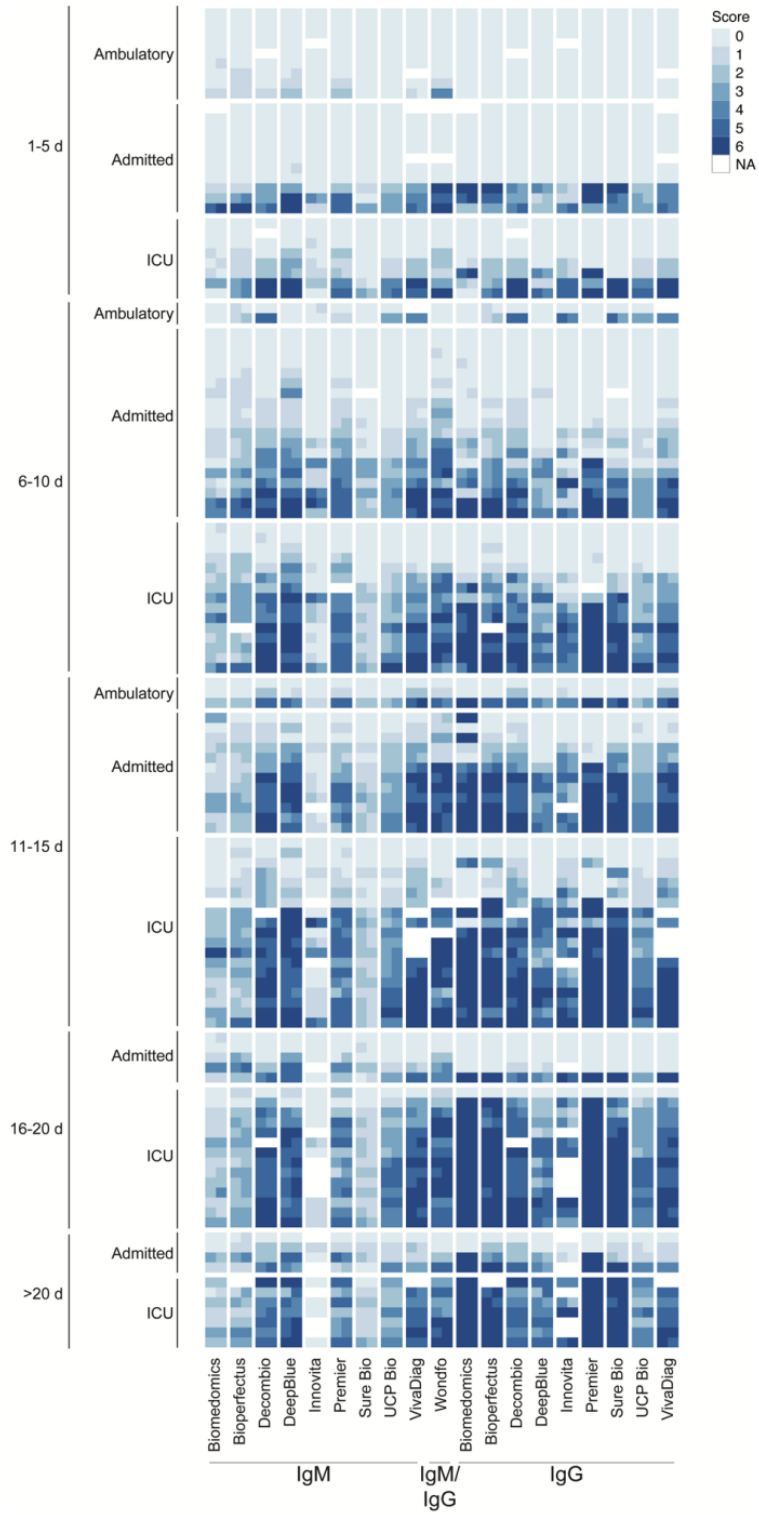
Figure S2.3: LFA scores by serological assay according to highest-level clinical care received by the patient.

2.7: References

1. Johns Hopkins University. COVID-19 Dashboard by the Center for Systems Science and Engineering (CSSE) at Johns Hopkins University (JHU), https://gisanddata.maps.arcgis.com/apps/opsdashboard/index.html#/bda7594740fd4029942 3467b48e9ecf6 (2020).

2. Infectious Diseases Society of America. IDSA Statement on COVID-19 Testing, https://www.idsociety.org/globalassets/idsa/public-health/covid-19-idsa-testing-intro.pdf (2020).

3. Weitz, J. S. et al. Modeling shield immunity to reduce COVID-19 epidemic spread. Nat. Med. https://doi.org/10.1038/s41591-020-0895-3 (2020).

4. World Health Organization. Laboratory Testing for Coronavirus Disease 2019 (COVID-19) in Suspected Human Cases: Interim Guidance, 2 March 2020 (World Health Organization, 2020).

5. Zhao, J. et al. Antibody responses to SARS-CoV-2 in patients of novel coronavirus disease 2019. Clin. Infect. Dis., https://doi.org/10.1093/cid/ciaa344 (2020).

6. Wolfel, R. et al. Virological assessment of hospitalized patients with COVID-2019. Nature https://doi.org/10.1038/s41586-020-2196-x (2020).

7. He, X. et al. Temporal dynamics in viral shedding and transmissibility of COVID-19. Nat. Med. https://doi.org/10.1038/s41591-020-0869-5 (2020).

8. Li, R. et al. Substantial undocumented infection facilitates the rapid dissemination of novel coronavirus (SARS-CoV2). Science https://doi.org/10.1126/science.abb3221 (2020).

9. Bai, Y. et al. Presumed asymptomatic carrier transmission of COVID-19. JAMA https://doi.org/10.1001/jama.2020.2565 (2020).

10. Du, Z. et al. Serial interval of COVID-19 among publicly reported confirmed cases. Emerg. Infect. Dis. https://doi.org/10.3201/eid2606.200357 (2020).

11. Kimball, A. et al. Asymptomatic and presymptomatic SARS-CoV-2 infections in residents of a long-term care skilled nursing facility - King County, Washington, March 2020. MMWR Morb. Mortal. Wkly. Rep. 69, 377–381 (2020).

12. Mizumoto, K., Kagaya, K., Zarebski, A. & Chowell, G. Estimating the asymptomatic proportion of coronavirus disease 2019 (COVID-19) cases on board the Diamond Princess cruise ship, Yokohama, Japan, 2020. Euro. Surveill. https://doi.org/10.2807/1560-7917.ES.2020.25.10.2000180 (2020).

13. Qiu, H. et al. Clinical and epidemiological features of 36 children with coronavirus disease 2019 (COVID-19) in Zhejiang, China: an observational cohort study. Lancet Infect. Dis. https://doi.org/10.1016/S1473-3099(20)30198-5 (2020).

14. Tong, Z. D. et al. Potential presymptomatic transmission of SARS-CoV-2, Zhejiang Province, China, 2020. Emerg. Infect. Dis. 26, 1052–1054 (2020).

15. Secretary of Health and Human Services. Determination of a public health emergency and declaration that circumstances exist justifying authorizations pursuant to section 564(b) of the Federal Food, Drug, And Cosmetic Act, 21 U.S.C. § 360bbb-3. https://www.fda.gov/media/135010/download (2020).

16. Food and Drug Administration. Policy for diagnostic tests for coronavirus disease-2019 during the public health emergency. https://www.fda.gov/media/135659/download (2020).

17. San Francisco Department of Public Health. San Francisco Department of Public Health Annual Report 2017-2018, https://www.sfdph.org/dph/files/reports/PolicyProcOfc/DPHAnnualReportFY17-18.pdf (2018).

18. DataSF. San Francisco COVID-19 Data Tracker, https://data.sfgov.org/stories/s/San-Francisco-COVID-19-Data-Tracker/fjki-2fab/ (2020).

19. Long, Q. X. et al. Antibody responses to SARS-CoV-2 in patients with COVID-19. Nat. Med. https://doi.org/10.1038/s41591-020-0897-1 (2020).

20. Tan, W. et al. Viral kinetics and antibody responses in patients with COVID-19. Preprint at medRxiv https://doi.org/10.1101/2020.03.24.20042382 (2020).

21. Ng, D. et al. SARS-CoV-2 seroprevalence and neutralizing activity in donor and patient blood from the San Francisco Bay Area. Preprint at medRxiv https://doi.org/10.1101/2020.05.19.20107482 (2020).

22. Lynch, K. L. et al. Magnitude and kinetics of anti-SARS-CoV-2 antibody responses and their relationship to disease severity. Preprint at medRxiv https://doi.org/10.1101/2020.06.03.20121525 (2020).

23. U.S. Food and Drug Administration. Emergency Use Authorization, https://www.fda.gov/emergency-preparedness-and-response/mcm-legal-regulatory-and-policy-framework/emergency-use-authorization (2020).

24. Lassaunière, R. et al. Evaluation of nine commercial SARS-CoV-2 immunoassays. Preprint at medRxiv https://doi.org/10.1101/2020.04.09.20056325 (2020).

25. To, K. K. et al. Temporal profiles of viral load in posterior oropharyngeal saliva samples and serum antibody responses during infection by SARS-CoV-2: an observational cohort study. Lancet Infect. Dis. https://doi.org/10.1016/S1473-3099(20)30196-1 (2020).

26. Amanat, F. et al. A serological assay to detect SARS-CoV-2 seroconversion in humans. Nat. Med. https://doi.org/10.1038/s41591-020-0913-5 (2020).

27. Wang, W. et al. Detection of SARS-CoV-2 in different types of clinical specimens. JAMA https://doi.org/10.1001/jama.2020.3786 (2020).

28. Kim, D., Quinn, J., Pinsky, B., Shah, N. H. & Brown, I. Rates of co-infection between SARS-CoV-2 and other respiratory pathogens. JAMA https://doi.org/10.1001/jama.2020.6266 (2020).

29. Jiang, S., Hillyer, C. & Du, L. Neutralizing antibodies against SARS-CoV-2 and other human coronaviruses. Trends Immunol. https://doi.org/10.1016/j.it.2020.03.007 (2020).

30. Nie, J. et al. Establishment and validation of a pseudovirus neutralization assay for SARS-

CoV-2. Emerg. Microbes Infect. 9, 680–686 (2020).

31. Crawford, K. H. D. et al. Protocol and reagents for pseudotyping lentiviral particles with SARS-CoV-2 spike protein for neutralization assays. Viruses https://doi.org/10.3390/v12050513 (2020).

32. Food and Drug Administration. Clinical Laboratory Improvement Amendments (CLIA), https://www.fda.gov/medical-devices/ivd-regulatory-assistance/clinical-laboratory-improvement-amendments-clia (2020).

33. Altmann, D. M., Douek, D. C. & Boyton, R. J. What policy makers need to know about COVID-19 protective immunity. Lancet 395, 1527–1529 (2020).

34. Weinstein, M. C., Freedberg, K. A., Hyle, E. P. & Paltiel, A. D. Waiting for certainty on COVID-19 antibody tests — at what cost? N. Engl. J. Med. https://doi.org/10.1056/NEJMp2017739 (2020).

35. U.S. Food and Drug Administration. Policy for Coronavirus Disease-2019 Tests During the Public Health Emergency (Revised), https://www.fda.gov/regulatory-information/search-fda-guidance-documents/policy-coronavirus-disease-2019-tests-during-public-health-emergency-revised (2020).

36. National Cancer Institute. NCI Part of Federal Effort to Evaluate Antibody Tests for Novel Coronavirus, https://www.cancer.gov/news-events/cancer-currents-blog/2020/covid-19-nci-antibody-testing-review (2020).

37. Whitman, J. D. et al. Chagas disease serological test performance in United States blood donor specimens. J. Clin. Microbiol. https://doi.org/10.1128/JCM.01217-19 (2019).

Chapter 3: Improved COVID-19 Serology Test Performance by Integrating Multiple Lateral Flow Assays using Machine Learning

This Chapter is publicly available as:

Cody T. Mowery, Alexander Marson, Yun S. Song, Chun Jimmie Ye. Improved COVID-19 Serology Test Performance by Integrating Multiple Lateral Flow Assays using Machine Learning. *medRxiv,* 2020.

3.1: Abstract

Mitigating transmission of SARS-CoV-2 has been complicated by the inaccessibility and, in some cases, inadequacy of testing options to detect present or past infection. Immunochromatographic lateral flow assays (LFAs) are a cheap and scalable modality for tracking viral transmission by testing for serological immunity, though systematic evaluations have revealed the low performance of some SARS-CoV-2 LFAs. Here, we re-analyzed existing data to present a proof-of-principle machine learning framework that may be used to inform the pairing of LFAs to achieve superior classification performance while enabling tunable False Positive Rates optimized for the estimated seroprevalence of the population being tested.

3.2: Main

The SARS Coronavirus-2 (SARS-CoV-2) has emerged rapidly and precipitated the Coronavirus Disease 2019 (COVID-19) pandemic that continues to threaten vulnerable populations and disrupt daily life [5]. Although definitive evidence of antibody-mediated protective immunity against SARSCoV-2 infection is still needed [10, 14], promising early results from trials of convalescent plasma therapy [4] and animal re-infection models [2] raise hopes that antibodies can confer some degree of protection. Because infected individuals nearly uniformly mount detectable serological responses against SARS-CoV-2 [9], sensitive and specific measurement of anti-SARS-CoV-2 serostatus is critical for obtaining accurate estimates of natural immunity (prevalence), as well as infection rates (incidence). Thus, reliable serology tests may provide important epidemiological information to model viral spread and inform non-pharmaceutical interventions including physical distancing and contact tracing.

A number of immunochromatographic lateral flow assays (LFAs) and enzyme-linked immunosorbence assays (ELISAs) were developed swiftly to detect antibodies against SARS-CoV-2 antigens. Recent work by our group and others has revealed potentially inadequate

sensitivity and specificity of some of these LFAs [1, 6, 16], suggesting that uninformed usage of these tests could result in inaccurate estimates of seroprevalence or release of misleading information to tested individuals. Although select LFAs perform relatively well, no single LFA is both perfectly sensitive and specific. ELISAs tend to perform better, but they require specialized laboratory equipment that limit their widespread adoption. Because LFAs remain accessible and can be deployed in point-of-care settings, rational LFA deployment may improve diagnostic performance while retaining scalability and ease of use.

Clinical testing methods incorporating multiple laboratory assays achieve superior performance by leveraging the unique strengths of different assays, as is standard practice for HIV testing [8]. Because LFAs utilize a range of antigens and chemistries, we hypothesize that testing with pairs of SARS-CoV-2 LFAs may classify specimen serostatus better than single LFAs. To test our hypothesis, we compare the performance of single LFAs with that of LFA pairs using a simple strategy requiring positive results from both LFAs (AND logic). Although the AND logic strategy is able to reduce the false positive rate (FPR), it is accompanied by a substantial reduction in true positive rate (TPR) (i.e., sensitivity or power), in some cases to levels below the performance of individual LFAs.

To overcome the limitations of the simple AND logic strategy, we demonstrate a proof-of-concept machine-learning classifier that combines the information of semi-quantitative readouts from both IgM and IgG tests to control the FPR at a targeted level while achieving higher TPRs than individual LFAs. Importantly, our classifier obtained the largest TPR gains when low-performing LFAs are combined, thus significantly expanding their utility. The ability to tune the FPR could enable the deployment of LFA pairs across a range of prior probabilities of seropositivity, and facilitate sound statistical comparisons of different tests. We offer a principled framework that may be used to identify well-performing LFA pairs for studies of individual- and population-level immunity, effectively expanding the SARS-CoV-2 immunity testing options to increase testing scalability and distribute supply demands across multiple vendors.

3.3: Results

We re-analyzed recently generated data [16] that examined the performance of SARS-CoV-2 LFAs from 10 vendors (19 tests based on separate IgM and IgG detection for 9/10 assays) scored by two independent readers (Table 3.S1) using a validated semi-quantitative scoring scale [15] with the positivity threshold of ≥1 (Figure 3.1a-b: "IgM only" & "IgG only"). Here, we use the term "test" to indicate individual IgM or IgG results, and the terms "LFA" and "vendor" to reference the integrated result of IgM and IgG when interpreted together.

First, we determined whether a simple LFA pairing strategy improves specimen classification performance as measured by the F1 score, a well-used evaluation metric in machine learning (see Supplemental Methods). For each LFA, we combined the IgM and IgG results, calling the specimen "positive" if either the IgM or IgG test result is above the positivity threshold (≥1) used in the source publication [16] (Figure 3.1a-b: "Single LFA"). We find that combining IgM and IgG results for each LFA improves the F1 score relative to IgM or IgG alone (mean: 88% vs. 81% & 84%, respectively, Figure 3.1b) by primarily improving TPR (mean: 84% vs. 76% & 77%, respectively, Figure 3.S1). Subsequently, we examined all possible LFA pairs to determine whether requiring concordant positivity of two LFAs (AND logic) would improve sample classification. This strategy resulted in no improvements in F1 scores compared to single LFAs (mean: 88%, Figure 3.1b) but lowered the TPR (mean: 80%, Figure 3.S1).

This decrease in TPR revealed a vulnerability of the AND logic pairing approach to unforeseen negative combination effects, thus motivating us to explore more sophisticated pairing strategies. We evaluated several machine learning classifiers (including random forest, logistic regression, and gradient boosting) using semi-quantitative readouts of LFA test intensities rather than binarized data. We found gradient boosted decision trees (implemented in XGBoost [3], see Supplemental Methods) worked particularly well, so we focused on this approach. Our XGBoost classifier integrates the IgM and IgG test results for each LFA and outputs a probability of positivity

for each specimen. Thus, the trade-off between TPR and FPR can be tuned by applying a different probability threshold in accordance with the needs of the user and the prior probability of seropositivity in the test population [16]. Whereas the heterogeneous FPRs reported across different single and AND logic-paired LFAs complicates TPR comparisons (Figure 3.S1), controlling the FPR at a desired significance level α using a machine-learning classifier enables direct TPR comparisons and, thus, identification of high-performing single and paired LFAs.

We first assessed the overall performance (F1 score) of the XGBoost classifier at a fixed probability threshold of 0.5. We find that processing single LFAs with XGBoost (mean: 89%, Figure 3.1a-b: "Single LFA + ML") outperforms simple single IgM or IgG tests, single LFAs, and AND logic LFA pairs mentioned previously. Further, combining LFAs with XGBoost further improves F1 scores (mean: 90%, Figure 3.1a-b: "LFA Pair + ML"). Leveraging the aforementioned ability to tune the FPR, we next examined the TPR performance for individual LFAs at fixed significance levels α = 1.5% (Figure 3.1c: diagonal, see Supplemental Methods), 3% (Figure 3.S2a), and 4.5% (Figure 3.S2b). At α = 1.5%, we found that XGBoost roughly segregates LFAs from different vendors into three TPR ranges: low (< 70%, light grey bar), mid (70–80%, grey), and high (> 80%, dark grey). Pairing different LFAs with XGBoost (mean: 81%, Figure 3.1c: off-diagonal) achieves higher TPRs than single vendor XGBoost classifiers (mean: 71%, Figure 3.1c: diagonal) at the same FPR threshold. We found that vendors that perform well individually (e.g., Vendors 7 & 8) perform marginally better in combination (82% combined vs. 79% & 79% individually). Importantly, LFAs that are lower performers alone (e.g., Vendors 2 & 3) can be paired to achieve significant performance gains over each individual LFA (78% combined vs. 61% & 61% individually) and/or confer modest gains on already mid-performing LFAs (e.g., Vendor 8: 79% individually vs. 83% with Vendor 2 and 84% with Vendor 3). Similarly, two mid-performing LFAs (e.g., Vendors 5 & 8) could be paired to achieve performance in the range of single high-performing LFAs (85% vs. 73% & 79% individually). These effects are not merely additive. For example, certain LFAs enhance the performance of Vendor 10 more than others despite mid-

level performance alone; e.g., at significance level α = 1.5%, Vendor 9 (80%) performs better than Vendor 6 (77%) individually, but combining Vendors 6 and 10 (91%) is better than Vendors 9 and 10 (89%). These results demonstrate a proof-of-concept implementation of a machine-learning classifier that can effectively identify specific LFA pairs with better classification performance overall and increased sensitivity at a tuned False Positive Rate.

3.4: Discussion

Here, we have demonstrated the utility of machine learning to enhance performance and inform deployment of lateral flow assays (LFAs) for anti-SARS-CoV-2 antibodies. LFAs will likely be integral for accurate estimation of population seroprevalence to inform public health directives, especially in settings where specialized equipment is unavailable [13]. We found that training an optimized gradient boosted decision tree algorithm on LFA pairs has higher classification performance (F1 score) than single LFA tests and a more naive LFA pairing strategy. Though LFAs for anti-SARS-CoV-2 antibody detection are likely to improve with time, our framework provides an alternative LFA deployment strategy until a "perfect" SARS-CoV-2 immunoassay is widely available. This computational approach will likely improve the performance of other immunoassays, including SARS-CoV-2 rapid antigen tests and serological assays for other conditions, though the method should be thoroughly validated on a case-by-case basis.

In addition to its superior performance, one of the primary advantages of using a machine learning classifier is the ability to tune the target False Positive Rates in accordance to the population in which the LFAs are being deployed. Given the geographic variability of SARS-CoV-2 prevalence [5], a more stringent FPR may be implemented in low prevalence settings where the pre-test probability is exceedingly low. Conversely, high prevalence populations may be more effectively screened by implementing a classifier that prioritizes higher TPR at the cost of specificity. Such threshold tuning is dependent upon the use of a (semi)quantitative LFA scoring

strategy [16], as categorical input data (e.g., "Positive" or "Negative") cannot be effectively optimized by the classifier. Objective LFA scoring in the form of automated densitometry or an image processing algorithm would be ideal to provide continuous scoring data on which a machine learning classifier can be trained, but, in the absence of this technology, we advocate for use of a validated semi-continuous scoring system to be used by trained readers for optimal results.

Our calculations likely underestimate True Positive Rate given the absence of a gold-standard SARS-CoV-2 immunoassay to identify seroconverted patient specimens. As discussed in our previous work [16], the use of SARS-CoV-2 RT-PCR to classify positive and negative specimens (with the exception of historical, pre-SARS-CoV-2 negative samples) almost certainly includes specimens that have not yet seroconverted. Here, we enrich for seropositive specimens by subsetting to specimens collected 10 or more days after symptom onset [6] (see Supplemental Methods), but we do not have sufficient late timepoint data to more stringently select for seropositivity [7, 9].

LFA batch variability, ongoing assay development, and small sample size preclude our ability to nominate specific LFA combinations for real-world implementation. Rather, we propose here a conceptual framework by which healthcare systems and governmental organizations performing independent LFA evaluations can improve the performance of SARS-CoV-2 immunoassays using machine learning. We demonstrate the approach using a popular machine learning classifier trained on a rather small data set. Although this small sample size limits our ability to explore FPRs lower than 1.5% (see Supplemental Methods), our results demonstrate increased TPR gains with combination testing as the targeted FPR level decreases (Figure 3.1c, S2). We anticipate that using a model trained on larger data should lead to improved performance and further aid researchers in selecting high-utility LFAs from a collection of evaluated vendors. Additional assay information, including the SARS-CoV-2 antigen bait and secondary antibody detection reagents used in each cartridge, will likely further improve performance by identifying

co-linearity and, thus, more effectively identify useful LFA combinations by de-prioritizing those unlikely to enhance one another.

Informed combination LFA testing could help to minimize supply chain limitations by spreading the burden of meeting the world's SARS-CoV-2 testing demand across multiple manufacturers and LFA vendors. In doing so, our work could effectively expand the number of acceptable SARSCoV-2 immunoassay testing options, serving as a proof of principle demonstrating the utility of combination LFA testing for more accurate determination of anti-SARS-CoV-2 antibody status.

3.5: Methods

True Positive Rate (TPR) is reported with respect to 79 specimens collected from SARS-CoV-2 RT-PCR-positive patients 10 days or more after patient-reported symptom onset. False Positive Rate (FPR) is estimated against 31 specimens from SARS-CoV-2 RT-PCR-negative patients and 108 specimens from pre-July 2018 historical negative controls.

LFAs were scored using a validated 0-6 LFA scoring strategy [15], and a positivity threshold of ≥ 1 [16] was used for non-machine learning results (Figure 3.1a-b: "IgM only", "IgG only", "Single LFA", and "LFA Pair"). Missing LFA scores for each vendor (0–15.3% of all specimens, mean: 3.4%, SD: 4.6%) from two independent readers were imputed using a k-nearest neighbors algorithm [12], and for each sample the average of the two scores was used for downstream analyses. Pre-processing with imputation and score averaging does not significantly improve baseline TPR (p = 0.27, Mann–Whitney U test) or FPR (p = 0.60, Mann–Whitney U test) performance metrics of tests with missing data (Table 3.S1).

We employed balanced F-score (F1 score), a widely-used measure of classification performance in machine learning, to compare the performance of different experiments at divergent false positive rates. It is defined as

$$F_1 = \cfrac{2}{\cfrac{1}{precision} + \cfrac{1}{recall}}$$

or the harmonic mean of precision (the fraction of true positives among all instances called as positive, or Positive Predictive Value) and recall (TPR, sensitivity, or power).

We implemented an ensemble machine learning classifier using the eXtreme Gradient Boosting (XGBoost) package [3] with 'gbtree' booster and 'binary:logistic' objective. This method uses both IgM and IgG test results for each LFA and iteratively generates, evaluates, and refines decision trees to optimize for accurate "positive" or "negative" specimen classification. We trained the XGBoost classifier on 50% of data, used 3-fold cross validation to tune its hyperparameters (max_depth, min_child_weight, lambda, subsample, colsample_bytree), and then tested the trained model on the remaining 50% of data. We repeated this experiment 100 times each with different random splits of data into training and test sets, and computed average TPRs at fixed significance levels α = 1.5% (Figures 1c), 3%, and 4.5% (Figure 3.S2). Given this train-test split, the lowest possible non-zero FPR that could be considered when testing 50% of the 139 negative specimens is $1/(0.5 × 139) ≈ 0.015$.

All analyses were performed in Python using the scikit-learn library [11] (except where otherwise specified).

Acknowledgements

Administration. The information presented here does not necessarily reflect the position or the policy of the Government and no official endorsement should be inferred. A.M. and Y.S.S. are Chan Zuckerberg Biohub Investigators, and C.J.Y. is a Chan Zuckerberg Biohub Intercampus Research Award Investigator.

Disclosures

3.6: Figures

Figure 3.1: Comparative performance of LFA combination strategies.

a. Schematic describing data reported in b, including baseline performance characteristics for IgM ("IgM only", n = 9) and IgG ("IgG only", n = 9) tests for each LFA. For single ("Single LFA", n = 10) and paired ("LFA Pair", n = 45) LFAs, specimens were classified as positive if either IgM or IgG test was positive for each LFA. Machine learning (XGBoost) classifier receives both IgM and IgG test information for either single ("Single LFA + ML", n = 10) or paired ("LFA Pair + ML", n = 45) LFAs. b. Balanced Fscore (or F1 score) for each experiment outlined in A. One "IgM only" outlier (F1 = 0.49) is cut off for visualization purposes. The Wondfo LFA was excluded from "IgM only" and "IgG only" because a single band reports signal from both IgM and IgG isotypes. The vertical black bars indicate the range from first to third quartiles, white points indicate mean values, and horizontal bars indicate median values. c. Pairwise vendor (V1-V10) TPR performance for XGBoost classifier at α = 0.015, binned as low (light grey bar), medium (grey bar), or high (dark grey bar) TPR performance. The diagonal (black outline) specifies TPR results for single LFAs, whereas off-diagonal results reflect TPR of LFA pairs. The reported TPRs were averaged over 100 different random splits of data into 50% training and 50% test sets (see Supplemental Methods).

Table S3.1: Comparative LFA performance.

Comparing scores from a single reader ("Reader2"), averaged scores from two independent readers ("Mean"), or averaged scores from two independent readers after imputation ("Imputed").

	False Positive Rate (FPR)						True Positive Rate (TPR)					
	IgM			IgG			IgM			IgG		
Vendor	Reader2	Mean	Imputed	Reader2	Mean	Imputed	Reader2	Mean	Imputed	Reader2	Mean	Imputed
Bioperfectus	0.062	0.039	0.036	0.047	0.047	0.043	0.872	0.846	0.848	0.821	0.808	0.810
Sure	0.000	0.000	0.000	0.000	0.000	0.000	0.671	0.658	0.658	0.760	0.747	0.747
UCP	0.029	0.029	0.029	0.022	0.022	0.022	0.810	0.810	0.810	0.747	0.747	0.747
DeepBlue	0.180	0.151	0.151	0.036	0.029	0.029	0.861	0.848	0.848	0.696	0.684	0.684
DecomBio	0.101	0.094	0.093	0.073	0.065	0.065	0.870	0.870	0.873	0.870	0.857	0.861
Innovita	0.033	0.008	0.007	0.000	0.000	0.000	0.369	0.369	0.329	0.742	0.742	0.760
Premier	0.022	0.022	0.022	0.014	0.014	0.014	0.861	0.848	0.848	0.709	0.709	0.709
BioMedomics	0.130	0.087	0.086	0.044	0.044	0.043	0.795	0.756	0.747	0.744	0.744	0.747
VivaChek	0.062	0.062	0.058	0.039	0.039	0.036	0.851	0.851	0.861	0.824	0.811	0.823
Mean	0.069	0.055	0.054	0.030	0.029	0.028	0.773	0.762	0.758	0.768	0.761	0.765
SD	0.058	0.049	0.049	0.024	0.022	0.021	0.155	0.152	0.165	0.055	0.051	0.053

	IgM & IgG						IgM & IgG		
Vendor	Reader2	Mean	Imputed				Reader2	Mean	Imputed
Wondfo	0.008	0.008	0.007				0.870	0.870	0.873
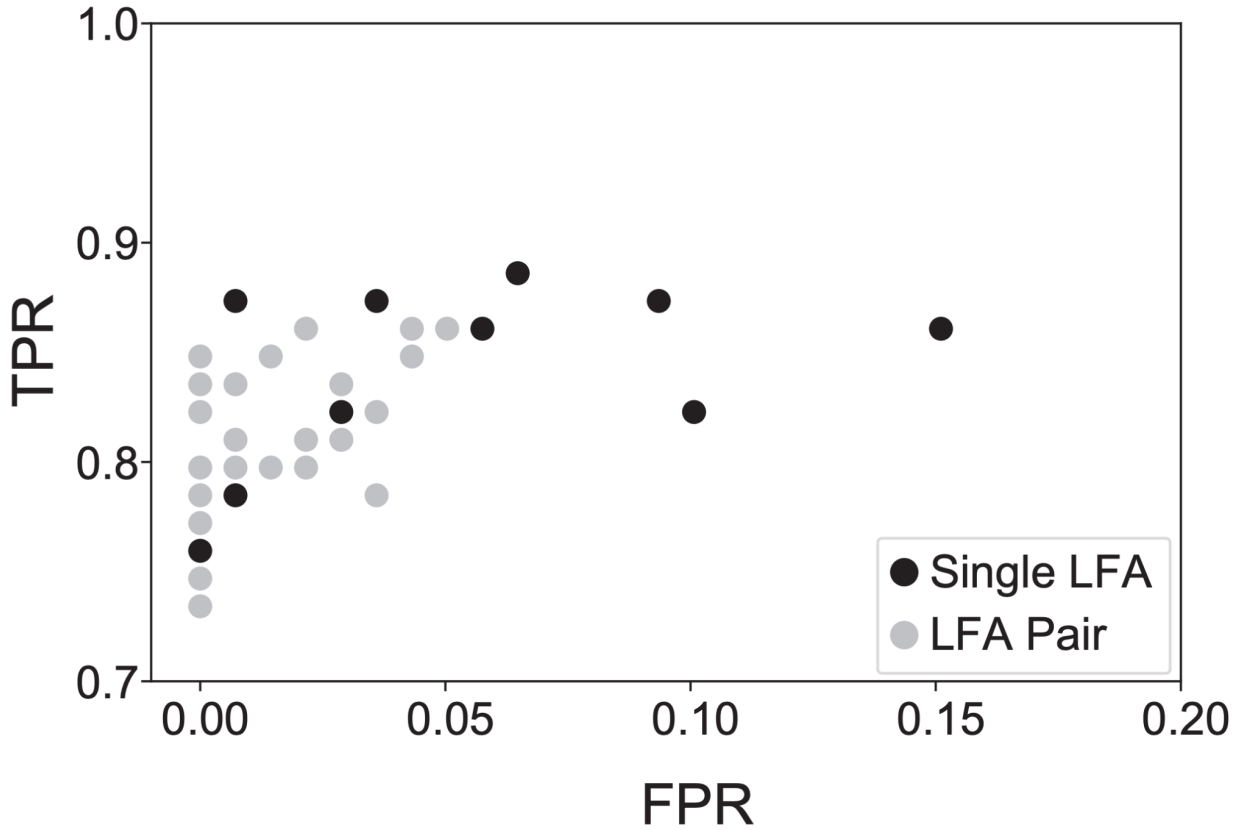
Figure S3.1: LFA performance.
Plotting LFA performance with respect to True (TPR) and False Positive Rates (FPR) after integrating IgM and IgG test results for each "Single LFA" (n = 10, black). Subsequently, an AND logic was applied to require concordant positivity for each "LFA Pair" (n = 45, grey) in order to classify a specimen as positive.

Figure S3.2: Pairwise LFA performance for XGBoost classifier.
Plotted are results at significance level α = 0.03 (A) and α = 0.045 (B). The diagonal (black outline) specifies results for single LFAs, whereas off-diagonal results reflect TPR of LFA combinations. The reported TPRs were averaged over 100 different random splits of data into 50% training and 50% test sets (see Supplemental Methods).
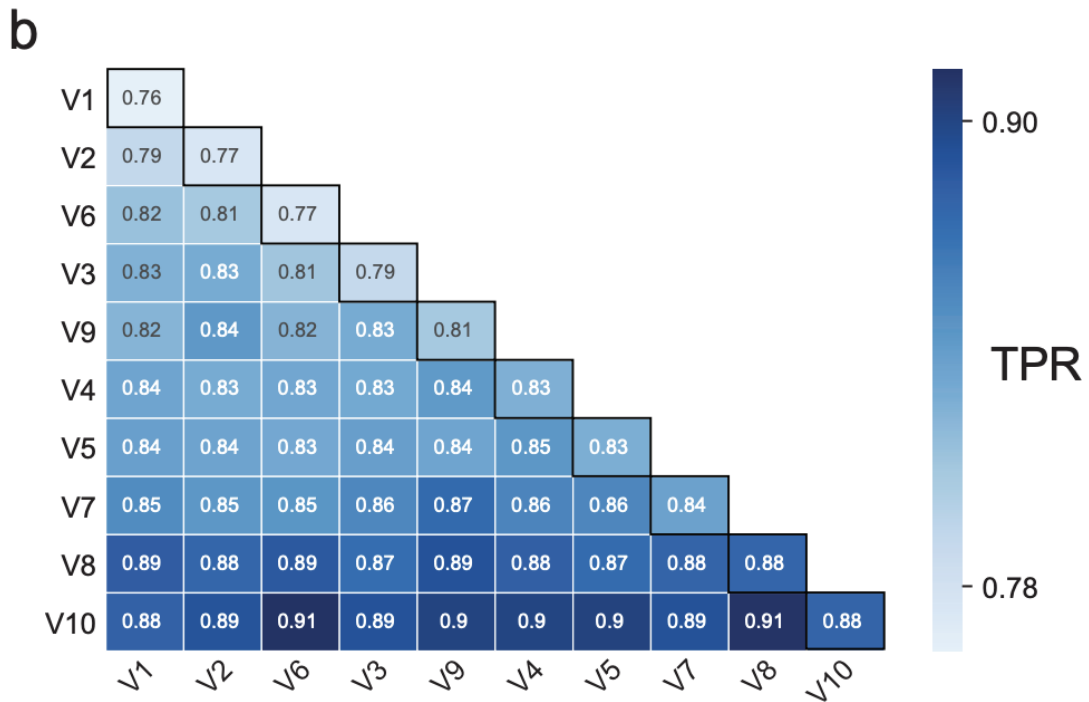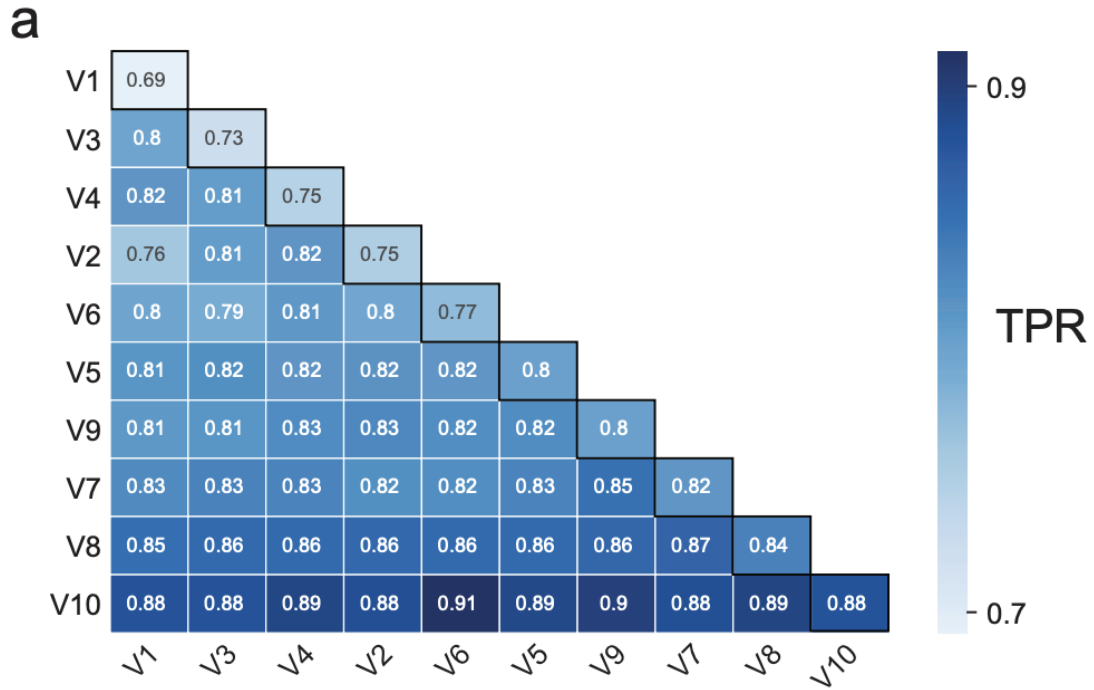
3.7: References

1. E. R. Adams, M. Ainsworth, R. Anand, M. I. Andersson, K. Auckland, J. K. Baillie, E. Barnes, S. Beer, J. Bell, T. Berry, S. Bibi, M. Carroll, S. Chinnakannan, E. Clutterbuck, R. J. Cornall, D. W. Crook, T. D. Silva, W. Dejnirattisai, K. E. Dingle, C. Dold, A. Espinosa, D. W. Eyre, H. Farmer, M. F. Mendoza, D. Georgiou, S. J. Hoosdally, A. Hunter, K. Jeffrey, P. Klenerman, J. Knight, C. Knowles, A. J. Kwok, U. Leuschner, R. Levin, C. Liu, C. Lopez-Camacho, J. C. M. Garrido, P. C. Matthews, H. McGivern, A. J. Mentzer, J. Milton, J. Mongkolsapaya, S. C. Moore, M. S. Oliveira, F. Pereira, E. P. Lopez, T. Peto, R. J. Ploeg, A. Pollard, T. Prince, D. J. Roberts, J. K. Rudkin, V. Sanchez, G. R. Screaton, M. G. Semple, D. T. Skelly, J. SlonCampos, E. N. Smith, A. J. S. Diaz, J. Staves, D. Stuart, P. Supasa, T. Surik, H. Thraves, P. Tsang, L. Turtle, A. S. Walker, B. Wang, C. Washington, N. Watkins, and J. Whitehouse. Antibody testing for COVID-19: A report from the National COVID Scientific Advisory Panel. medRxiv, page 2020.04.15.20066407, May 2020.

2. A. Chandrashekar, J. Liu, A. J. Martinot, K. McMahan, N. B. Mercado, L. Peter, L. H. Tostanoski, J. Yu, Z. Maliga, M. Nekorchuk, K. Busman-Sahay, M. Terry, L. M. Wrijil, S. Ducat, D. R. Martinez, C. Atyeo, S. Fischinger, J. S. Burke, M. D. Slein, L. Pessaint, A. V. Ry, J. Greenhouse, T. Taylor, K. Blade, A. Cook, B. Finneyfrock, R. Brown, E. Teow, J. Velasco, R. Zahn, F. Wegmann, P. Abbink, E. A. Bondzie, G. Dagotto, M. S. Gebre, X. He, C. Jacob-Dolan, N. Kordana, Z. Li, M. A. Lifton, S. H. Mahrokhian, L. F. Maxfield, R. Nityanandam, J. P. Nkolola, A. G. Schmidt, A. D. Miller, R. S. Baric, G. Alter, P. K. Sorger, J. D. Estes, H. Andersen, M. G. Lewis, and D. H. Barouch. SARS-CoV-2 infection protects against rechallenge in rhesus macaques. Science, May 2020.

3. T. Chen and C. Guestrin. XGBoost: A Scalable Tree Boosting System. In Proceedings of the 22nd ACM SIGKDD International Conference on Knowledge Discovery and Data Mining, pages 785–794, San Francisco California USA, Aug. 2016. ACM.

4. K. Duan, B. Liu, C. Li, H. Zhang, T. Yu, J. Qu, M. Zhou, L. Chen, S. Meng, Y. Hu, C. Peng, M. Yuan, J. Huang, Z. Wang, J. Yu, X. Gao, D. Wang, X. Yu, L. Li, J. Zhang, X. Wu, B. Li, Y. Xu, W. Chen, Y. Peng, Y. Hu, L. Lin, X. Liu, S. Huang, Z. Zhou, L. Zhang, Y. Wang, Z. Zhang, K. Deng, Z. Xia, Q. Gong, W. Zhang, X. Zheng, Y. Liu, H. Yang, D. Zhou, D. Yu, J. Hou, Z. Shi, S. Chen, Z. Chen, X. Zhang, and X. Yang. Effectiveness of convalescent plasma therapy in severe COVID-19 patients. Proceedings of the National Academy of Sciences, 117(17):9490–9496, Apr. 2020.

5. Johns Hopkins Coronavirus Resource Center. COVID-19 Map.

6. R. Lassauni`ere, A. Frische, Z. B. Harboe, A. C. Nielsen, A. Fomsgaard, K. A. Krogfelt, and C. S. Jørgensen. Evaluation of nine commercial SARS-CoV-2 immunoassays. medRxiv, page 2020.04.09.20056325, Apr. 2020.

7. Q.-X. Long, B.-Z. Liu, H.-J. Deng, G.-C. Wu, K. Deng, Y.-K. Chen, P. Liao, J.-F. Qiu, Y. Lin, X.-F. Cai, D.-Q. Wang, Y. Hu, J.-H. Ren, N. Tang, Y.-Y. Xu, L.-H. Yu, Z. Mo, F. Gong, X.-L. Zhang, W.-G. Tian, L. Hu, X.-X. Zhang, J.-L. Xiang, H.-X. Du, H.-W. Liu, C.-H. Lang, X.-H. Luo, S.-B. Wu, X.-P. Cui, Z. Zhou, M.-M. Zhu, J. Wang, C.-J. Xue, X.-F. Li, L. Wang, Z.-J. Li, K. Wang, C.-C. Niu, Q.-J. Yang, X.-J. Tang, Y. Zhang, X.-M. Liu, J.-J. Li, D.-C. Zhang, F. Zhang, P. Liu, J. Yuan, Q. Li, J.-L. Hu, J. Chen, and A.-L. Huang. Antibody responses to SARS-CoV-2 in patients with COVID-19. Nature Medicine, pages 1–4, Apr. 2020.

8. National Center for HIV/AIDS, Viral Hepatitis, and TB Prevention (U.S.). Division of HIV/AIDS Prevention. ; Association of Public Health Laboratories. Laboratory testing for the diagnosis of HIV infection : Updated Recommendations, June 2014.

9. D. Ng, G. Goldgof, B. Shy, A. Levine, J. Balcerek, S. P. Bapat, J. Prostko, M. Rodgers, K. Coller, S. Pearce, S. Franz, L. Du, M. Stone, S. Pillai, A. Sotomayor-Gonzalez, V. Servellita, C. S.-S. Martin, A. Granados, D. R. Glasner, L. M. Han, K. Truong, N. Akagi, D. N. Nguyen, N. Neumann, D. Qazi, E. Hsu, W. Gu, Y. A. Santos, B. Custer, V. Green, P. Williamson, N. K. Hills, C. M. Lu, J. D. Whitman, S. Stramer, C. Wang, K. Reyes, J. Hakim, K. Sujishi, F.

Alazzeh, L. Pharm, C.-Y. Oon, S. Miller, T. Kurtz, J. Hackett, G. Simmons, M. P. Busch, and C. Y. Chiu. SARS-CoV-2 seroprevalence and neutralizing activity in donor and patient blood from the San Francisco Bay Area. medRxiv, page 2020.05.19.20107482, May 2020.

10. W. H. Organization. "Immunity passports" in the context of COVID-19, Apr. 2020

11. F. Pedregosa, G. Varoquaux, A. Gramfort, V. Michel, B. Thirion, O. Grisel, M. Blondel, P. Prettenhofer, R. Weiss, V. Dubourg, J. Vanderplas, A. Passos, D. Cournapeau, M. Brucher, M. Perrot, and E. Duchesnay. Scikit-learn: Machine Learning in Python. Journal of Machine Learning Research, 12(85):2825–2830, 2011.

12. O. Troyanskaya, M. Cantor, G. Sherlock, P. Brown, T. Hastie, R. Tibshirani, D. Botstein, and R. B. Altman. Missing value estimation methods for DNA microarrays. Bioinformatics, 17(6):520–525, June 2001.

13. S. K. Vashist. In Vitro Diagnostic Assays for COVID-19: Recent Advances and Emerging Trends. Diagnostics, 10(4):202, Apr. 2020.

14. M. C. Weinstein, K. A. Freedberg, E. P. Hyle, and A. D. Paltiel. Waiting for Certainty on Covid-19 Antibody Tests — At What Cost? New England Journal of Medicine, 0(0):null, June 2020.

15. J. D. Whitman, C. A. Bulman, E. L. Gunderson, A. M. Irish, R. L. Townsend, S. L. Stramer, J. A. Sakanari, and C. Bern. Chagas Disease Serological Test Performance in U.S. Blood Donor Specimens. Journal of Clinical Microbiology, 57(12), Dec. 2019.

16. J. D. Whitman, J. Hiatt, C. T. Mowery, B. R. Shy, R. Yu, T. N. Yamamoto, U. Rathore, G. M. Goldgof, C. Whitty, J. M. Woo, A. E. Gallman, T. E. Miller, A. G. Levine, D. N. Nguyen, S. P. Bapat, J. Balcerek, S. Bylsma, A. M. Lyons, S. Li, A. W.-y. Wong, E. M. Gillis-Buck, Z. B. Steinhart, Y. Lee, R. Apathy, M. J. Lipke, J. A. Smith, T. Zheng, I. C. Boothby, E. Isaza, J. Chan, D. D. Acenas, J. Lee, T. A. Macrae, T. S. Kyaw, D. Wu, D. L. Ng, W. Gu, V. A. York, H. A. Eskandarian, P. C. Callaway, L. Warrier, M. E. Moreno, J. Levan, L. Torres, L. Farrington, R. Loudermilk, K. Koshal, K. C. Zorn, W. F. Garcia-Beltran, D. Yang, M. G. Astudillo, B. E. Bernstein, J. A. Gelfand, E. T. Ryan, R. C. Charles, A. J. Iafrate, J. K. Lennerz, S. Miller, C.

Y. Chiu, S. L. Stramer, M. R. Wilson, A. Manglik, C. J. Ye, N. J. Krogan, M. S. Anderson, J. G. Cyster, J. D. Ernst, A. H. B. Wu, K. L. Lynch, C. Bern, P. D. Hsu, and A. Marson. Test performance evaluation of SARS-CoV-2 serological assays. medRxiv, page 2020.04.25.20074856, May 2020.

Chapter 4: Systematic decoding of *cis* gene regulation defines context-dependent control of the multi-gene costimulatory receptor locus in human T cells.

This Chapter is under review as:

Cody T. Mowery, Jacob W. Freimer, Zeyu Chen, Salvador Casaní-Galdón, Christian M. Garrido, Benjamin G. Gowen, Vinh Nguyen, Dimitre R. Simeonov, Gemma L. Curie, Jennifer M. Umhoefer, Ralf Schmidt, Zachary Steinhart, Maya M. Arce, Jacob E. Corn, Bradley E Bernstein, Chun Jimmie Ye & Alexander Marson. Systematic decoding of *cis* gene regulation defines context-dependent control of the multi-gene costimulatory receptor locus in human T cells.

4.1: Abstract

Cis-regulatory elements (CRE) interact with *trans* regulators to orchestrate gene expression, but how this transcriptional regulation is coordinated in multi-gene loci has not been experimentally defined. We sought to characterize the CREs that control dynamic expression of adjacent T cell costimulatory genes *CD28*, *CTLA4*, and *ICOS* encoding regulators of cell-mediated immunity. Tiling CRISPR interference (CRISPRi) screens in primary human T cells – both Conventional and Regulatory subsets – allowed us to uncover gene-, cell subset-, and stimulation-specific CREs. Integrating these data with CRISPR knockout (KO) screens and ATAC-seq characterization identified *trans* regulators influencing chromatin states at specific CRISPRi-responsive elements to control costimulatory gene expression. Lastly, we discovered and extensively validated a critical CTCF boundary that governs the costimulatory locus, serving to reinforce CRE interaction with *CTLA4* while also preventing promiscuous activation of *CD28*. By systematically mapping CREs and associated *trans* regulators directly in primary human T cell subsets, this work overcomes longstanding experimental limitations to decode context-dependent gene regulatory programs in a complex, multi-gene locus critical to immune homeostasis.

4.2: Main

Interactions of *cis*-regulatory elements (CREs) and *trans* regulators control how genes are expressed in specific cell types and in response to specific extracellular stimuli[1,2]. Context-restricted transcription factors (TFs) work in concert with chromatin modifying complexes to bind CREs and tune the expression of target transcriptional programs[3–6]. However, how CREs and *trans* regulators coordinate to control gene expression in complex multi-gene loci harboring one or more functionally-related genes remains unknown[7]. While adjacent genes are commonly transcriptionally co-expressed[8–11], many loci harbor multiple genes that exhibit divergent expression patterns. By organizing the genome into topologically-associating domains (TADs)

and subTADs, regulators of chromatin structure such as CTCF play a critical role orchestrating transcriptional regulation by promoting interactions between CREs and promoters of their target genes[12–15] while insulating non-target loci from promiscuous activation[16–20]. Natural genetic variation in CREs can disrupt transcriptional regulation and confer risk for disease[21], providing strong motivation to functionally decode CREs and *trans* regulators directly in disease-relevant primary human cell types.

We sought to map systematically the *cis*-regulatory elements required for appropriate expression of three critical immune genes: *CD28*, *CTLA4*, and *ICOS*. Collectively referred to here as the "costimulatory genes," this CD28 family of receptors is believed to have arisen from ancestral duplications of *CD28* and is encoded by directly adjacent genes on human chromosome 2q33.2[22,23]. Since the ancestral duplications, each gene has functionally diverged[24] and evolved distinct expression dynamics[25]. These receptors influence the functional outcome of T cell activation and thus regulate immune homeostasis more broadly[26]. CD28 is constitutively expressed, and its engagement sends a co-stimulatory signal to drive cell activation in coordination with T cell receptor (TCR) signaling. Conversely, CTLA4 negatively regulates T cell costimulation via competitive, high-affinity interactions for the same ligands as CD28[27]. Regulatory T (T_{reg}) cells constitutively express CTLA4 at high levels and further upregulate it upon activation, whereas Conventional T (T_{conv}) cells exclusively express CTLA4 after activation. ICOS expression is induced in multiple activated T cell subsets and provides an orthogonal co-stimulatory signal that influences T cell polarization and T_{reg} function upon binding of a unique ligand, ICOSL[28,29]. The integration of these co-stimulatory and co-inhibitory signals shapes the functional outcomes of TCR engagement, ranging from anergy to full activation. The association of common genetic variants in this locus with various autoimmune conditions[30,31], and the clinical efficacy of costimulation-modifying therapies for cancer[32,33] and autoimmunity[34,35], together underscore the major immunological significance of this gene family and motivate deeper understanding of how costimulation is regulated. More broadly, systematic characterization of *cis*

gene regulation in this locus could reveal how regulatory logic functions in other ancestrally-duplicated genomic regions.

The transcriptional programs regulating the CD28 family of costimulatory genes have not been functionally characterized. In recent years, chromatin immunoprecipitation (ChIP-seq) and Assay for Transposase-Accessible Chromatin sequencing (ATAC-seq) have been widely used to map cell type- and context-restricted CREs and transcription factor binding[36] based on characteristic chromatin features, but these methods do not confirm functionality nor do they link CREs to their specific target genes. Consequently, it has been difficult to pinpoint and characterize the causal variant(s) in human 2q33.2 that alter costimulatory gene expression[37–39] and confer autoimmune disease risk[40–42]. Recently, high-throughput forward genetic screens using CRISPR modalities have been used to functionally link perturbed *trans* regulatory factors and their gene targets[43–51]. Moreover, our group previously deployed CRISPR Activation (CRISPRa) in an immortalized human T cell line to map CREs that regulate immune gene expression[52]. While CRISPRa can systematically identify CREs whose *de novo* activation is sufficient to induce target gene expression, CRISPR Interference (CRISPRi) is uniquely suited to determining the essentiality of CREs for target gene expression and defining the specific cellular contexts in which particular CREs function[53]. Past studies have successfully applied this approach in cancer cell lines[54–56], but limitations in lentiviral transduction have long precluded the application of CRISPRa and CRISPRi at scale in primary human T cells, until recently[46]. Using these CRISPR-based tools to dissect how *CD28*, *CTLA4*, and *ICOS* are dynamically regulated in primary human T cells could uncover insights into molecular mechanisms of immune activation and tolerance. Moreover, this genomic approach could simultaneously reveal how regulatory logic has evolved more broadly to tightly orchestrate ancestrally duplicated genes in a complex, multi-gene region.

Here, we report the first tiling CRISPRi non-coding screens in primary human T cell subpopulations, tiling sgRNAs across a 1.44 Mb TAD in human chr2q33.2 to discover CREs with gene-, context-, and cell type-restricted activity. By assessing how each non-coding perturbation

affects the expression of each T cell costimulatory gene in both T_{reg} and T_{conv} cells, we overcame the limitations of genomic methods like ChIP- and ATAC-seq to functionally link CREs and their gene target(s) in this complex, multi-gene locus. Complementary pooled CRISPR knockout screens identified *trans* regulators of CD28, CTLA4, and ICOS protein expression. ATAC-seq profiling of knockout T cells allowed us to discover specific *trans* regulators modifying the chromatin state of CREs in the target locus. These functional genomic studies also uncovered crosstalk between the regulation of adjacent genes and a critical role for CTCF in establishing genomic boundaries to coordinate the activity of multiple CREs in the locus. By functionally linking CREs and *trans* regulators, associating them with their gene targets, and uncovering how the locus is regulated by CTCF boundary elements, our integrative functional genomics approach systematically decoded the regulatory logic of a complex, disease-associated multi-gene locus.

4.3: Results

An efficient CRISPRi platform to map functional CREs in primary human T cell subsets

We set out to discover systematically the CREs that regulate *CD28*, *CTLA4*, and *ICOS* expression in primary human CD4$^+$ T cells. Expression of these genes varies between pro-inflammatory T_{conv} and anti-inflammatory T_{reg} cell populations, as well as under different stimulation conditions for each cell type (Figure S4.1A). We leveraged recent improvements in lentiviral production and delivery to primary human T cells[46] to establish a robust CRISPRi-based workflow for mapping CREs in both T_{conv} and T_{reg} cells (Figure 4.1A). An annotated TAD in human 2q33.2 harbors the three genes of interest (Figure 4.1B, black outline)[57] and contains numerous H3K27 acetylation peaks (Figure 4.1C) suggestive of active enhancer elements. To map the functional enhancers required for appropriate expression of each costimulatory gene, we generated a 11534 single guide RNA (sgRNA) library tiling across the region. We employed the

dCas9-ZIM3 CRISPRi system based on its improved performance over the original dCas9-KRAB system in primary human CD4$^+$ T cells (Figure S4.1B), consistent with reports in other cell types[58].

We performed CRISPRi tiling screens in primary human T$_{conv}$ and T$_{reg}$ cells to identify stimulus-responsive and cell type-specific CREs that control CD28, CTLA4, and ICOS expression. We isolated donor-matched primary T$_{conv}$ and T$_{reg}$ cells, lentivirally transduced dCas9-ZIM3 and the sgRNA library, and collected samples at the time of peak expression for each gene without or with re-stimulation (Figure S4.1A). By comparing sgRNA abundances in cells with low and high target protein expression isolated by fluorescence-activated cell sorting (FACS) (Figure 4.1D, right; Figure S4.1C-D), we identified CRISPRi responsive elements (CiREs) as candidate CREs controlling target gene expression in each cell type (Figure 4.1D). We observed high donor correlation for sgRNAs significantly associated with positive (R=0.76, p=1.2x10^{-9}) and negative (R=0.69, p < 2.2x10^{-16}) CRISPRi effects on candidate regulatory elements (Figure S4.1E). Despite CRISPRi targeting across the entire published TAD, most CiREs were concentrated in the individual gene bodies and *CD28-CTLA4-ICOS* intergenic region residing within a high contact frequency subdomain (Figure 4.1B, dashed). Within this region, CRISPRi signals were generally strongest near each transcriptional start site (TSS) (Figure S4.1F) and throughout the first introns of target genes, consistent with expected distributions of regulatory elements[59]. We identified additional CiREs both down- (Figure S4.2A) and upstream (Figure 4.2A,C, S2B) of each gene. These data demonstrate, for the first time, that large-scale CRISPRi tiling screens can be performed in primary human T$_{conv}$ and T$_{reg}$ cell subpopulations to associate non-coding DNA elements directly with their *cis* gene targets.

Tiling CRISPRi screens associate context-specific CiREs and their gene targets

We focused on the regions harboring the majority of CiREs to identify cell type-specific and context-restricted effects. In contrast to CD28 and ICOS, expression of CTLA4 is known to be markedly more context-dependent. Thus, we sought to identify CREs responsible for

stimulation-dependent CTLA4 upregulation in both T_{conv} and T_{reg} cells, as well as those underlying constitutive CTLA4 expression specifically in T_{reg} cells. We examined the annotated "*CTLA4 Regulatory Region*" harboring the majority of CRISPRi-responsive elements influencing CTLA4 expression (Figure 4.1D). Outside of the gene body, restimulated T_{conv} cell expression of CTLA4 was most sensitive to CRISPRi targeting at a candidate enhancer element ~40kb upstream of the *CTLA4* TSS (labeled "Stim-Responsive"), with a few other intervening regions exhibiting smaller regulatory effects (Figure 4.2A-B). Regulatory T cells assayed under the same conditions were partially sensitive to this Stim-Responsive CiRE but displayed greater reliance on another candidate enhancer 5 kb downstream (labeled "T_{reg}-Dominant") (Figure 4.2C-D). Interestingly, constitutive CTLA4 expression in resting T_{reg} cells was unresponsive to the Stim-Responsive element but exquisitely sensitive to this T_{reg}-Dominant CiRE, demonstrating the existence of neighboring enhancer elements that underlie cell- and context-restricted expression of CTLA4. Comparatively, CD28 and ICOS CRISPRi sensitivities varied little between T_{conv} and T_{reg} cells (Figure S4.2A-B). Of note, we discovered that *ICOS* expression was subtly sensitive to the Stim-Responsive and T_{reg}-Dominant CiREs in a cell type-specific manner despite the intervening *CTLA4* gene body (Figure S4.2C). This finding suggests that "nearest gene" assumptions of enhancer-promoter association fail to capture the full breadth of *cis* regulation of gene expression[56]. Importantly, although the region upstream of *CTLA4* is a published T_{reg} super-enhancer[41] (Figure 4.2C, bottom), we found that much of this region was insensitive to CRISPRi under the conditions assayed. Thus, the context-dependent functional effects we measured throughout this region could not be readily inferred based on H3K27ac ChIP-seq and ATAC-seq alone. We demonstrate that CRISPRi screening can uniquely identify complex, context-restricted CREs that regulate the expression of target genes of interest in specific cell types and activation contexts.

We next explored how this functional map of CiRE elements controlling *CTLA4* expression could help prioritize human genetic variants conferring risk to T cell-mediated autoimmune

conditions like rheumatoid arthritis[60,61]. The biological relevance of CTLA4 regulation in rheumatoid arthritis is further underscored by clinical efficacy of CTLA4-Ig for this disease[62]. We annotated CiREs across the *CTLA4* locus by analyzing data from neighboring sgRNAs (Figure S4.2D-E, see Methods). Interestingly, the known *CTLA4* eQTL and index SNP most strongly associated with rheumatoid arthritis risk, rs3087243 (Figure 4.2E-F, triangle), resides outside of these CiRE regions. In contrast, different variants were found in one or both of the "Stim-Responsive" and "T_{reg}-Dominant" CiREs 30-40kb away from the *CTLA4* TSS. Both rs12990970 in the T_{reg}-Dominant CiRE and rs13030124 in the Stim-Responsive CiRE are in LD with rs3087243 (R^2=0.7416 & 0.7316, respectively) and are themselves significantly associated with rheumatoid arthritis risk (Figure 4.2E) and *CTLA4* expression (Figure 4.2F). Additionally, one variant in LD with rs3087243 (rs11571316, R^2=0.951) is harbored within a CiRE embedded in the *CTLA4* promoter region and T_{reg} super-enhancer. Thus, we show that CRISPRi functional screening can prioritize candidate causal variants within a haplotype that may not be identifiable from human genetic and chromatin-mapping data alone.

CRISPR KO screens with ATAC-seq validation localize *trans* regulatory effects to CiREs

A longstanding challenge has been to identify specific *trans* regulators controlling a given CRE. In order to first characterize the transcriptional regulatory control of *CD28*, *CTLA4*, and *ICOS* in T_{conv} cells more thoroughly, we performed CRISPR knockout (KO) screens to examine CD28 and ICOS regulation in resting and restimulated primary human T_{conv} cells, respectively (Figure S4.3A). Integrating these data with published results for CTLA4[47], we identified factors significantly regulating (Adjusted P-value < 0.05) individual, pairs of, or all three costimulatory genes (Figure S4.3B). Reassuringly, we noted concordant effects of genes acting in the same biological pathway, including critical transcription factors like IRF4 and RelA positively regulating stimulation-responsive CTLA4 and ICOS expression[63,64] (Figure S4.3B-C). Publicly available bulk RNA sequencing of cells with arrayed *trans* regulator KO served to validate the regulatory effects

revealed by the pooled CRISPR screens (Figure S4.3C)[47]. Taken together, these observations confirmed that our systematic CRISPR KO screens successfully identified *trans* regulators influencing costimulatory gene expression.

We next aimed to link *trans* regulators with the specific CiREs they influence. To this end, we assessed changes in Stim-Responsive CiRE accessibility by ATAC-seq following CRISPR KO of individual *trans* regulators[47] (Figure 4.3A-C). IRF4 is a stimulation-responsive transcription factor that critically regulates T cell function and survival[64]. We found that IRF4 directly bound the Stim-Responsive CiRE and promoted its chromatin accessibility in bulk human CD4$^+$ T cells (Figure 4.3B, D), consistent with the transcription factor's well-characterized immunological role and positive effect on CTLA4 expression (Figure S4.3B,C). The study also suggested more novel regulators. Notably, ZNF217 negatively influences all three costimulatory genes (Figure S4.3B-D), and ATAC-seq profiling revealed that ZNF217 KO increased accessibility at the Stim-Responsive CiRE (Figure 4.3B, D). This suggests that this factor exerts a negative effect on *CTLA4* expression in T$_{conv}$ cells by normally repressing this enhancer element. ZNF217 has been studied in the context of cancer[65] and is known to associate with various protein complexes to either promote or inhibit target gene expression[66], but its regulatory effects on immune-related genes have not been thoroughly characterized[47]. Here, we found that ZNF217 KO increased accessibility at many other putative CREs in the costimulatory locus (Figure S4.4A-B, S5A). Interestingly, ZNF217 also regulated the expression of a number of *trans* factors acting on the costimulatory genes, including *IRF4* (Figure S4.5B). These findings indicate a regulatory circuit whereby ZNF217 inhibits *CTLA4* at least in part through its effects on *IRF4* (Figure 4.3E). More broadly, ZNF217 KO resulted in immune transcriptional program dysregulation as well (Figure S4.5C). Thus, we demonstrate that integrative CRISPR screens and genomic analyses robustly characterize complex gene regulatory relationships influencing costimulatory gene expression by systematically mapping functional non-coding regulatory elements influencing target genes,

identifying *trans* regulators influencing those same genes, and leveraging perturbational ATAC-Seq to associate *trans* and *cis* effects.

CRISPR tiling and KO screens revealed regulatory crosstalk of *CD28*, *CTLA4*, and *ICOS*

The sensitivity of all three costimulatory genes to shared *trans* regulators like ZNF217 led us to explore other mechanisms of coordinated regulation acting in the locus. To our surprise, we observed that CRISPRi targeted to each TSS positively influenced the expression of the adjacent costimulatory gene(s) (Figure 4.4A). CRISPRi tiling across the *CD28* transcriptional start site decreased *CD28* expression as expected, but also increased *CTLA4* in T_{conv} cells and had no effect on *ICOS*. Similarly, targeting the *ICOS* TSS subtly enhanced *CTLA4* expression in T_{conv} cells, though *CD28* remained unchanged. Lastly, CRISPRi-mediated inhibition of the *CTLA4* TSS positively affected the expression of both adjacent genes. CRISPRi targeting at the *CTLA4* TSS with multiple individual sgRNAs confirmed positive effects on *CD28* and *ICOS* expression relative to non-targeting controls (Figure 4.4B, left). This effect on neighboring genes was not due to loss of the CTLA4 gene product, as CRISPR knockout of *CTLA4* had negligible effects on CD28 and ICOS expression (Figure 4.4B, right). Importantly, we did not find evidence of promoter homology between adjacent genes, which suggests these effects are not simply due to promiscuous off-target sgRNA binding to homologous sequences. Of note, we found that adjacent (*CD28-CTLA4* and *CTLA4-ICOS*) but not non-adjacent (*CD28-ICOS*) gene pairs are subject to significant co-regulation by shared *trans* regulators (Figure S4.6). Thus, we discovered that shared sets of *trans* regulators coordinately influence adjacent costimulatory gene expression while the neighboring genes themselves interact in *cis*. In addition to the sharing of Stim-Responsive and T_{reg}-Dominant CiRE sensitivity by CTLA4 and ICOS (Figure S4.2C), these findings establish additional regulatory interplay between adjacent costimulatory genes. Moreover, our data reveal an underexplored level of complexity in human gene regulation, providing evidence of complex modes of *cis* and *trans* crosstalk shaping the expression of individual genes in a multi-gene locus.

CRISPRi-sensitive CTCF boundaries direct preferential enhancer-promoter looping

Evidence of crosstalk between neighboring genes raised the question of how *cis*-regulatory elements are ultimately linked specifically to their target genes. Given CTCF's role in functionally compartmentalizing the linear genome by establishing TADs and subTADs[15], we explored how CTCF and three-dimensional chromatin organization might regulate costimulatory gene expression. We examined CTCF ChIA-PET data[67] to determine how the human 2q33.2 locus is structurally organized in primary human CD4^{+} T cells. Chromatin Interaction Analysis with Paired-End-Tag sequencing (ChIA-PET) revealed chromatin looping between *CD28-CTLA4* and *CTLA4-ICOS,* but not between *CD28-ICOS* promoters and gene bodies (Figure 4.5A), consistent with the selective regulatory crosstalk between adjacent genes we observed. This suggests that CTCF binding might establish locus architecture that permits adjacent, but not non-adjacent, gene interactions.

Next, we aligned the ChIA-PET data with functional CiRE maps from our CRISPRi experiments. The "peaks" of CTCF-mediated 3D genomic contacts co-localized with three CiREs exhibiting small yet discordant effects on adjacent genes (Figure 4.5A, dashed outlines). These CTCF-associated CiREs reside in accessible chromatin (Figure 4.5A) marked by H3K4me1 and minimal H3K4me3 but not H3K27ac (Figure S4.7A), consistent with the epigenomic profile of poised enhancer elements. Motif mapping at the dominant peak labeled "CTCF-2" revealed a cluster of CTCF binding sites with one dominant antisense motif (M1+M2) in a highly conserved region surrounded by several weaker and evolutionarily non-conserved motifs (Figure S4.7B). This motif cluster is flanked by Alu SINE and LINE-2 retrotransposable elements, which are postulated to be involved in the evolution of transcriptional regulation via species-specific CTCF insulator expansion[68]. Arrayed validation of CRISPRi targeting this region recapitulated the gene expression changes observed in the pooled tiling screens (Figure S4.7C), further supporting that

the CTCF-2 boundary might serve a critical role governing genomic topography in the costimulatory locus.

The CTCF-2 boundary region lies between *CD28* and *CTLA4*, which encode activating and inhibitory costimulatory receptors, respectively. We next tested whether this CTCF site serves as a boundary to control *CD28* and *CTLA4* expression by modulating CRE activity in the locus. We used paired Cas9 RNPs to excise the CTCF-2 region (Figure S4.7B, bottom) or a control region near *AAVS1* in primary human T_{conv} cells. Then, we used CRISPRa to compare CD28 and CTLA4 induction between non-targeting control (NTC) sgRNAs and sgRNAs targeting the Stim-Responsive CiRE (Figure 4.5B). So long as the CTCF-2 boundary was intact, Stim-Responsive CiRE activation with CRISPRa only modestly altered CD28 (Figure 4.5C, "Intact Boundary") with more robust induction of CTLA4 (Figure 4.5D, "Intact Boundary"). However, in the setting of CTCF-2 boundary excision, CRISPRa targeting of the Stim-Responsive CiRE was less effective at inducing CTLA4 and concomitantly increased aberrant CD28 activation (Figure 4.5C-D, "ΔCTCF-2"). These data strongly suggest that the CTCF-2 boundary masks *CD28* from spurious activation, and that disruption of this critical boundary element effectively re-appropriates Stim-Responsive CiRE activity to *CD28*. Importantly, the study also uncovers an under-appreciated role of the CTCF boundary element in reinforcing proper *CTLA4* regulation by its stimulation-responsive enhancer.

We next sought to more finely characterize how the CTCF-2 boundary governs three-dimensional chromatin conformation in the costimulatory locus. To that end, we used CRISPRi to interfere with the CTCF-2 site which falls at a boundary separating two chromatin subdomains (Figure 4.5E). Then, we performed 4C-Seq in primary T_{conv} cells with or without CTCF-2 boundary perturbation (Figure 4.5E, S7D). Anchoring the 4C-seq assay on the Stim-Responsive CiRE, we found that CTCF-2 boundary perturbation permitted more frequent interactions between the non-coding element and *CD28* (Figure 4.5F, S7E) at the expense of contacts with *CTLA4* (Figure 4.5G, S7F). Interestingly, CTCF-2 excision also disrupted interactions with *ICOS* (Figure 4.5H,

S7G), which shares sensitivity to the Stim-Responsive CiRE with *CTLA4* (Figure S4.2C). Thus, by mapping the reorganized genomic topology after CTCF-2 perturbation using 4C-seq, we discovered a boundary domain that reinforces CRE prioritization of stimulation-responsive genes (*CTLA4, ICOS*), of which CTLA4 encodes an inhibitory costimulatory receptor, while simultaneously limiting effects on expression of a neighboring activating costimulatory receptor (CD28).

Overall, our tiling CRISPRi and *trans* KO screens revealed a critical regulatory role of CTCF boundary sites in establishing enhancer looping to preferential gene targets. More broadly, our data reaffirm that gene regulation in complex multi-gene loci is susceptible to neighborhood effects, and that higher-level genomic organization plays a critical role in restricting enhancer activity to *bona fide* targets. Taken together, we systematically mapped gene-, cell type-, and context-specific enhancer elements that regulate costimulatory gene expression under the coordination of *trans* regulators and CTCF boundary elements.

4.4: Discussion

Recent advances in deploying CRISPR technologies at scale in primary human T cells enabled us to develop an integrative functional genomics approach to discover, validate, and functionally disentangle *cis* and *trans* components of complex regulatory circuits key for immune homeostasis. Systematic perturbations of coding and non-coding sequences represent a considerable step beyond genomic profiling approaches like ChIP- and ATAC-seq, which have been instrumental in informing our current understanding of immune cell gene regulatory networks but fail to associate CREs with their gene target(s). Although the CiREs we mapped generally overlapped with chromatin profiles indicative of regulatory elements, only a subset of accessible chromatin regions was critical for target gene regulation as demonstrated by CRISPRi sensitivity. As a notable example, most of the well-characterized H3K27ac super-enhancer upstream of

CTLA4 in T$_{reg}$ cells appeared relatively unresponsive to CRISPRi in the specific stimulation contexts we tested. Although the possibility exists that our assay was not sufficiently sensitive to identify all CREs influencing target gene expression – especially if there is regulatory redundancy – we did uncover non-redundant CRISPRi-responsive sites within the broader super-enhancer that did not necessarily reflect the strongest ATAC-seq or H3K27ac ChIP signals. Many have called for experimental annotation of super-enhancer elements[69], and our functional validation of regulatory element activity reinforces the importance of experimentally annotating non-coding regions, particularly in complex loci of significant physiologic importance. Furthermore, CRISPRi revealed CREs shared by *CTLA4* and *ICOS* – an insight lost with common CRE inference from ChIP-seq and ATAC-seq. Future work can use our approach to understand how different CREs operate in specific contexts. The ability to locate critical non-coding sites and functionally connect them directly to target gene(s) in particular cellular contexts moves us beyond conclusions that can be reached with observational chromatin profiling and will transform our understanding of how CREs operate in complex genomic loci.

Common genetic variation influencing traits and complex disease risk overwhelmingly occurs at non-coding regions of the genome[70], which remain poorly functionally annotated. Systematic perturbations of disease-associated regions will thus be crucial to prioritize causal risk variants and functionally link them to target genes that depend on these elements. The lack of conservation of enhancer elements across species[71], which may be perturbed by these non-coding genetic variants, underscores the importance of performing functional experiments directly in human cells as opposed to model organisms. Numerous publications have associated the human polymorphism rs3087243 with altered *CTLA4* expression[37–39] and autoimmunity risk[30,31], but our screens pointed to other genetic variants in strong linkage disequilibrium with this lead SNP that may individually or cooperatively mediate the expression effects by altering the activity of validated CRISPRi Responsive Elements. Importantly, we performed the CRISPRi screens under select stimulation conditions chosen for maximum expression of each target gene, so other

context-specific enhancer elements could nominate different risk variants in other stimulation contexts. Nonetheless, while we focused primarily on rheumatoid arthritis, our dataset can be used to characterize additional genetic associations residing throughout the 2q33.2 locus, such as Graves' disease and Type I Diabetes[72,73]. We not only link new candidate variants to their target genes, but we also discover upstream transcription factors that regulate the chromatin state of the elements that harbor these genetic variants. Taken together, we use the power of functional genomics to decipher gene regulatory networks contributing to disease risk.

The gene products encoded in the *CD28/CTLA4/ICOS* locus tune a delicate costimulatory balance and are under tight regulation. Our perturbation data revealed complex and previously unappreciated circuits controlling expression levels of these receptors, including by ZNF217 and IRF4 acting on a *CTLA4*-associated enhancer element. Moreover, we demonstrate how systematic genomic studies like this one can characterize how local genomic architecture governs *cis*-regulatory element and *trans* regulator interactions to control expression of specific target genes, especially in complex loci where multiple key target genes neighbor critical enhancer elements. Our CRISPRi tiling data and functional 4C-Seq validation showed how CTCF boundaries prioritize enhancer activity to primary gene targets, and how boundary disruption gives rise to promiscuous gene regulation in the costimulatory locus. In a locus encoding a critical negative regulatory gene (*CTLA4*) flanked by two activating receptors, coordination of enhancer activity to the appropriate target at the appropriate time is of utmost importance: aberrant cellular activation leads to deleterious immune hyperreactivity, whereas activation blockade impedes immune defense from pathogenic threat. Topologically-associating domains (TADs) and subTADs function to this end, segregating the genome and organizing regulatory processes, but they do so incompletely[74]. Despite intervening CTCF boundary elements of varying strength, the CRISPRi screens identified gene crosstalk where adjacent costimulatory gene TSS's were mutually sensitive to one another. Consistent with previous studies attributing similar instances of gene crosstalk to shared enhancers[54,75], we identified Stim-Responsive enhancer sharing

between *CTLA4* and *ICOS* (Figure S4.2C), with *CD28* sensitivity to the same element blunted by the CTCF-2 boundary. The neighboring costimulatory genes also could be mutually sensitive due to transcriptional interference[76–82] or local competition for *trans* regulators shared by adjacent genes (Figure 4.5A), and additional experimentation will be needed to explore these possibilities. Nonetheless, our systematic investigation of GRNs expands on decades of genomic studies of the regulation of multi-gene loci, especially in model systems, and reveals reciprocal regulatory effects between adjacent genes in a locus of central importance for human immunology.

The *CD28/CTLA4/ICOS* locus is essential for immune regulation and human health. This is evidenced by strong genetic associations with immune dysregulation and the emergence of effective costimulatory modulation treatments for autoimmunity[34,35] and malignancies[83]. Here, we define coding and non-coding elements that shape the expression of these genes in human T cells. These studies serve as a roadmap for future efforts to define disease-associated functional gene regulatory networks in the relevant primary human cell types. Looking forward, knowledge of specific transcription factors, enhancers, and boundary elements that regulate target gene expression in varying immune cell contexts will enable design of complex synthetic circuits to program the expression of immune regulatory products in cellular immunotherapies.

Acknowledgements

Competing Interests

C.T.M. is a compensated Bio+Health Venture Fellow at Andreessen Horowitz. B.G.G. is a current employee of Spotlight Therapeutics. B.E.B. declares outside interests in Fulcrum Therapeutics, HiFiBio, Arsenal Biosciences, Design Pharmaceuticals, Cell Signaling Technologies, and Chroma Medicine. C.J.Y. is a Scientific Advisory Board member for and holds equity in Related Sciences and ImmunAI, a consultant for and holds equity in Maze Therapeutics, and is a consultant for TReX Bio. C.J.Y. has received research support from Chan Zuckerberg Initiative, Chan Zuckerberg Biohub, and Genentech. C.J.Y is a cofounder, member of the boards of directors, and member of the scientific advisory board of Survey Genomics. A.M. is a cofounder of Arsenal Biosciences, Spotlight Therapeutics and Survey Genomics; serves on the boards of directors at Spotlight Therapeutics and Survey Genomics; is board observer at Arsenal Biosciences; is a member of the scientific advisory boards of Arsenal Biosciences, Spotlight Therapeutics, Survey Genomics, NewLimit, and Amgen; owns stock in Arsenal Biosciences, Spotlight Therapeutics, NewLimit, Survey Genomics, and PACT Pharma; and has received fees from Arsenal

Biosciences, Spotlight Therapeutics, NewLimit, 23andMe, PACT Pharma, Juno Therapeutics, Trizell, Vertex, Merck, Amgen, Genentech, AlphaSights, Rupert Case Management, Bernstein and ALDA. A.M. is an investor in and informal advisor to Offline Ventures and a client of an informal advisor to EPIQ. The Marson laboratory has received research support from Juno Therapeutics, Epinomics, Sanofi, GlaxoSmithKline, Gilead and Anthem.

4.5: Methods

Isolation and culture of human T cells

Peripheral Blood Mononuclear Cell-enriched leukapheresis products (leukopaks) were sourced from healthy donors following informed and written consent (Stemcell Technologies). $CD4^+CD127^{low}CD25^+$ Regulatory T cells and $CD4^+CD25^-$ Conventional T cells were isolated from leukopaks using EasySep magnetic selection following the manufacturer's recommended protocol (Stemcell Technologies #18063). Regulatory T cell samples were further enriched for purity either before (validation) or after (screen) experimentation as indicated for each experiment below. Conventional T cells used in screens were frozen in Bambanker Cell Freezing Medium at 50e6 cells/ml (Bulldog Bio #BB01) and stored in liquid nitrogen immediately following isolation. Regulatory T cells used in screens, and all cells used in arrayed validations, were used immediately after isolation without freezing. Frozen cells were rapidly thawed in a 37°C water bath. All cells were cultured in Complete X-VIVO [cX-VIVO: X-VIVO 15 (Lonza Bioscience #04-418Q) supplemented with 5% FCS (R&D Systems, lot #M19187), 55uM 2-mercaptoethanol (Fisher Scientific #21985023), and 4mM N-Acetyl L-Cysteine (VWR #0108)]. Regulatory T cells were activated by CTS Dynabeads Treg Xpander (Thermo Fisher #46000D, 1:1 cell:bead ratio) and maintained at 1e6 cells/mL in cX-VIVO supplemented with recombinant human IL-2 (Amerisource Bergen #10101641) as indicated for each experiment below. Conventional T cell cultures were activated by CTS Dynabeads CD3/CD28 (Thermo Fisher #40203D, 1:1 cell:bead ratio) and maintained at 1e6 cells/mL in cX-VIVO supplemented with recombinant human IL-2 as

indicated for each experiment below. Bulk CD4^{+} T cells used in Figure S4.1B were isolated from a leukopak from a single human donor using EasySep magnetic selection following the manufacturer's recommended protocol (Stemcell Technologies #17952) and otherwise handled the same as Conventional T cells.

Trans regulator screens were conducted as previously described[47]. Primary human CD4^{+}CD25^{-} T cells were isolated using EasySep magnetic selection following the manufacturer's recommended protocol for isolating the responder fraction (Stemcell Technologies #18063). Cells were cultured at 1e6 cells/mL in Complete RPMI [cRPMI: RPMI (Sigma #R0883) supplemented with 10% FCS (R&D Systems lot #M19187), 100U/mL Pen-Strep (Fisher Scientific #15140122), 2mM L-Glutamine (Fisher Scientific #25030081), 10mM HEPES (Sigma #H0887), 1X MEM Non-essential Amino Acids (Fisher Scientific #11140050), 1mM Sodium Pyruvate (Fisher Scientific #11360070), and 50U/mL IL-2 (Amerisource Bergen #10101641)]. Cells were activated with Immunocult Human CD3/CD28/CD2 T Cell Activator (STEMCELL #10970) at 6.25uL per 1e6 cells and maintained at 1e6 cells/mL in cRPMI.

Lentivirus Production

High-titer lentivirus was generated as previously described[46]. Lenti-X HEK293T cells (Takara Bio #632180) were maintained in complete DMEM [cDMEM: GlutaMAX™ (Fisher Scientific #10566024) supplemented with 10% FCS (R&D Systems lot #M19187), 100U/ml Pen-Strep (Fisher Scientific #15140122), 1mM Sodium Pyruvate (Fisher Scientific #11360070), 1x MEM Non-Essential Amino Acids (Fisher Scientific #11140050) and 10mM HEPES solution (Sigma #H0887). Cells were kept at a confluency of <60%. Prior to transfection, Lenti-X cells were seeded in Complete Opti-MEM [cOpti-MEM: Opti-MEM Reduced Serum Medium with GlutaMAX™ Supplement (Gibco #31985088) supplemented with 5% FCS (R&D Systems, lot #M19187), 1mM Sodium Pyruvate (Fisher Scientific #11360070), 1x MEM Non-Essential Amino Acids (Fisher Scientific #11140050)] overnight to achieve confluency between 85% and 95% at the time of transfection. The day after plating, Lenti-X cells were transfected with desired plasmid,

2nd generation lentiviral packaging plasmid psPAX2, and transfer plasmid pMD2.G using Lipofectamine 3000 Transfection Reagent (Fisher Scientific #L3000075) following the manufacturer's recommended protocol. After 6 hours, the transfection medium was replaced with cOPTI-MEM supplemented with 1.15x ViralBoost (Alstem Bio #VB100). Lentiviral supernatants were harvested at 24 and 48 hours after transfection and spun at 500xG 5 minutes 4°C to remove packaging cell debris. The cleared supernatants were mixed with ⅓ volume Lenti-X-Concentrator (Takara Bio #631232), incubated 24-96 hours at 4°C, and then centrifuged at 1500xG, 45 minutes, 4°C to pellet lentiviral particles. Lentiviral pellets were resuspended with 1/100th (screens) or 1/10th (validations) volume cX-VIVO, aliquoted, and frozen at -80°C until use. Lentiviral aliquots were thawed in ambient air at room temperature and gently resuspended prior to use. Concentrated lentivirus was titered in a 2x dilution series to identify doses for dCas9-ZIM3 saturation and 50% transduction efficiency of sgRNA libraries.

Plasmids

CRISPRi single guide RNA (sgRNA) libraries were designed and cloned as previously described[52]. The hg38 coordinates of the region harboring *CD28, CTLA4,* and *ICOS* were chr2:202527032-203967032. Given the general conservation of TADs between different cell types[85] and due to the unavailability of HiC data in primary T cells at the time of sgRNA library design, this region was derived from a topologically-associating domain (extended by 20kb bilaterally) originally defined in GM12878 cells[57]. The TAD tiling library (11534 sgRNAs) contains every 20bp protospacer flanked by a 5'-NGG protospacer adjacent motif (PAM) within the defined region, excluding only sequences (1) containing BstXI or BlpI restriction sites used for cloning and/or (2) >1 perfectly matching site across the genome. Protospacers flanked by adaptor sequences were synthesized by Agilent Technologies and cloned into the pCRISPRia-v2 lentiviral vector (Addgene #84832) as previously described [86].

To generate the lentiviral vector delivering dCas9-ZIM3, we first amplified the ZIM3 KRAB domain conjugated to dCas9 from pLX303-ZIM3-KRAB-dCas9 (Addgene #154472) via PCR with primers 5'-GAGCTGTACAAGATTAACGGATCCGGCGCAACAAACTTCTCTCTGCTGAAACAA GCCGGAGATGTCGAAGAGAATCCTGGACCGATGAACAATTCCCAGGGAAGAGT and 5'-CTGATCAGCGGGTTTAAACACGTACTGCTAGAGATTTTCCAC. The lentiviral backbone Lenti-SFFV-mCherry-dCas9-VP64 [46] was digested with PmeI (NEB #R0560) and BamHI (NEB #R3136). The dCas9-ZIM3 insert was cloned into the linearized Lenti-SFFV-mCherry backbone using NEBuilder HiFi DNA Assembly Master Mix (NEB #E2621) following the manufacturer's recommended protocol.

For arrayed CRISPRi validation experiments, four or more sgRNA sequences targeting the feature of interest were ordered as Ultramers (IDT) with flanking sequences: 5'-AAGTATCCCTTGGAGAACCACCTTGTTGG-[sgRNA]-GTTTAAGAGCTAAGCTGGAAACAGCATAGCAAGTT. Non-targeting control sgRNAs were chosen at random from the Human CRISPR Inhibition Pooled Library (Dolcetto) (Addgene #1000000114). Diluted Ultramers (0.2uM) were cloned into BlpI- (NEB #R0585) BstXI-digested (NEB #R0113) pCRISPRia-v2 lentiviral vector (Addgene #84832) using NEBuilder HiFi DNA Assembly Master Mix (NEB #E2621) and transformed into STBL3 chemically-competent cells (QB3 MacroLab). Cultures were grown overnight in the presence of Ampicillin (Fisher Scientific #J66972-AC). Mini (Zymo Research #D4037) and/or maxi (Zymo Research #D4203) plasmid DNA preps were used for lentivirus production.

For arrayed CRISPRa experiments, sgRNAs were ordered as sense (5'-CACCG[sgRNA]) and antisense (5'-AAAC[sgRNA]C) oligonucleotides (IDT). 200pmol of sense and antisense oligos for each sgRNA were mixed in 1x CutSmart buffer (NEB), heated to 95°C and slowly cooled to 25°C for annealing. Annealed oligos were diluted 1/150, cloned into the pXPR_502 lentiviral vector (Addgene #96923) using BsmBI-v2 Golden Gate Assembly Kit (NEB #E1602L) as previously described [46], and transformed into STBL3 chemically-competent cells (QB3

MacroLab). Cultures were grown overnight in the presence of Ampicillin (Fisher Scientific #J66972-AC). Mini (Zymo Research #D4037) and/or maxi (Zymo Research #D4203) plasmid DNA preps were used for lentivirus production.

CRISPRi Screens

Primary human T cells from two donors were activated as described above. T_{conv} cells were activated and maintained in 300U/mL rhIL-2. T_{reg} cells were activated in 300U/mL rhIL-2 and subsequently maintained in 200U/ml rhIL-2. One day after activation, T cells were transduced with saturating doses (1.5-3.5% v/v) of concentrated dCas9-ZIM3 lentivirus. Two days after activation, T cells were transduced with 1% v/v (~50% transduction efficiency) sgRNA library virus for >100x cell:sgRNA coverage. Three days after activation, cell cultures were split to 1e6 cells/mL with fresh cX-VIVO supplemented with rhIL-2 and puromycin (2ug/mL final, Fisher Scientific #A1113803). Puromycin selection was confirmed by (1) untransduced T cell killing and (2) sgRNA-BFP enrichment relative to unselected T cell cultures as measured by flow cytometry (Thermo Fisher Attune). Cells were maintained ~1e6 cells/mL every 2 days with fresh cX-VIVO supplemented with rhIL-2. Eight days after activation, a fraction of T cells from each donor were restimulated for 24 hours with 1uL/mL Cell Activation Cocktail without Brefeldin A (Biolegend #423302) for ICOS staining. Eighteen hours later, a fraction of T cells from each donor were restimulated for 6 hours with 1ul/mL Cell Activation Cocktail without Brefeldin A for CTLA4 staining. At the end of the restimulation period, samples were harvested for fluorescence-activated cell sorting (FACS). Cells for ICOS (24 hours restimulation), CTLA4 (6 hours restimulation for both cell types and 0 hours restimulation for T_{reg} cells only), and CD28 (0 hours restimulation) were spun down at 500xG, 10 minutes, 4°C. After spinning, cells were washed in 50mL cold EasySep buffer (PBS, 2% FCS, 2mM EDTA), applied to a magnet for removing Dynabeads, and transferred to a new tube. All samples were stained for 30 minutes at 4°C with Ghost Dye Red 780 (Tonbo #13-0865), and antibodies for ICOS (Biolegend #313510) and CD28 (Biolegend #302912) were included in the appropriate samples. After surface staining, cells were

washed twice in cold EasySep buffer and fixed with the FOXP3 Fix/Perm Buffer Set (Biolegend #421403) at room temperature for 30 minutes. After fixation, cells were spun at 750xG, 10 minutes, 4°C. ICOS and CD28 samples were resuspended at 40e6 cells/mL in cold EasySep buffer and stored at 4°C until FACS. Samples for Total CTLA4 staining were washed and permeabilized in FOXP3 Perm/Wash Buffer (Biolegend #421403) at room temperature for 15 minutes, spun, and stained with anti-CTLA4 antibody (Biolegend #349908) in 1x FOXP3 Perm/Wash Buffer at room temperature for 30 minutes. Cells were washed twice in cold EasySep buffer and resuspended at 40e6 cells/mL in cold EasySep buffer and stored at 4°C until FACS. For T_{reg} cell screens, all samples were carried through permeabilization and stained with HELIOS (Biolegend #137216) and FOXP3 (Biolegend #320112) antibodies.

After fluorescent compensation with single-stained control samples, the highest and lowest 20% expression bins for each target (CD28, CTLA4, ICOS) were sorted into cold EasySep buffer at the Parnassus Flow Cytometry Core Facility (PFCC) and/or Gladstone Flow Cytometry Core using Aria II, Aria III, and Aria Fusion (BD Biosciences) cell sorters. We recovered and processed libraries for >200-fold cells:sgRNA coverage for all samples except Donor 1 T_{reg} cells, ICOS screen (>140-fold cells:sgRNA coverage). Sorted samples were pelleted and resuspended in ChIP Lysis Buffer (400ul per 5e6 cells) for library prep as previously described[46]. Sequencing libraries were generated as previously described (Broad Institute "Protocol PCR of sgRNAs from gDNA for Illumina sequencing") with minor changes. Up to 3.75ug genomic DNA was loaded into each 50uL PCR reaction with 0.25uM p5 forward primer (5'-AATGATACGGCGACCACCGAGATCTGCACAAAAGGAAACTCACCCT) and 0.25uM unique p7 reverse primer (5'-CAAGCAGAAGACGGCATACGAGAT[NNNNNNNNN]GTGACTGGAGTTCAGACGTGTGCTCTTCCGATCTCGACTCGGTGCCACTTTTTC). PCR reactions were run with the following parameters: 95°C 1', [95°C 30", 60°C 30", 72°C 30"] x 28, 72°C 10', 4°C hold. PCR reactions were purified as previously described[87] (Zymo Research #D4033) and eluted in 12ul per 1e6 cell genomic DNA inputted. One sample (Donor 2 T_{conv} cells, ICOS screen) was re-

indexed before sequencing. Pooled libraries were sequenced with a custom sequencing primer (5'-GTGTGTTTTGAGACTATAAGTATCCCTTGGAGAACCACCTTGTTG) on an Illumina NextSeq500 instrument targeting >200-fold read:sgRNA coverage per sample.

CRISPRi Screen Analysis

Raw Illumina sequencing data were demultiplexed and fastqs generated using bcl2fastq (v2.20.0, Illumina). Short guide RNA abundances were quantified using MAGeCK (v0.5.9.4)[88] with a reference file listing sgRNA sequences, an arbitrary ID, and the 5' genomic position of the sgRNA (hg38). Unnormalized sgRNA count files for each sample were loaded into R (v4.1.2), and statistical testing of sgRNA effects across two donors per sample was performed with DESeq2 (v1.34.0) using the default Wald test and Benjamini-Hochberg Procedure to correct for multiple hypotheses[89]. To highlight genetic windows of CRISPRi effects for prioritizing variants affecting *CTLA4*, we subsetted our data to all significant sgRNAs identified in any of the *CTLA4* CRISPRi screens (Adjusted P-value < 0.05) and examined the distance between adjacent sgRNAs (Figure S4.2D). Using this strategy, we called CiREs based on runs of sgRNAs less than 500bp from the previous sgRNA, setting the peak boundaries to the genomic start positions of the first and last sgRNAs within the CiRE.

CRISPR Knockout Screens and Analysis

CRISPR knockout screens and analyses were performed in MAGeCK as previously described[47]. Unstimulated cells were used for CD28 screens, and cells restimulated for 24 hours with Cell Activation Cocktail without Brefeldin A (Biolegend #423302) were used for ICOS screens.

Arrayed Validation

T_{conv} and T_{reg} cells were isolated from matched donors described above. Immediately after magnetic isolation, $CD25^+CD127^{low}$ T_{reg} cells were further enriched for purity using fluorescence-activated cell sorting (Biolegend #302618; Becton Dickinson #557938). Arrayed sgRNA lentiviral

supernatants were harvested from 6-well plates and concentrated to 1/10th volumes, and dCas9-ZIM3 lentivirus was produced as with the pooled screens. T cells were activated, sequentially transduced with saturating dCas9-ZIM3 and sgRNA lentiviruses, subjected to puro selection, and assayed on day 8 or 9.

For arrayed CRISPR KO experiments, cells were activated for 2 days before nucleofection. Lyophilized Edit-R crRNA (Dharmacon) were ordered for each target in an arrayed format. crRNAs and Edit-R CRISPR-Cas9 Synthetic tracrRNA (Dharmacon #U-002005-20) were resuspended to 160mM in nuclease-free duplex buffer (IDT #11-05-01-03), mixed at a 1:1 ratio for a 80 mM solution, and incubated at 37°C for 30 minutes. Single-stranded donor oligonucleotides enhancer from IDT (ssODN;

TTAGCTCTGTTTACGTCCCAGCGGGCATGAGAGTAACAAGAGGGTGTGGTAATATTACGGT ACCGAGCACTATCGATACAATATGTGTCATACGGACACG) was added at a 1:1 molar ratio of the final Cas9-Guide complex, mixed well by pipetting, and incubated for an additional 5 minutes at 37°C. Cas9 protein (UCB MacroLab, 40uM) was added at a 1:1 ratio, mixed thoroughly by pipetting, and incubated at 37°C for 15 minutes. Prepared Cas9 ribonucleoproteins (RNPs) were distributed into a 96-well plate. Stimulated cells were pelleted at 90g for 10 minutes in a 25°C centrifuge, the supernatant removed, and resuspended at 1e6 cells per 20uL supplemented Buffer P3 (Lonza #V4SP-3096). Prepared cells were distributed into the plate with RNPs, mixed gently, and transferred to the 96-well Nucleocuvette Plate (Lonza) for nucleofection (DS-137, Amaxa Nucleofector 96-well Shuttle System). Cells were recovered in 80uL pre-warmed cXVIVO media and placed in the incubator for 10 minutes. Nucleofected cells were then distributed into 96-well plates (Fisher #353077) at 1e6 cells/mL in cXVIVO supplemented with rhIL-2 and passaged every two days until analysis.

For the CRISPRa experiment with ΔCTCF-2 excision, arrayed sgRNA lentiviral supernatants were harvested from 6-well plates and concentrated to 1/10th volumes. The pZR112_Lenti-SFFV-mCherry-2A-dCas9-VP64 (Addgene #180263) CRISPRa lentivirus was

produced the same as dCas9-ZIM3 lentivirus described above. Freshly isolated and unstimulated T_{reg} and T_{conv} cells were nucleofected (Buffer P3, DS-137, Amaxa Nucleofector 96-well Shuttle System) with 50 pmol each of two Cas9 RNPs (100 pmol total) flanking the CTCF-2 region (509bp) or a control region in the AAVS1 locus (582bp). PCR analysis of the targeted regions revealed ~50% excision efficiency. Nucleofected cells were recovered in pre-warmed cX-VIVO for 30 minutes at 37°C and 5% CO_2 and then transferred to flasks at 1e6 cells per mL cXVIVO supplemented with Dynabeads, 300U/mL rhIL-2, and 1uM M3814 (Selleckchem #S8586). Activated cells were sequentially transduced with saturating dCas9-VP64 and sgRNA lentiviruses 24 and 48 hours later, respectively, subjected to puro selection 24 hours later, and assayed on day 9 as previously described[46].

For all validation experiments, protein expression was measured using the Attune NxT flow cytometer (Thermo Fisher) and analyzed in FlowJo (v10.8.1) and R (v4.1.2). The number of arrayed sgRNAs analyzed per donor for each experiment is indicated in the figure legend, as only samples with 500 or more cells remaining after QC and gating were carried through for analysis. Median Fluorescence Intensity (MFI) values for each sample were normalized to mean MFI values for donor-matched controls (Fold Change). Significance tests were performed with ggpubr (v0.4.0) "stat_cor" and "compare_means" functions. Adjusted P-values (Holm method) are reported for all mean comparisons.

4C-Seq

T_{conv} cells from two human donors (1e7 per donor) were perturbed with CRISPRi targeting of the CTCF-2 boundary or Non-Targeting Control as described above. Nine days after the initial activation, cells were restimulated for 6 hours with 1ul/mL Cell Activation Cocktail without Brefeldin A and then snap frozen. Cell pellets were thawed, fixed with 1% PFA, and re-pelleted. Cell pellets were resuspended with 500ul 4C lysis buffer (50mM Tris-HCl pH 7.5, 150mM NaCl, 5mM EDTA, 0.5% NP-40 (IGEPAL CA-630), 1% Triton-X100, and 1X protease inhibitors (ThermoFisher #1862209)). The pellet was then pipetted vigorously and incubated on ice for 10

minutes for cell lysis. The nuclear pellet was spun down at 750G for 5 minutes at 4°C and washed twice with ice cold PBS. Next, the nuclear pellet was resuspended in H_2O and 1X rCutSmart buffer (with HindIII-HF, NEB #R3104T). 0.25% SDS and 2.5% Triton-X100 were added for denaturation at 37°C for one hour on a thermomixer set to 900 rpm. Genomic DNA was digested with 400UI-600UI HindIII-HF (NEB #R3104T) overnight before heat inactivation on the second day. Digested genomic DNA was ligated by T4 DNA ligase system (NEB, Cat#M0202T) at room temperature for 4 hours. The mixture was digested by proteinase K (ThermoFisher #EO0491) and RNase (Roche #11119915001) to remove remaining proteins and contaminating RNA. The circled genomic DNA was purified by phenol-chloroform purification method. The DNA pellet was resuspended in TE buffer and subjected to DpnII secondary digestion overnight (200UI, NEB #R0543T) before heat inactivation on the second day. DNA was again ligated using the T4 DNA ligase system (NEB #M0202T) at room temperature for 4 hours and then pelleted with 60mM sodium acetate, 3ug/ml glycogen, and 70% Ethanol.

The digested DNA then went to PCR amplification for CiRE view-point interactions. Two probe sets spanning the entire Stim-Responsive CiRE were tested, but only the probe covering the latter half of the enhancer region (which aligns with maximum CRISPRi responsiveness) yielded sufficiently diverse libraries and is included here. We used the view primer sequence CAAGCTATATGCCCAAGCTT and non-view primer sequence AATGCTCTGGGACAGTGA. Forward primer was designed as reading adapter+view primer, with the whole sequence as: AATGATACGGCGACCACCGAGATCTACACTCTTTCCCTACACGACGCTCTTCCGATCTCAA GCTATATGCCCAAGCTT. Reverse primer was designed as indexed non-reading adapter+non-view primer, with the whole sequence as: CAAGCAGAAGACGGCATACGAGATNNNNNNNNGTGACTGGAGTTCAGACGTGTGCTCTTC CGATCT AATGCTCTGGGACAGTGA. PCR was performed on 200ng DNA using Platinum™ SuperFi™ DNA Polymerase system (ThermoFisher, cat#12351010) with the program [98°C 10",

52°C 10", 72°C 1'] x 30 cycles. SPRI clean-up was performed to isolate the final amplified library, and the final library was quantified and sequenced on a NextSeq 500 with 75 cycle kits.

4C-Seq Analysis

4C sequencing reads were processed and aligned to hg38 using pipe4C processing pipeline[90], normalizing to one million reads and using a default window size of 21. The resulting wig files were imported in R and smoothed using spline models with a smoothing parameter of 0.75. The gene track was plotted using R package Sushi[91] for the genomic region of interest (chr2: 203500000-203967032204100000), and smoothed wig files were plotted in the given region using R base plot function. The level of interaction between CD28 and CTLA4 with the viewpoint were quantified using pipe4C's RDS files, where the normalized 4C signal of the captured fragments was extracted for the gene body of each gene (chr2:203706475-203738912 for CD28 and chr2:203867771-203873965 for CTLA4), log transformed, and plotted in a boxplot.

4C resulted in satisfactory quality parameters according to established guidelines[90], where over 55% of the reads mapped in the viewpoint chromosome. More than 40% of the total coverage mapped within 1Mb of the viewpoint, and over 55% of fragments within 100Kb of the viewpoint were captured in any sample.

Genomic Data Access and Processing

HiC data[57] in Figure 4.1 were accessed with the 3D Genome Browser[92]. HiC data for Figure 4.5 were extracted from the ENCODE portal[84] with the identifier ENCSR421CGL. ATAC-Seq profiles were sourced from GSE118189[93] and GSE171737[47]. ChIP-Seq profiles of histone modifications were generated by the NIH Roadmap Epigenomics Mapping Consortium (https://egg2.wustl.edu/). Summary statistics from trans-ethnic GWAS meta-analysis for rheumatoid arthritis[30] and single cell genetic analysis of lupus erythematosus[94] were loaded into R (v4.1.2), lifted from hg19 to hg38 with a chain file (UCSC) using the liftOver function (rtracklayer v1.48.0), and linkage disequilibrium relative to the lead variant rs3087243 was calculated with

LDlinkR (v1.2.0). Homology of adjacent gene promoters was examined in Benchling's alignment tool. RNA-seq of differentiated T_{conv} cells was sourced from the Database of Immune Cell Expression, Expression quantitative trait loci (eQTLs) and Epigenomics (DICE) project[95]. Whenever possible, care was taken to select publicly-available genomic data gathered from the same primary human T cell subsets under the same activation conditions assayed in the present study. ChIP-Seq data for STAT5B and IRF4 were sourced from GSE43119[96] and GSM2810038, respectively.

Trans regulator screening results for *CTLA4*, RNA sequencing in the setting of *trans* regulator knockout, and ATAC-seq profiles of *trans* regulator knockout T_{conv} cells were recently published under GSE171737[47]. To identify transcription factor motifs enriched in ATAC-Seq peaks altered by ZNF217 knockout, bed files of called ATAC-Seq peaks gaining or losing log2FC=|0.3| were compared to one another using the findMotifsGenome script from HOMER (v4.11) with `–size 350`. Gene set enrichment of differentially-expressed genes between ZNF217 knockout and control RNA-Seq samples was performed in R (v4.1.2) with enrichR (v3.0) using databases KEGG_2021_Human and GO_Biological_Process_2021. Stimulation-responsive ATAC-seq data for T_{conv} (used in all figures without perturbation ATAC-seq) and T_{reg} cells (used in all figures) are published under GSE118189[93].

CTCF ChIA-PET was generated by the ENCODE Project Consortium[67] and processed in R to plot only loops (A) detected in samples from two biological replicates within 5kb and (B) originating and ending in the visualized region. ChIP-seq profiles of CTCF in CD4+ T cells from healthy control subjects were sourced from GSE164215[97]. Genome tracks for gene positions, retrotransposable elements, and 30-way PhastCons were downloaded from the UCSC Genome Browser. CTCF motifs were identified with FIMO using the MA0139.1 motif from JASPAR.

Plotting of ATAC-Seq and ChIP-Seq data was performed with ggplot2 (v3.3.5) and pyGenomeTracks (v3.6).

4.6: Figures
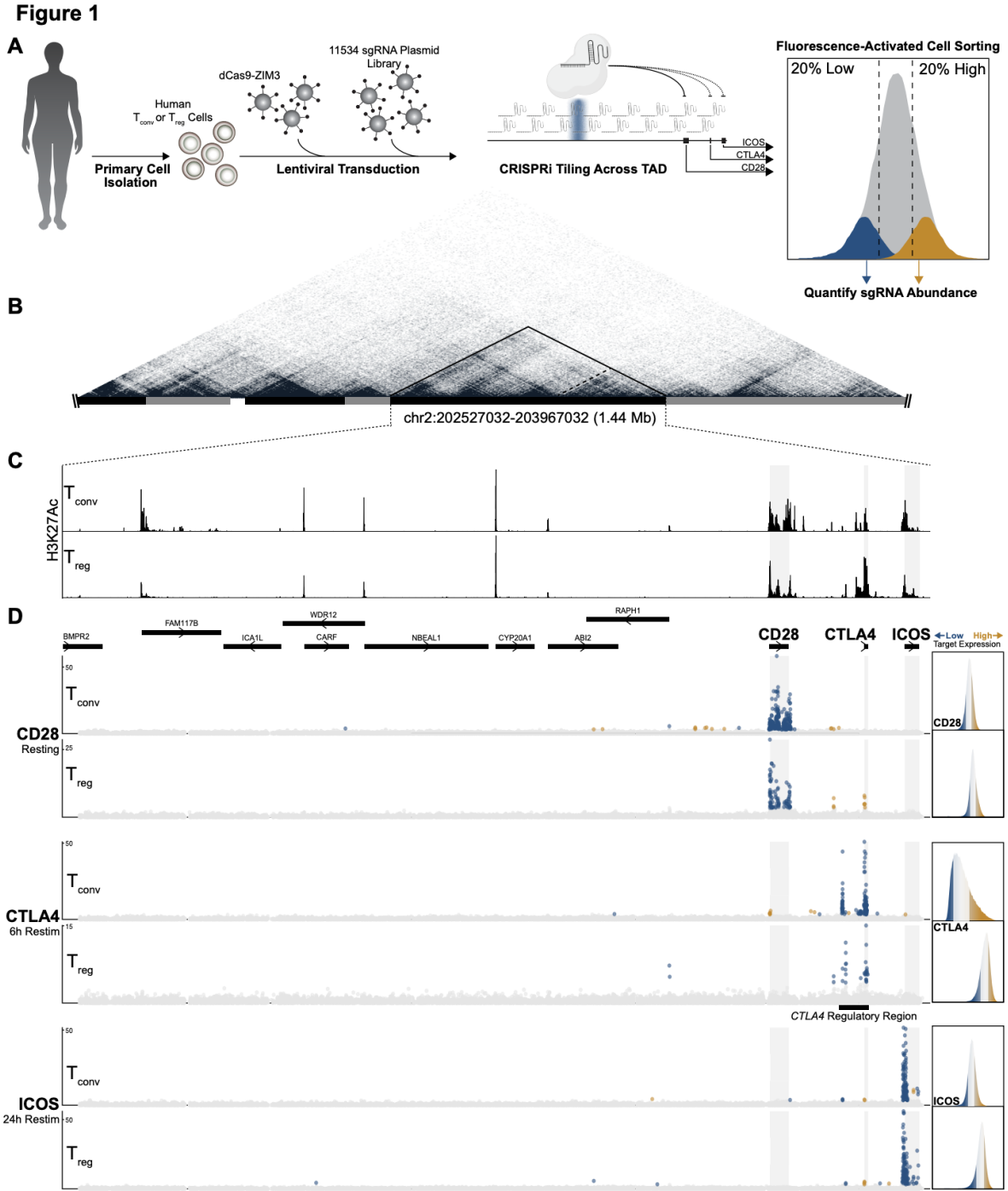
Figure 1

Figure 4.1: Tiling CRISPRi screens map gene-specific *cis*-regulatory elements across the costimulatory locus.

A. Schematic overview of CRISPRi screening workflow. B. HiC contact plot from GM12878 originally used to design the CRISPRi sgRNA library (see Methods), with annotated TADs (black

and gray bars). The TAD harboring the 2q33.2 costimulatory locus is outlined and expanded in panels C-D. C. H3K27 acetylation in T_{conv} (top) and T_{reg} (bottom) cells across the TAD designated in B. D. Gene bodies throughout the locus atop CRISPRi tiling screen results for each target gene (rows) in T_{conv} (top) and T_{reg} (bottom) cells from two human donors across the TAD designated in B. Each point signifies the genomic position (x) and -log10(unadjusted P-value) (y) of the sgRNA. Blue indicates sgRNAs significantly enriched (Adjusted P-value<0.05) in the lowest 20% of target protein-expressing cells, and gold indicates sgRNAs significantly enriched (Adjusted P-value<0.05) in the highest 20% of target protein-expressing cells. FACS histograms of target protein expression for each screen are included in the right margin, including the gated populations isolated for sgRNA quantification. The window labeled "*CTLA4* Regulatory Region" is expanded in Figure 4.2.
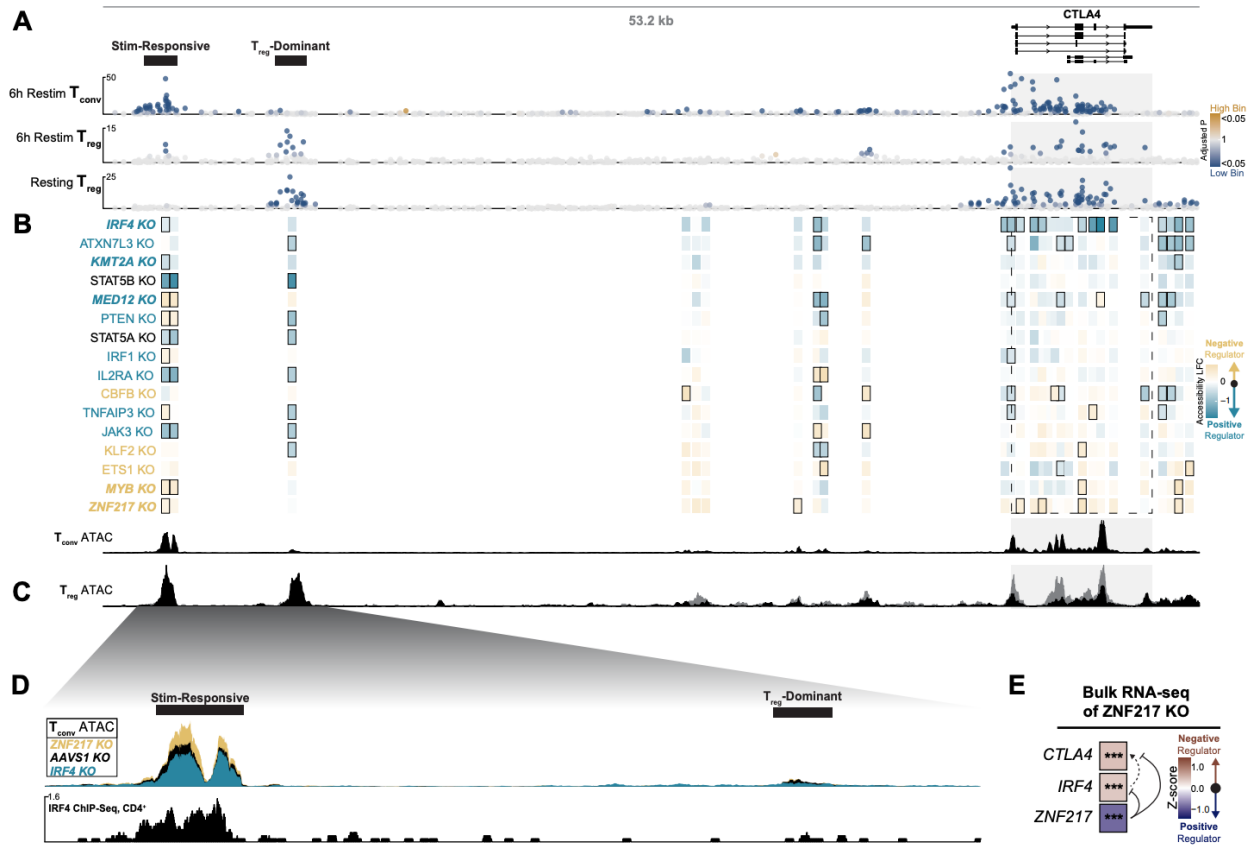
Figure 2
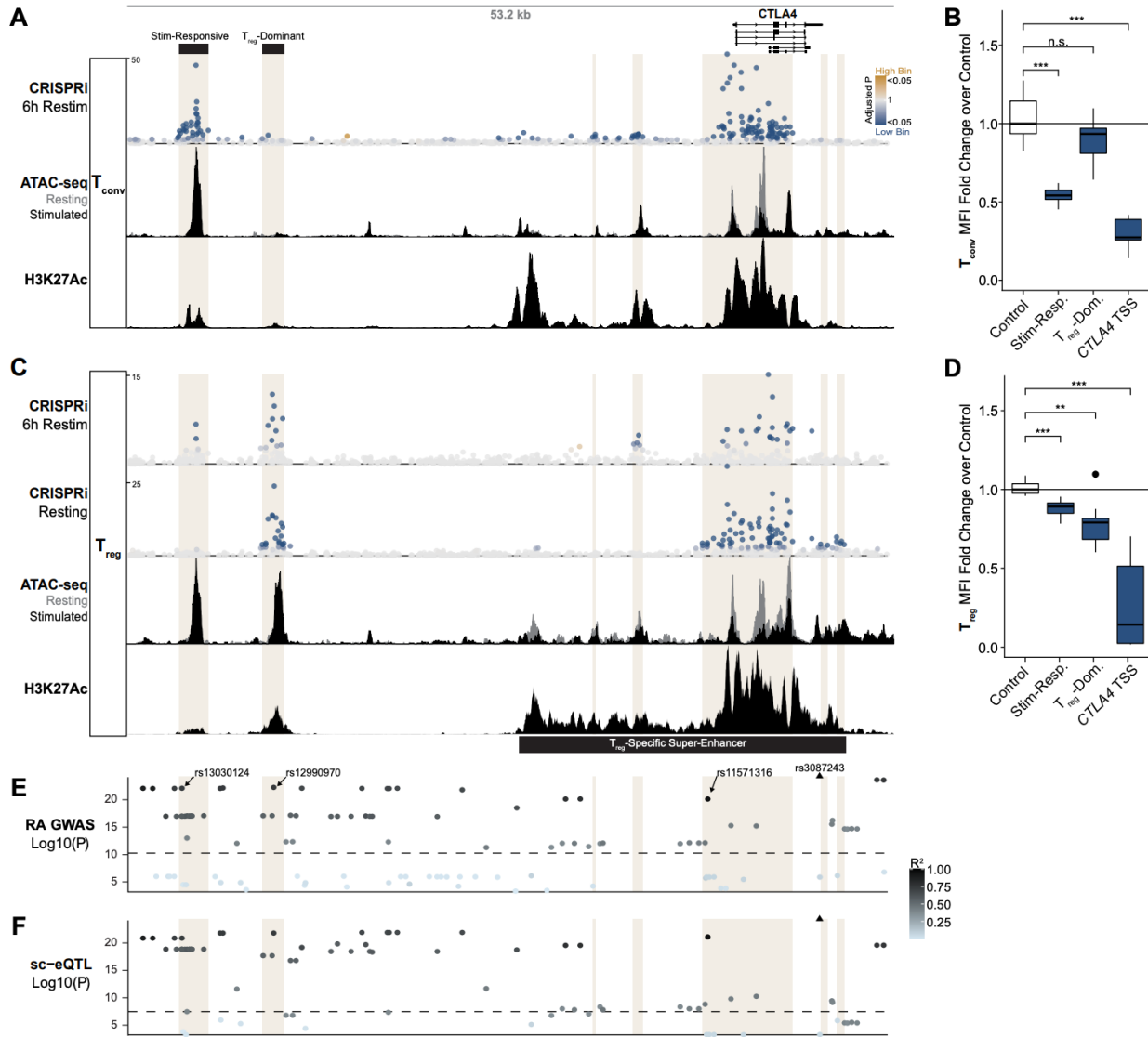
Figure 4.2: Context-restricted CTLA4 enhancers colocalize with autoimmunity risk variants.

A. Genomic profiles around the *CTLA4* gene body (indicated by the isoform diagram) in the "*CTLA4* Regulatory Region" indicated in Figure 4.1D. Top: CRISPRi tiling results in T_{conv} cells restimulated for 6 hours. Middle: ATAC-Seq profiles of resting (gray) and stimulated (black) T_{conv} cells. Bottom: H3K27ac profile of T_{conv} cells. Beige columns highlight genomic regions with significant sgRNAs across all CTLA4 CRISPRi screens less than 500bp from the previous significant sgRNA (see Methods). For all CRISPRi tiling results, each point signifies the genomic position (x) and -log10(unadjusted P-value) (y) of the sgRNA. Blue indicates sgRNAs enriched in the lowest 20th percentile of cells, and gold indicates sgRNAs enriched in the highest 20th percentile of cells. The fill gradients indicate increasing significance of sgRNA enrichment, with maximum colors signifying Adjusted P-value < 0.05. B. Fold change of CTLA4 median fluorescence intensity in primary T_{conv} cells from two human donors restimulated for 6h under arrayed CRISPRi validation of sgRNAs targeting the Stim-Responsive CiRE (N=4 sgRNAs), T_{reg}-Dominant CiRE (N=4), or *CTLA4* TSS (N=5 for Donor 1, N=3 for Donor 2) relative to non-targeting

96

Controls (N=7 for Donor 1, N=6 for Donor 2) for each donor. Mean values were compared to the Control group using the Student's T-test with Holm correction. C. Top: CRISPRi tiling results in T_{reg} cells restimulated for 6 hours. Fill gradients match those in panel A. Top Middle: CRISPRi tiling results in T_{reg} cells without restimulation. Bottom Middle: ATAC-Seq profiles of resting (gray) and stimulated (black) T_{reg} cells. Bottom: H3K27ac profile of T_{reg} cells. The T_{reg}-specific H3K27Ac super-enhancer annotation is approximated based on prior studies[41]. D. Fold change of CTLA4 median fluorescence intensity in restimulated primary T_{reg} cells from two human donors under arrayed CRISPRi validation of sgRNAs targeting the Stim-Responsive CiRE (N=4), T_{reg}-Dominant CiRE (N=4), or *CTLA4* TSS (N=5) relative to non-targeting Controls (N=7) for each donor. Mean values were compared to the Control group using the Student's T-test with Holm correction. E. Genetic variants and their -log10(P-value) association with rheumatoid arthritis risk. Triangle indicates the lead index SNP from the study. Fill color indicates linkage disequilibrium to the lead SNP. Arrows point to other variants nominated by CRISPRi screens and in strong LD with the lead SNP. Dashed line indicates genome-wide significance threshold ($p < 5x10^{-8}$). F. Genetic variants and their -log10(P-value) association with altered *CTLA4* expression. Triangle indicates the lead index SNP from the study. Fill color indicates linkage disequilibrium to the lead SNP. Arrows point to example candidate causal SNPs prioritized by CRISPRi screens. Dashed line indicates genome-wide significance threshold ($p < 5x10^{-8}$). For all panels: *P < 0.05, **P < 0.01, ***P < 0.005.
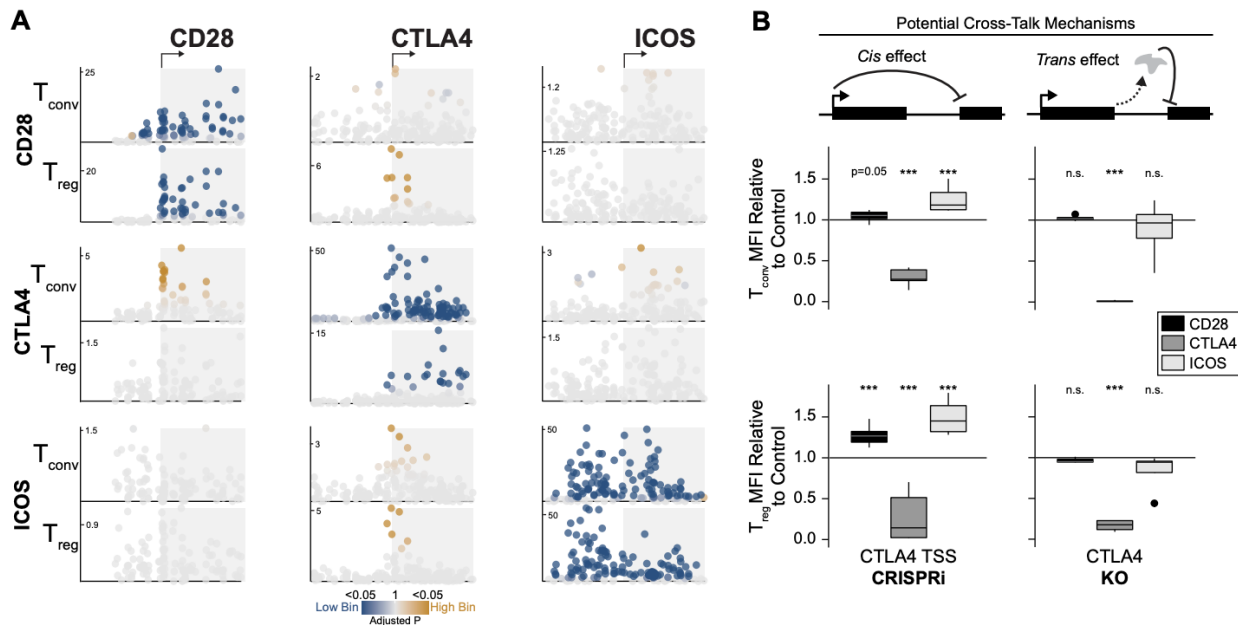
Figure 3

Figure 4.3: Linking *trans* regulators of CTLA4 to CRISPRi-Responsive Elements via ATAC-Seq of perturbed cells.

A. CRISPRi tiling results for CTLA4 in T_{conv} cells restimulated 6 hours (top), T_{reg} cells restimulated 6 hours (middle), and T_{reg} cells without restimulation (bottom) around the *CTLA4* gene body. CiRE regions are manually annotated. For all CRISPRi tiling results, each point signifies the genomic position (x) and -log10(unadjusted P-value) (y) of the sgRNA. Blue indicates sgRNAs enriched in the lowest 20th percentile of cells, and gold indicates sgRNAs enriched in the highest 20th percentile of cells. The fill gradients indicate increasing significance of sgRNA enrichment, with maximum colors signifying Adjusted P-value < 0.05. B. Effect of *trans* regulator knockout on ATAC-Seq accessibility. Dashed outline indicates *CTLA4* gene body. Blue indicates positive regulation (i.e. *trans* regulator knockout decreases peak accessibility), and gold indicates negative regulation. Black tile outlines indicate significant changes in peak accessibility. Colored *trans* regulator labels indicate those significantly regulating CTLA4 expression either positively (blue) or negatively (gold) according to either the *trans* regulator screens or arrayed RNA-seq validation, and bolded and italicized labels have concordant significant effects between the *trans* regulator screens and arrayed RNA-seq validation. Bottom: ATAC-Seq of AAVS1 KO T_{conv} cell control samples from the profiling experiment. C. Public ATAC-Seq of resting (gray) and restimulated (black) T_{reg} cells from a separate experiment. D. Top: ATAC-Seq of T_{conv} cells with either ZNF217 (yellow), AAVS1 control (black), or IRF4 (blue) KO. Bottom: Public IRF4 ChIP-Seq in CD4^{+} T cells. CiRE regions are manually annotated. E. Changes in *CTLA4*, *IRF4*, and *ZNF217* expression as measured by bulk RNA-seq in the setting of ZNF217 KO in human T_{conv} cells[47]. Data supporting

positive regulation of IRF4 on *CTLA4* are plotted in Figures S3B and S3C. Asterisks indicate FDR-adjusted *P* from Limma. For all panels: *P < 0.05, **P < 0.01, ***P < 0.005, n.s. Not Significant.
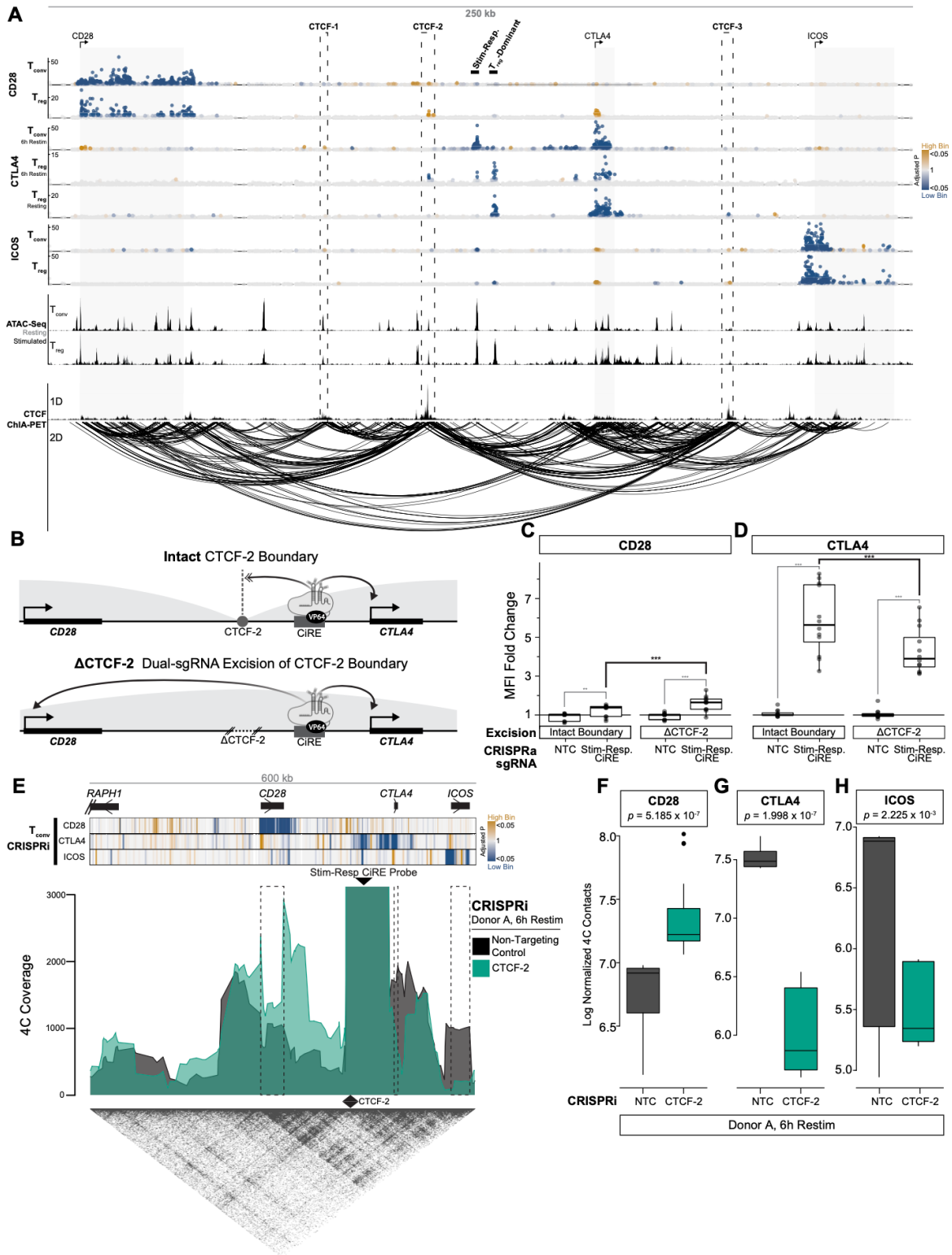
Figure 4

Figure 4.4: Gene co-regulation evidenced by CRISPRi and *trans* KO screens.

A. CRISPRi tiling screen results for each target gene (rows) in T_{conv} (top) and T_{reg} (bottom) cells at the three transcriptional start sites (columns). For all CRISPRi tiling results, each point signifies the genomic position (x) and -log10(unadjusted P-value) (y) of the sgRNA. Blue indicates sgRNAs enriched in the lowest 20th percentile of cells, and gold indicates sgRNAs enriched in the highest 20th percentile of cells. The fill gradients indicate increasing significance of sgRNA enrichment, with maximum colors signifying Adjusted P-value < 0.05. B. Target protein expression in cells from two human donors after CRISPRi targeting of the *CTLA4* TSS (left, N=3 sgRNAs for Donor 2 T_{conv} samples, N=5 sgRNAs for all other samples) or CRISPR Knockout of *CTLA4* downstream of the TSS (right, N=1 sgRNA for Donor 1 T_{conv} CD28 sample, N=2 sgRNAs for all other samples). Plotted are Median Fluorescence Intensity values normalized to Non-Targeting (CRISPRi, N=6 sgRNAs for Donor 2 T_{conv} samples, N=7 sgRNAs for all other samples) or AAVS1 (KO, N=6 sgRNAs for all samples) controls for each target gene (fill color) in T_{conv} (top) and T_{reg} (bottom) cells. Significance calculated with the Student's t-test with Holm correction. For all panels: $*P < 0.05$, $**P < 0.01$, $***P < 0.005$, n.s. Not Significant.
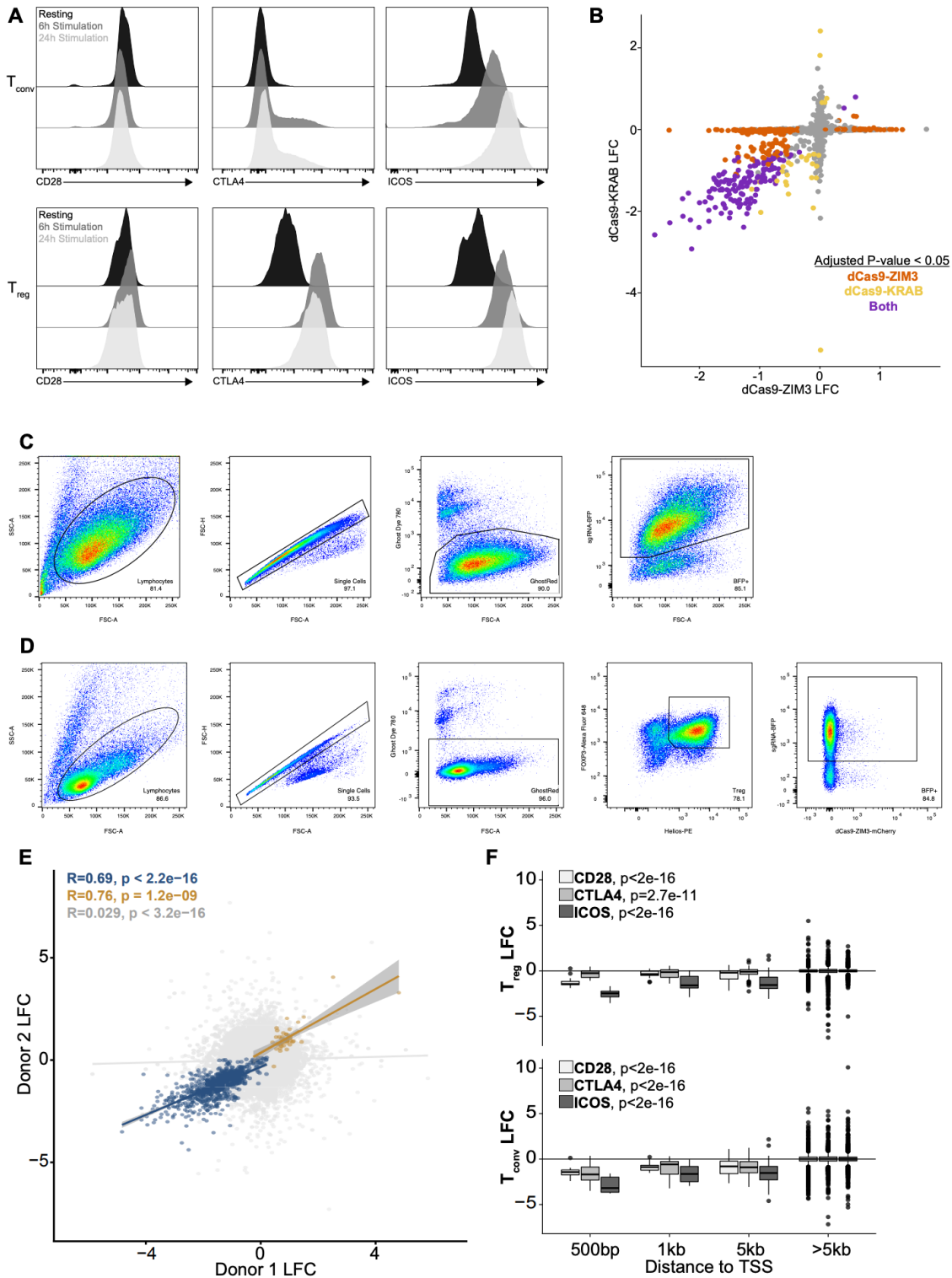
Figure 5

Figure 4.5: CTCF boundary sites coordinate enhancer looping to costimulatory genes.
A. Top: CRISPRi tiling screen results for each target gene (rows) in T_{conv} (top) and T_{reg} (bottom)
cells. Gray bars indicate costimulatory gene bodies, and the Stim-Responsive and T_{reg}-Dominant

CiREs are manually labeled. For all CRISPRi tiling results, each point signifies the genomic position (x) and -log10(unadjusted P-value) (y) of the sgRNA. Blue indicates sgRNAs enriched in the lowest 20th percentile of cells, and gold indicates sgRNAs enriched in the highest 20th percentile of cells. The fill gradients indicate increasing significance of sgRNA enrichment, with maximum colors signifying Adjusted P-value < 0.05. Middle: ATAC-Seq profiles in T_{conv} (top) and T_{reg} (bottom) cells. Bottom: 1- (top) and 2-Dimensional (bottom) CTCF-bound genomic contacts identified by ChIA-PET in human CD4$^+$ T cells filtered for contacts that (1) both originate and end in the target locus and (2) are shared between two donors within 5kb. Dashed outlines indicate CRISPRi-responsive elements colocalizing with CTCF ChIA-PET peaks. B. Schematic overview of conditions plotted in C and D. CRISPRa was recruited to the Stim-Responsive CTLA4 enhancer in the setting of an intact CTCF-2 boundary region (top) or in the setting of dual-sgRNA mediated excision (Figure S4.7B) of the CTCF-2 boundary region (bottom). C. Changes in CD28 Median Fluorescence Intensity (MFI) in the setting of Non-Targeting Control (NTC, N=3 sgRNAs, light color) or Stim-Responsive CiRE (N=3 sgRNAs, dark color) targeting by CRISPRa with either AAVS1 control region ("Intact Boundary", left) or CTCF-2 boundary region ("ΔCTCF-2", right) excision in T_{conv} cells from four human donors. Each sample is normalized to CRISPRa non-targeting control MFI mean after AAVS1 control region or CTCF-2 region excision. D. Changes in CTLA4 MFI in the setting of Non-Targeting Control (NTC, N=3 sgRNAs, light color) or Stim-Responsive CiRE (N=3 sgRNAs, dark color) targeting by CRISPRa after AAVS1 control region ("Intact Boundary", left) or CTCF-2 boundary region ("ΔCTCF-2", right) excision. Each sample is normalized to CRISPRa non-targeting control MFI mean after AAVS1 control region or CTCF-2 region excision in T_{conv} cells from four human donors. For both C and D, the results of Student's t-test with Holm correction comparing NTC and Stim-Responsive CiRE CRISPRa are included in gray, and the results of paired Student's t-test with Holm correction comparing Stim-Responsive CiRE CRISPRa in Intact Boundary or ΔCTCF-2 conditions are included in black. E. 4C-seq plot for CTCF-2 CRISPRi Tconv cells from one donor, anchored on Stim-Responsive CiRE, plotting contacts in Non-Targeting Control (black) and CTCF-2 targeting (green) conditions. CRISPRi tiling screen results in T_{conv} cells are plotted, where each bar signifies the genomic position (x) and -log10(Adjusted P-value) (fill) of the sgRNA. Maximum colors signify Adjusted P-value < 0.05. HiC from intact CD4+ T cells[84] is shown at the bottom. Scale bar indicates genomic region that is plotted. The 4C viewpoint and CTCF-2 boundary are indicated by arrowheads. Dashed box regions indicate *CD28*, *CTLA4,* and *ICOS* (left to right) gene bodies. Biological replicate data are included in Figure S4.7. F. Normalized 4C signal intensity between Non-Targeting Control and CTCF-2 CRISPRi targeting groups for the *CD28* gene body. G. Normalized 4C signal intensity between Non-Targeting Control and CTCF-2 CRISPRi targeting groups for the *CTLA4* gene body. H. Normalized 4C signal intensity between Non-Targeting Control and CTCF-2 CRISPRi targeting groups for the *ICOS* gene body. For F-H, each dot represents the log-transformed 4C signal intensity of each captured genomic region in either the *CD28*, *CTLA4,* or *ICOS* gene body (see Methods). For all panels: *P < 0.05, **P < 0.01, ***P < 0.005, n.s. Not Significant.

Figure S4.1: Target protein expression and CRISPRi tiling screen preparations.
A. Protein expression of CD28 (left), CTLA4 (middle) and ICOS (right) in T$_{conv}$ (top) and T$_{reg}$ (bottom) cells after 0 hours (black), 6 hours (dark gray), or 24 hours (light gray) after restimulation.

B. Examination of high versus low protein bin sgRNA enrichment (log2) matched by gene target in bulk CD4$^+$ T cells from one human donor. Colors indicate significant (Adjusted P-value < 0.05) sgRNA enrichment with the dCas9-ZIM3 (orange), dCas9-KRAB (yellow), or both (purple) CRISPRi systems. C. Representative FACS gating strategy for CRISPRi screens in T$_{conv}$ cells. D. Representative FACS gating strategy for CRISPRi screens in T$_{reg}$ cells. E. Correlation of log2(Fold Change) sgRNA enrichment between high versus low protein bins matched by cell type and gene target for each donor. Blue sgRNAs were significantly enriched in the low bin (Adjusted P-value < 0.05, LFC < 0), gold sgRNAs were significantly enriched in the high bin (Adjusted P-value < 0.05, LFC > 0), and grey sgRNAs were non-significant (Adjusted P-value > 0.05). Inset includes Pearson statistics for each group. F. Log2(Fold Change) sgRNA enrichment between high versus low protein bins for each gene target and cell type categorized by distance to the target gene transcriptional start site. Adjusted P-values were calculated with the ANOVA test for each target per cell type.
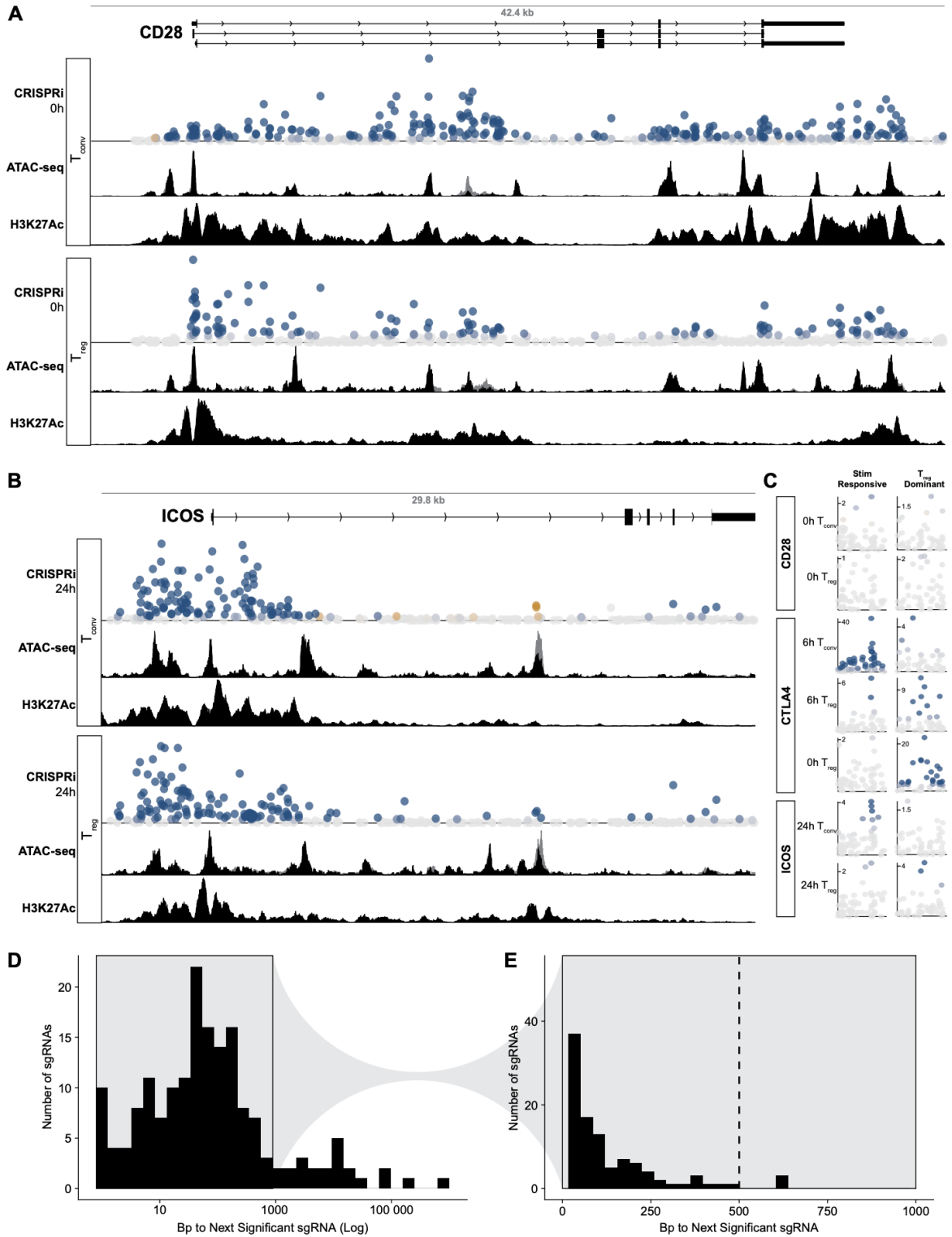
Figure S4.2: Tiling CRISPRi screens chart *cis* regulation of CD28 and ICOS expression.
A. Genomic profiles of T_{conv} and T_{reg} cells at the *CD28* gene body as indicated by the isoform diagrams at top. Top: CRISPRi, ATAC-seq, and H3K27ac ChIP-seq profiles in T_{conv} cells. Bottom:

CRISPRi, ATAC-seq, and H3K27ac ChIP-seq profiles in T$_{reg}$ cells. For ATAC-Seq profiles, accessibility for both resting (gray) and stimulated (black) T$_{conv}$ cells are plotted. Gray columns indicate the *CD28* gene body. B. Genomic profiles of T$_{conv}$ and T$_{reg}$ cells at the *ICOS* gene body as indicated by the isoform diagrams at top. Top: CRISPRi, ATAC-seq, and H3K27ac ChIP-seq profiles in T$_{conv}$ cells. Bottom: CRISPRi, ATAC-seq, and H3K27ac ChIP-seq profiles in T$_{reg}$ cells. For ATAC-Seq profiles, accessibility for both resting (gray) and stimulated (black) T$_{conv}$ cells are plotted. Gray columns indicate the *CD28* gene body. C. CRISPR results for each cell type, restimulation condition, and target gene at the Stim-Responsive and T$_{reg}$-Dominant CiREs described in Figure 4.2. For all CRISPRi tiling results, each point signifies the genomic position (x) and -log10(unadjusted P-value) (y) of the sgRNA. Blue indicates sgRNAs enriched in the lowest 20th percentile of cells, and gold indicates sgRNAs enriched in the highest 20th percentile of cells. The fill gradients indicate increasing significance of sgRNA enrichment, with maximum colors signifying Adjusted P-value < 0.05. D. Log-transformed distribution of genomic distance (Basepair, Bp) for each significant sgRNA (Adjusted P-value < 0.05) to the next significant sgRNA across all CTLA4 CRISPRi screens. Subset under 1kb (gray box with black outline) is re-plotted in E. E. Non-transformed (linear) representation of the subset of genomic distances plotted in D (gray box with black outline) thresholded on inter-sgRNA distances less than 1kb. A cutoff of 500bp to the next significant sgRNA (dashed line) at the end of the distribution tail was used to identify CiREs for Figure 4.2 (beige regions) in an unbiased way.
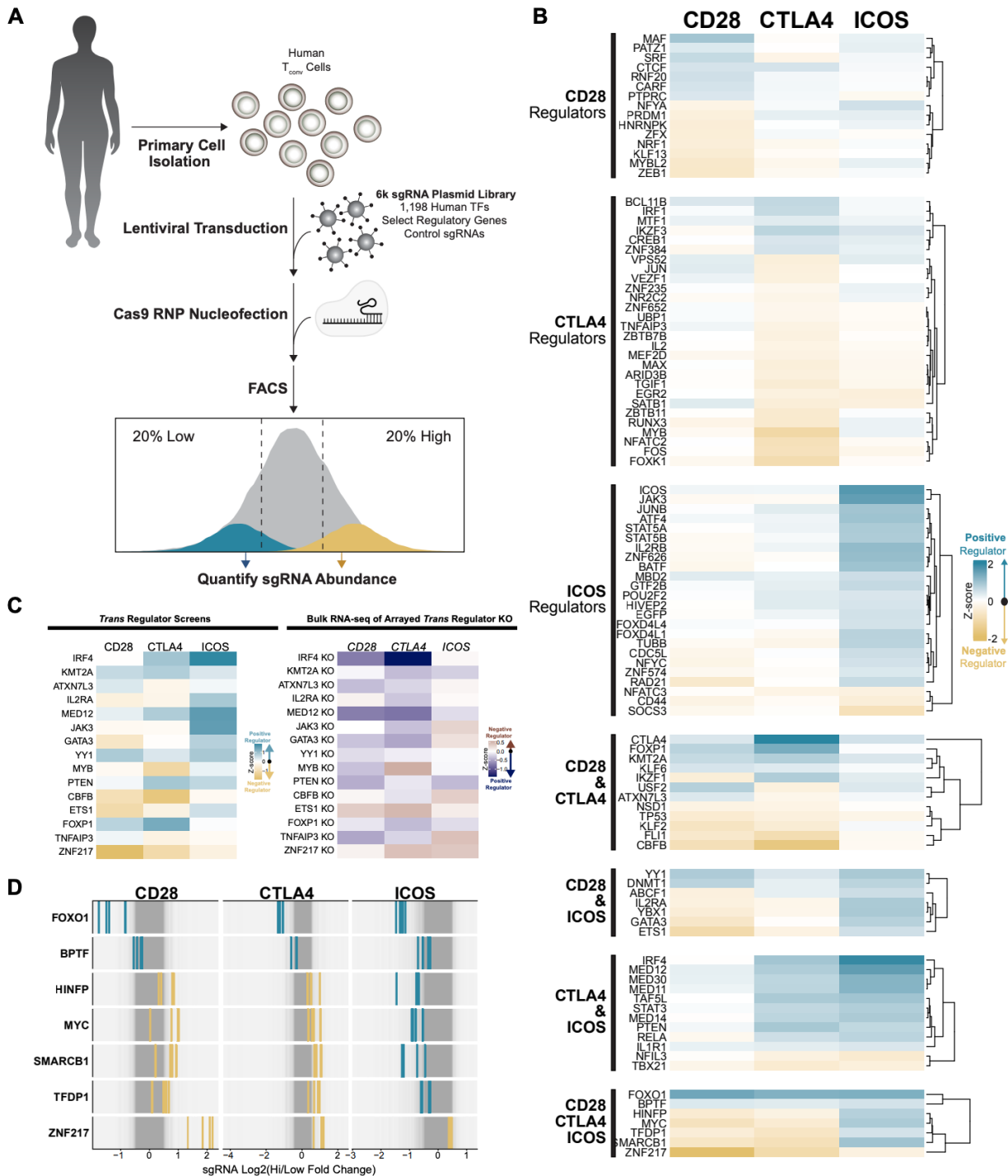
Figure S4.3: *Trans* regulator screens identify shared and unique gene regulatory modules.

A. Schematic overview of CRISPR KO screens to identify *trans* regulators of gene expression in primary human T_conv cells from two human donors. B. *Trans* regulators of one or more target gene products in the locus in primary human T_conv cells are shown. *Trans* regulators are grouped by the gene product(s) they significantly regulate (Adjusted P-value < 0.05). Blue indicates positive

regulators of gene expression, and gold indicates negative regulators. C. Effect on costimulatory genes (columns) in the setting of *trans* regulator perturbation (rows). Fill values indicate log2(fold change) enrichment from the pooled KO screen (left) or as measured by RNA-seq in the setting of arrayed *trans* regulator KO[47] (right). D. Log2(High bin/Low bin) enrichment of sgRNAs targeting the set of *trans* regulators significantly regulating all three costimulatory genes. Blue bars represent sgRNAs associated with positive *trans* regulators for each costimulatory gene, gold bars represent sgRNAs associated with negative *trans* regulators, and gray bars indicate the background sgRNA distribution.

Figure S4
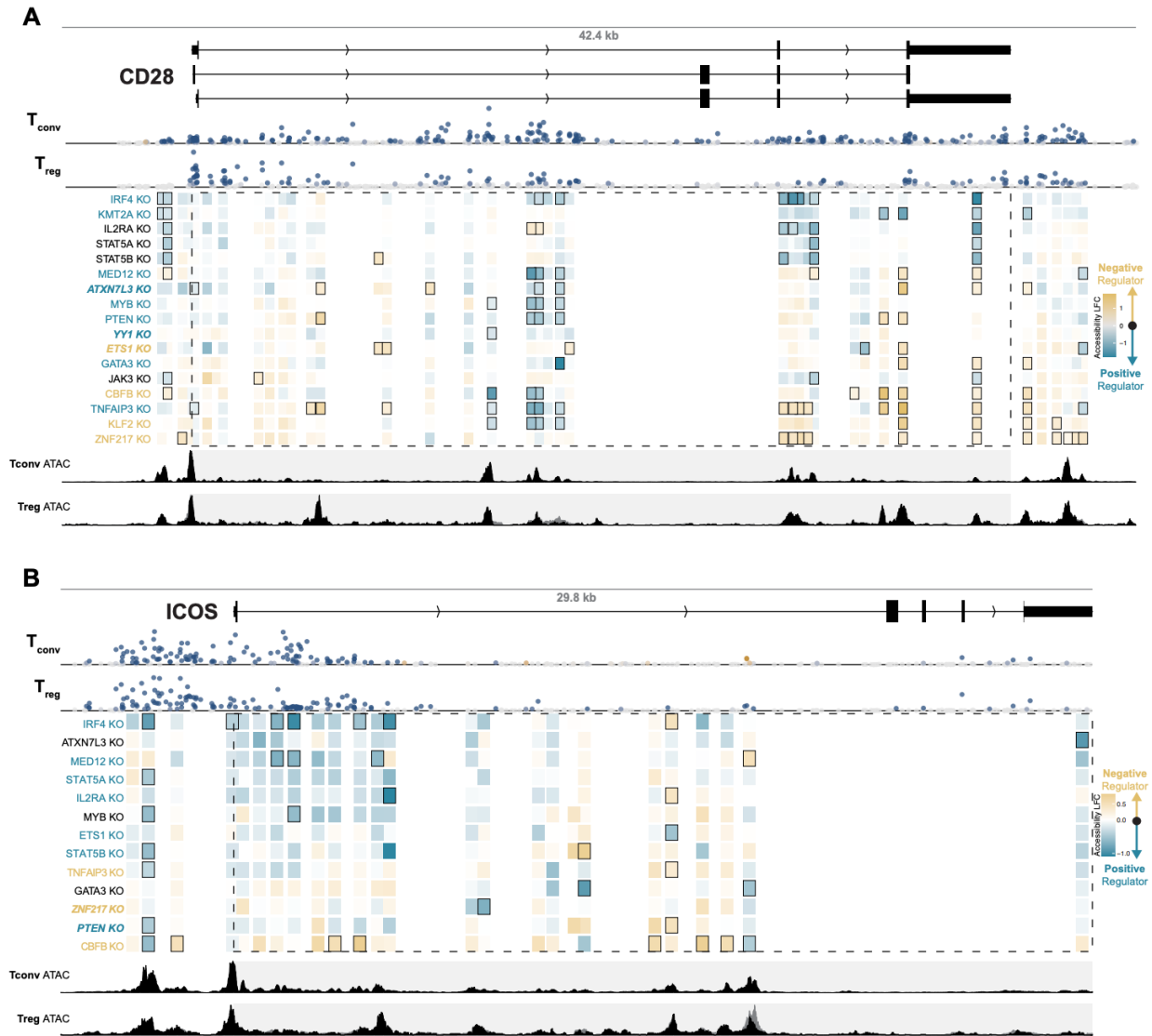
Figure S4.4: Associating *trans* regulators of CD28 and ICOS with CRISPRi-Responsive Elements via ATAC-Seq of perturbed cells.

A. CRISPRi tiling, ATAC-Seq peak accessibility changes in the setting of *trans* regulator knockout, and reference ATAC-Seq tracks for the *CD28* gene body. B. CRISPRi tiling, ATAC-Seq peak accessibility changes in the setting of *trans* regulator knockout, and reference ATAC-Seq tracks for the *CD28* gene body. For all CRISPRi tiling results, each point signifies the genomic position (x) and -log10(unadjusted P-value) (y) of the sgRNA. Blue indicates sgRNAs enriched in the lowest 20th percentile of cells, and gold indicates sgRNAs enriched in the highest 20th percentile of cells. The fill gradients indicate increasing significance of sgRNA enrichment, with maximum colors signifying Adjusted P-value < 0.05. For tile plots measuring peak accessibility changes, blue indicates positive regulation (i.e. *trans* regulator knockout decreases peak accessibility) and gold indicates negative regulation. Outlined tiles indicate significant changes in peak accessibility. Colored *trans* regulator labels indicate those significantly regulating costimulatory gene expression either positively (blue) or negatively (gold) according to either the *trans* regulator

screens or arrayed RNA-seq validation, and bolded and italicized labels have concordant significant effects between the *trans* regulator screens and arrayed RNA-seq validation.
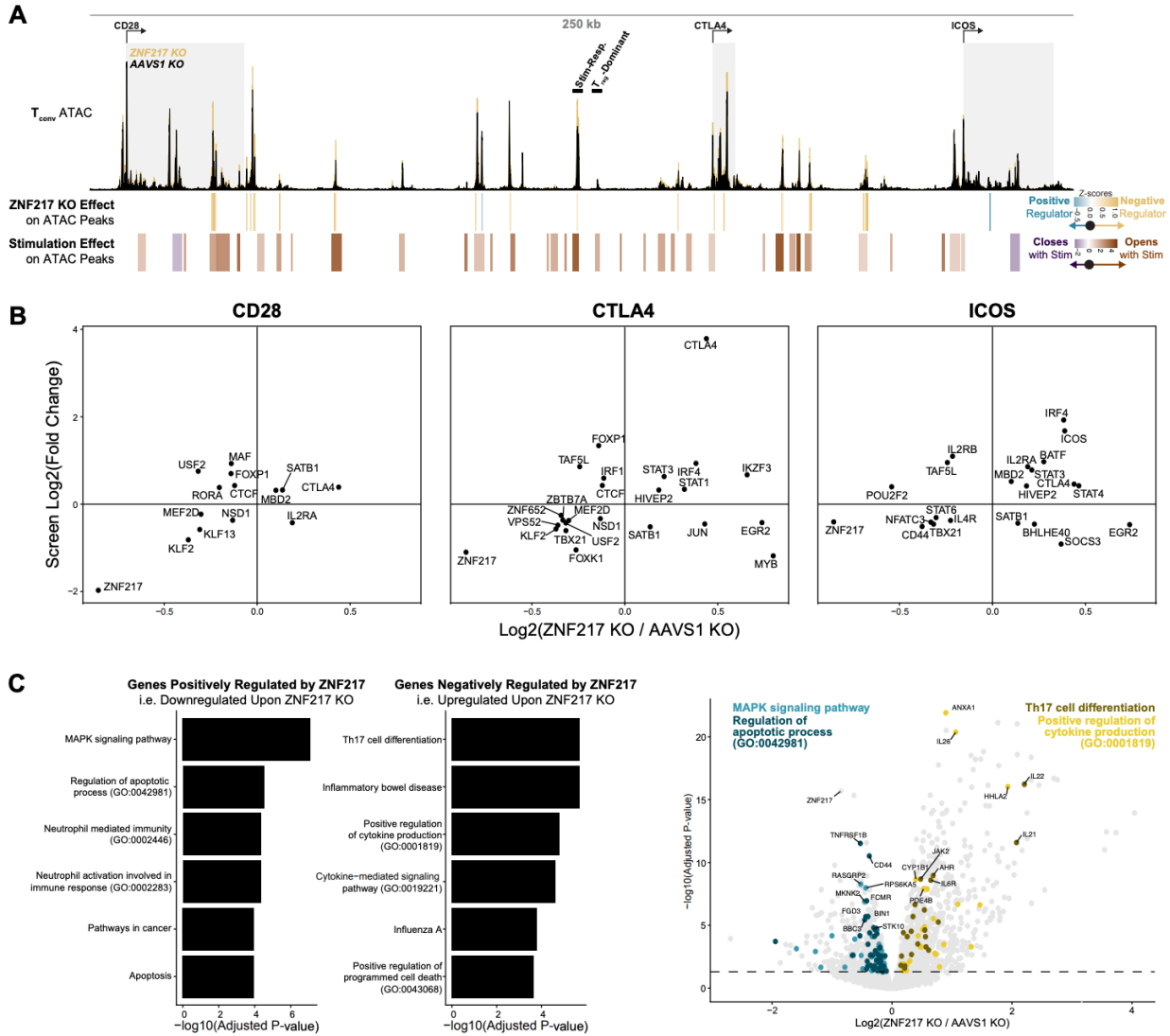
Figure S4.5: ZNF217 broadly affects gene regulatory networks acting on the costimulatory genes.
A. Top: ATAC-Seq of T_{conv} cells with either ZNF217 (yellow) or AAVS1 control (black) knockout across the entire costimulatory gene region (chr2:203696475-203967032). Costimulatory gene bodies are indicated. Middle: Bars indicate ATAC-Seq peaks that significantly gain (gold) or lose (blue) accessibility with ZNF217 KO. Bottom: Bars indicate ATAC-Seq peaks that significantly gain (red) or lose (purple) accessibility upon T cell stimulation. B. Comparison of the effect of ZNF217 knockout (FDR<0.1) on *trans* factors that regulate each costimulatory gene (FDR<0.1). C. Bar plots indicate the top three KEGG and GO terms associated with sets of genes significantly (FDR<0.05) down- (left) or up-regulated (right) by ZNF217 knockout. Volcano plot indicates gene expression changes in the setting of ZNF217 KO relative to AAVS1 controls. Down- (blue) or up-regulated (gold) genes associated with the top KEGG or GO term are colored, and the top ten most significantly altered genes associated with any KEGG or GO term are labeled. Dashed line indicates -log10(Adjusted P-value = 0.05).

Figure S6
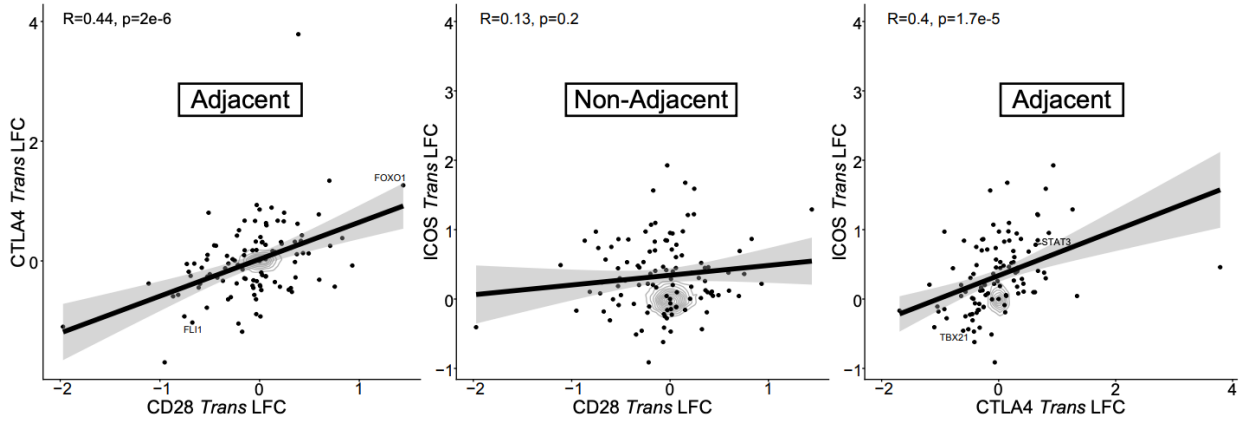
Figure S4.6: Co-regulation of *trans* factors on adjacent costimulatory genes.
Correlation of log2(fold change) of *trans* regulator effects on all costimulatory receptor pairs. Gray contour plot represents effect sizes of sgRNAs not significantly affecting the expression of any one target gene. Black points indicate *trans* regulators significantly regulating at least one costimulatory receptor. Insets include Pearson statistics. Lines indicate best fit from a general linear model.
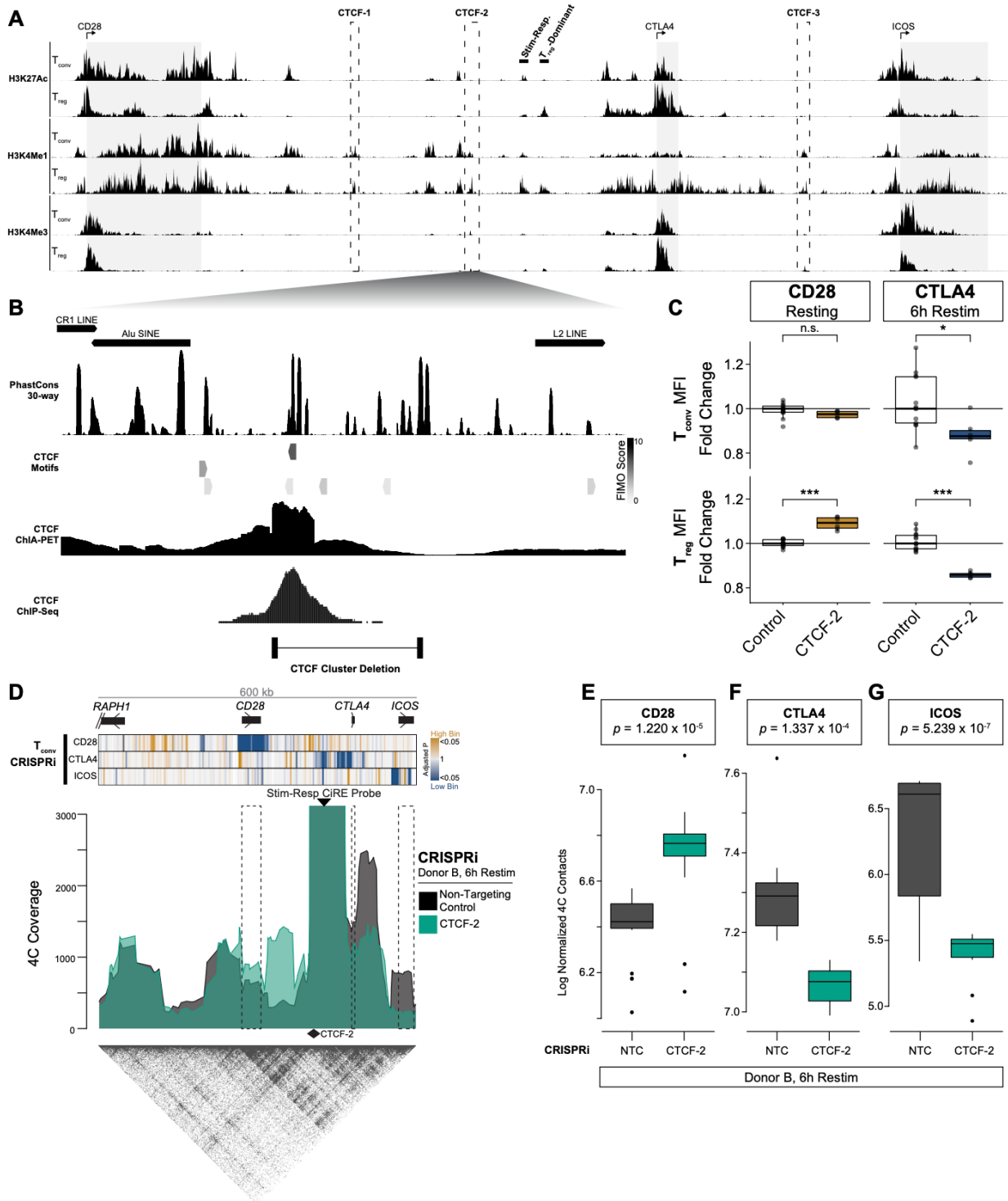
Figure S4.7: Disruption of CTCF boundary between *CD28* and *CTLA4* alters chromatin looping of stim-responsive CiRE.

A. Public H3K27ac, H3K4me1, and H3K4me3 ChIP-seq data in primary human T_{conv} (top) and T_{reg} (bottom) cells in the region plotted in Figure 4.5A. Gray bars indicate costimulatory gene bodies, and the Stim-Responsive and T_{reg}-Dominant CiREs are labeled. Dashed outlines indicate

CRISPRi-responsive elements colocalizing with CTCF ChIA-PET peaks. B. Zoomed view of region CTCF-2 region indicated in A, with track visualizations of retrotransposable elements, PhastCons 30-way conservation, CTCF motif scores and positions, 1D CTCF ChIA-PET, and CTCF ChIP-Seq. Genomic positions of sgRNAs used for CTCF Cluster excision in Figure 4.5 are plotted at bottom. C. Target protein expression in cells from two human donors after CRISPRi targeting of the CTCF-2 region (N=3 sgRNAs for all samples) outlined in A. Plotted are Median Fluorescence Intensity (MFI) values normalized to Non-Targeting Controls (N=6 sgRNAs for Donor 2 T_{conv} samples, N=7 sgRNAs for all other samples) in T_{conv} (top) and T_{reg} (bottom) cells. Significance calculated with the Student's t-test with Holm correction. For all panels: *$P < 0.05$, **$P < 0.01$, ***$P < 0.005$, n.s. Not Significant. D. Biological replicate of Figure 4.5E. 4C-seq plot for CTCF-2 CRISPRi Tconv cells from one donor, anchored on Stim-Responsive CiRE, plotting contacts in Non-Targeting Control (black) and CTCF-2 CRISPRi targeting (green) conditions. CRISPRi tiling screen results in T_{conv} cells are plotted, where each bar signifies the genomic position (x) and -log10(Adjusted P-value) (fill) of the sgRNA. Maximum colors signify Adjusted P-value < 0.05. HiC from intact CD4+ T cells[84] is shown at the bottom. Scale bar indicates genomic region that is plotted. The 4C viewpoint and CTCF-2 boundary are indicated by arrowheads. Dashed box regions indicate *CD28*, *CTLA4,* and *ICOS* (left to right) gene bodies. E. Normalized 4C signal intensity between Non-Targeting Control and CTCF-2 targeting CRISPRi groups for the *CD28* gene body. F. Normalized 4C signal intensity between Non-Targeting Control and CTCF-2 targeting CRISPRi groups for the *CTLA4* gene body. G. Normalized 4C signal intensity between Non-Targeting Control and CTCF-2 targeting CRISPRi groups for the *ICOS* gene body. For E-G, each dot represents the log-transformed 4C signal intensity of each captured genomic region in either the *CD28*, *CTLA4*, or *ICOS* gene body (see Methods).

4.7: References

1. Yan, M. *et al.* Dynamic regulatory networks of T cell trajectory dissect transcriptional control of T cell state transition. *Mol. Ther. Nucleic Acids* **26**, 1115–1129 (2021).

2. Georgescu, C. *et al.* A gene regulatory network armature for T lymphocyte specification. *Proc. Natl. Acad. Sci. U. S. A.* **105**, 20100–20105 (2008).

3. Alver, B. H. *et al.* The SWI/SNF chromatin remodelling complex is required for maintenance of lineage specific enhancers. *Nat. Commun.* **8**, 14648 (2017).

4. Jeong, S. M., Lee, C., Lee, S. K., Kim, J. & Seong, R. H. The SWI/SNF chromatin-remodeling complex modulates peripheral T cell activation and proliferation by controlling AP-1 expression. *J. Biol. Chem.* **285**, 2340–2350 (2010).

5. Sun, Y. *et al.* The mediator subunit Med23 contributes to controlling T-cell activation and prevents autoimmunity. *Nat. Commun.* **5**, 5225 (2014).

6. Hosokawa, H. & Rothenberg, E. V. How transcription factors drive choice of the T cell fate. *Nat. Rev. Immunol.* **21**, 162–176 (2021).

7. Zaugg, J. B. *et al.* Current challenges in understanding the role of enhancers in disease. *Nat. Struct. Mol. Biol.* **29**, 1148–1158 (2022).

8. Michalak, P. Coexpression, coregulation, and cofunctionality of neighboring genes in eukaryotic genomes. *Genomics* **91**, 243–248 (2008).

9. Kustatscher, G., Grabowski, P. & Rappsilber, J. Pervasive coexpression of spatially proximal genes is buffered at the protein level. *Mol. Syst. Biol.* **13**, 937 (2017).

10. Arnone, J. T., Robbins-Pianka, A., Arace, J. R., Kass-Gergi, S. & McAlear, M. A. The adjacent positioning of co-regulated gene pairs is widely conserved across eukaryotes. *BMC Genomics* **13**, 546 (2012).

11. Vogel, J. H., von Heydebreck, A., Purmann, A. & Sperling, S. Chromosomal clustering of a human transcriptome reveals regulatory background. *BMC Bioinformatics* **6**, 230 (2005).

12. Phillips-Cremins, J. E. *et al.* Architectural protein subclasses shape 3D organization of genomes during lineage commitment. *Cell* **153**, 1281–1295 (2013).

13. Dowen, J. M. *et al.* Control of cell identity genes occurs in insulated neighborhoods in mammalian chromosomes. *Cell* **159**, 374–387 (2014).

14. Matthews, B. J. & Waxman, D. J. Computational prediction of CTCF/cohesin-based intra-TAD loops that insulate chromatin contacts and gene expression in mouse liver. *Elife* **7**, (2018).

15. Beagan, J. A. & Phillips-Cremins, J. E. On the existence and functionality of topologically associating domains. *Nat. Genet.* **52**, 8–16 (2020).

16. Lupiáñez, D. G. *et al.* Disruptions of topological chromatin domains cause pathogenic rewiring of gene-enhancer interactions. *Cell* **161**, 1012–1025 (2015).

17. Hnisz, D. *et al.* Activation of proto-oncogenes by disruption of chromosome neighborhoods. *Science* **351**, 1454–1458 (2016).

18. Flavahan, W. A. *et al.* Insulator dysfunction and oncogene activation in IDH mutant gliomas. *Nature* **529**, 110–114 (2016).

19. Sekimata, M. *et al.* CCCTC-binding factor and the transcription factor T-bet orchestrate T helper 1 cell-specific structure and function at the interferon-gamma locus. *Immunity* **31**, 551–564 (2009).

20. Shih, H.-Y. *et al.* A critical CTCF binding site of the Ifng-Il22 locus specifies cytokine expression and finetunes immune response. *The Journal of Immunology* **206**, 53.13–53.13 (2021).

21. Xavier, R. J. & Rioux, J. D. Genome-wide association studies: a new window into immune-mediated diseases. *Nat. Rev. Immunol.* **8**, 631–643 (2008).

22. Bernard, D. *et al.* Costimulatory receptors in jawed vertebrates: conserved CD28, odd CTLA4 and multiple BTLAs. *Dev. Comp. Immunol.* **31**, 255–271 (2007).

23. Ling, V. *et al.* Assembly and annotation of human chromosome 2q33 sequence containing the CD28, CTLA4, and ICOS gene cluster: analysis by computational, comparative, and

microarray approaches. *Genomics* **78**, 155–168 (2001).

24. Riley, J. L. & June, C. H. The CD28 family: a T-cell rheostat for therapeutic control of T-cell activation. *Blood* **105**, 13–21 (2005).

25. Glinos, D. A. *et al.* Genomic profiling of T-cell activation suggests increased sensitivity of memory T cells to CD28 costimulation. *Genes Immun.* **21**, 390–408 (2020).

26. Chen, L. & Flies, D. B. Molecular mechanisms of T cell co-stimulation and co-inhibition. *Nat. Rev. Immunol.* **13**, 227–242 (2013).

27. Walker, L. S. K. Treg and CTLA-4: two intertwining pathways to immune tolerance. *J. Autoimmun.* **45**, 49–57 (2013).

28. Li, D.-Y. & Xiong, X.-Z. ICOS+ Tregs: A Functional Subset of Tregs in Immune Diseases. *Front. Immunol.* **11**, 2104 (2020).

29. Jogdand, G. M., Mohanty, S. & Devadas, S. Regulators of Tfh Cell Differentiation. *Front. Immunol.* **7**, 520 (2016).

30. Okada, Y. *et al.* Genetics of rheumatoid arthritis contributes to biology and drug discovery. *Nature* **506**, 376–381 (2014).

31. Ueda, H. *et al.* Association of the T-cell regulatory gene CTLA4 with susceptibility to autoimmune disease. *Nature* **423**, 506–511 (2003).

32. Hodi, F. S. *et al.* Improved survival with ipilimumab in patients with metastatic melanoma. *N. Engl. J. Med.* **363**, 711–723 (2010).

33. Robert, C. *et al.* Ipilimumab plus dacarbazine for previously untreated metastatic melanoma. *N. Engl. J. Med.* **364**, 2517–2526 (2011).

34. Edner, N. M., Carlesso, G., Rush, J. S. & Walker, L. S. K. Targeting co-stimulatory molecules in autoimmune disease. *Nat. Rev. Drug Discov.* **19**, 860–883 (2020).

35. Adams, A. B., Ford, M. L. & Larsen, C. P. Costimulation Blockade in Autoimmunity and Transplantation: The CD28 Pathway. *J. Immunol.* **197**, 2045–2050 (2016).

36. Hardison, R. C. & Taylor, J. Genomic approaches towards finding cis-regulatory modules in

animals. *Nat. Rev. Genet.* **13**, 469–483 (2012).

37. Yazar, S. *et al.* Single-cell eQTL mapping identifies cell type-specific genetic control of autoimmune disease. *Science* **376**, eabf3041 (2022).

38. Perez, R. K. *et al.* Single-cell RNA-seq reveals cell type–specific molecular and genetic associations to lupus. *Science* **376**, Art. No. abf1970 (2022).

39. Nathan, A. *et al.* Single-cell eQTL models reveal dynamic T cell state dependence of disease loci. *Nature* (2022) doi:10.1038/s41586-022-04713-1.

40. Arvey, A. *et al.* Genetic and epigenetic variation in the lineage specification of regulatory T cells. *Elife* **4**, e07571 (2015).

41. Ohkura, N. *et al.* Regulatory T Cell-Specific Epigenomic Region Variants Are a Key Determinant of Susceptibility to Common Autoimmune Diseases. *Immunity* **52**, 1119–1132.e4 (2020).

42. Butty, V. *et al.* Signatures of strong population differentiation shape extended haplotypes across the human CD28, CTLA4, and ICOS costimulatory genes. *Proc. Natl. Acad. Sci. U. S. A.* **104**, 570–575 (2007).

43. Shifrut, E. *et al.* Genome-wide CRISPR Screens in Primary Human T Cells Reveal Key Regulators of Immune Function. doi:10.1101/384776.

44. Ting, P. Y. *et al.* Guide Swap enables genome-scale pooled CRISPR-Cas9 screening in human primary cells. *Nat. Methods* **15**, 941–946 (2018).

45. Parnas, O. *et al.* A Genome-wide CRISPR Screen in Primary Immune Cells to Dissect Regulatory Networks. *Cell* **162**, 675–686 (2015).

46. Schmidt, R. *et al.* CRISPR activation and interference screens decode stimulation responses in primary human T cells. *Science* **375**, eabj4008 (2022).

47. Freimer, J. W. *et al.* Systematic discovery and perturbation of regulatory genes in human T cells reveals the architecture of immune networks. *Nat. Genet.* (2022) doi:10.1038/s41588-022-01106-y.

48. Ye, L. *et al.* A genome-scale gain-of-function CRISPR screen in CD8 T cells identifies proline metabolism as a means to enhance CAR-T therapy. *Cell Metab.* **34**, 595–614.e14 (2022).

49. Wang, D. *et al.* CRISPR Screening of CAR T Cells and Cancer Stem Cells Reveals Critical Dependencies for Cell-Based Therapies. *Cancer Discov.* **11**, 1192–1211 (2021).

50. Crowther, M. D. *et al.* Genome-wide CRISPR-Cas9 screening reveals ubiquitous T cell cancer targeting via the monomorphic MHC class I-related protein MR1. *Nat. Immunol.* **21**, 178–185 (2020).

51. Wei, J. *et al.* Targeting REGNASE-1 programs long-lived effector T cells for cancer therapy. *Nature* **576**, 471–476 (2019).

52. Simeonov, D. R. *et al.* Discovery of stimulation-responsive immune enhancers with CRISPR activation. *Nature* **549**, 111–115 (2017).

53. Tarjan, D. R., Flavahan, W. A. & Bernstein, B. E. Epigenome editing strategies for the functional annotation of CTCF insulators. *Nat. Commun.* **10**, 4258 (2019).

54. Fulco, C. P. *et al.* Systematic mapping of functional enhancer-promoter connections with CRISPR interference. *Science* **354**, 769–773 (2016).

55. Ahmed, M. *et al.* CRISPRi screens reveal a DNA methylation-mediated 3D genome dependent causal mechanism in prostate cancer. *Nat. Commun.* **12**, 1781 (2021).

56. Fulco, C. P. *et al.* Activity-by-contact model of enhancer-promoter regulation from thousands of CRISPR perturbations. *Nat. Genet.* **51**, 1664–1669 (2019).

57. Rao, S. S. P. *et al.* A 3D map of the human genome at kilobase resolution reveals principles of chromatin looping. *Cell* **159**, 1665–1680 (2014).

58. Alerasool, N., Segal, D., Lee, H. & Taipale, M. An efficient KRAB domain for CRISPRi applications in human cells. *Nat. Methods* **17**, 1093–1096 (2020).

59. Rose, A. B. Introns as Gene Regulators: A Brick on the Accelerator. *Front. Genet.* **9**, 672 (2018).

60. Mellado, M. *et al.* T Cell Migration in Rheumatoid Arthritis. *Front. Immunol.* **6**, 384 (2015).

61. Cope, A. P. T cells in rheumatoid arthritis. *Arthritis Res. Ther.* **10 Suppl 1**, S1 (2008).

62. Genovese, M. C. *et al.* Abatacept for rheumatoid arthritis refractory to tumor necrosis factor alpha inhibition. *N. Engl. J. Med.* **353**, 1114–1123 (2005).

63. Oh, H. & Ghosh, S. NF-κB: roles and regulation in different CD4(+) T-cell subsets. *Immunol. Rev.* **252**, 41–51 (2013).

64. Huber, M. & Lohoff, M. IRF4 at the crossroads of effector T-cell fate decision. *Eur. J. Immunol.* **44**, 1886–1895 (2014).

65. Cohen, P. A., Donini, C. F., Nguyen, N. T., Lincet, H. & Vendrell, J. A. The dark side of ZNF217, a key regulator of tumorigenesis with powerful biomarker value. *Oncotarget* **6**, 41566–41581 (2015).

66. Lee, D.-F., Walsh, M. J. & Aguiló, F. ZNF217/ZFP217 Meets Chromatin and RNA. *Trends Biochem. Sci.* **41**, 986–988 (2016).

67. ENCODE Project Consortium. An integrated encyclopedia of DNA elements in the human genome. *Nature* **489**, 57–74 (2012).

68. Schmidt, D. *et al.* Waves of retrotransposon expansion remodel genome organization and CTCF binding in multiple mammalian lineages. *Cell* **148**, 335–348 (2012).

69. Blobel, G. A., Higgs, D. R., Mitchell, J. A., Notani, D. & Young, R. A. Testing the super-enhancer concept. *Nat. Rev. Genet.* **22**, 749–755 (2021).

70. Zhang, F. & Lupski, J. R. Non-coding genetic variants in human disease. *Hum. Mol. Genet.* **24**, R102–10 (2015).

71. Villar, D. *et al.* Enhancer evolution across 20 mammalian species. *Cell* **160**, 554–566 (2015).

72. Keir, M. E. & Sharpe, A. H. The B7/CD28 costimulatory family in autoimmunity. *Immunol. Rev.* **204**, 128–143 (2005).

73. Gough, S. C. L., Walker, L. S. K. & Sansom, D. M. CTLA4 gene polymorphism and autoimmunity. *Immunol. Rev.* **204**, 102–115 (2005).

74. Chang, L.-H., Ghosh, S. & Noordermeer, D. TADs and Their Borders: Free Movement or

Building a Wall? *J. Mol. Biol.* **432**, 643–652 (2020).

75. Cho, S. W. *et al.* Promoter of lncRNA Gene PVT1 Is a Tumor-Suppressor DNA Boundary Element. *Cell* **173**, 1398–1412.e22 (2018).

76. Shearwin, K. E., Callen, B. P. & Egan, J. B. Transcriptional interference–a crash course. *Trends Genet.* **21**, 339–345 (2005).

77. Mazo, A., Hodgson, J. W., Petruk, S., Sedkov, Y. & Brock, H. W. Transcriptional interference: an unexpected layer of complexity in gene regulation. *J. Cell Sci.* **120**, 2755–2761 (2007).

78. Adhya, S. & Gottesman, M. Promoter occlusion: transcription through a promoter may inhibit its activity. *Cell* **29**, 939–944 (1982).

79. Palmer, A. C., Ahlgren-Berg, A., Egan, J. B., Dodd, I. B. & Shearwin, K. E. Potent transcriptional interference by pausing of RNA polymerases over a downstream promoter. *Mol. Cell* **34**, 545–555 (2009).

80. Buetti-Dinh, A. *et al.* Control and signal processing by transcriptional interference. *Mol. Syst. Biol.* **5**, 300 (2009).

81. Lee, T. J., Parikh, R. Y., Weitz, J. S. & Kim, H. D. Suppression of expression between adjacent genes within heterologous modules in yeast. *G3* **4**, 109–116 (2014).

82. Abarrategui, I. & Krangel, M. S. Noncoding transcription controls downstream promoters to regulate T-cell receptor alpha recombination. *EMBO J.* **26**, 4380–4390 (2007).

83. O'Neill, R. E. & Cao, X. Co-stimulatory and co-inhibitory pathways in cancer immunotherapy. *Adv. Cancer Res.* **143**, 145–194 (2019).

84. Sloan, C. A. *et al.* ENCODE data at the ENCODE portal. *Nucleic Acids Res.* **44**, D726–32 (2016).

85. Dixon, J. R. *et al.* Topological domains in mammalian genomes identified by analysis of chromatin interactions. *Nature* **485**, 376–380 (2012).

86. Horlbeck, M. A. *et al.* Nucleosomes impede Cas9 access to DNA in vivo and in vitro. *Elife* **5**, (2016).

87. Joung, J. *et al.* Genome-scale CRISPR-Cas9 knockout and transcriptional activation screening. *Nat. Protoc.* **12**, 828–863 (2017).

88. Li, W. *et al.* MAGeCK enables robust identification of essential genes from genome-scale CRISPR/Cas9 knockout screens. *Genome Biol.* **15**, 554 (2014).

89. Love, M. I., Huber, W. & Anders, S. Moderated estimation of fold change and dispersion for RNA-seq data with DESeq2. *Genome Biol.* **15**, 550 (2014).

90. Krijger, P. H. L., Geeven, G., Bianchi, V., Hilvering, C. R. E. & de Laat, W. 4C-seq from beginning to end: A detailed protocol for sample preparation and data analysis. *Methods* **170**, 17–32 (2020).

91. Phanstiel, D. H., Boyle, A. P., Araya, C. L. & Snyder, M. P. Sushi.R: flexible, quantitative and integrative genomic visualizations for publication-quality multi-panel figures. *Bioinformatics* **30**, 2808–2810 (2014).

92. Wang, Y. *et al.* The 3D Genome Browser: a web-based browser for visualizing 3D genome organization and long-range chromatin interactions. *Genome Biol.* **19**, 151 (2018).

93. Calderon, D. *et al.* Landscape of stimulation-responsive chromatin across diverse human immune cells. *Nat. Genet.* **51**, 1494–1505 (2019).

94. Perez, R. K. *et al.* Single-cell RNA-seq reveals cell type-specific molecular and genetic associations to lupus. *Science* **376**, eabf1970 (2022).

95. Schmiedel, B. J. *et al.* Impact of Genetic Polymorphisms on Human Immune Cell Gene Expression. *Cell* **175**, 1701–1715.e16 (2018).

96. Schmidl, C. *et al.* The enhancer and promoter landscape of human regulatory and conventional T-cell subpopulations. *Blood* **123**, e68–78 (2014).

97. Tarbell, E. *et al.* CD4+ T cells from children with active juvenile idiopathic arthritis show altered chromatin features associated with transcriptional abnormalities. *Sci. Rep.* **11**, 4011 (2021).

Chapter 5: Conclusion, Future Directions, and Closing Remarks

As stated in **Chapter 1**, the most impactful scientific projects answer some questions but uncover countless others. Consequently, new methods must be developed concomitantly to meet the ever-expanding set of opportunities to better understand the biological world. Fortunately for immunologists, novel analytical methods are often pioneered first in immune cells, primarily due to their ready accessibility and relatively simple culture *in vitro*. Just as flow cytometry was adapted from early immunological studies to examinations of countless other cell types[1], immunologists will likely continue to access emerging molecular and cellular analytical tools first.

5.1: Characterizing the immune system at single cell resolution.

Of the recent innovations, few have impacted the scientific landscape as much as droplet-based single cell sequencing technologies. The first single cell technologies to examine RNA transcriptomes were reported less than a decade ago[2], but they have quickly taken hold of the field. They have imparted unprecedented opportunity to finely characterize cellular heterogeneity in transcriptional[3], chromatin accessibility[4], mitochondrial[5], and other[6] forms. Moreover, these methods can be paired with perturbational screens (like that outlined in **Chapter 4**) to provide a richer phenotypic readout of the effects of experimental variables[7]. Complementarily, single cell analyses will be indispensable for extracting more information from natural experiments like population genetic variation[8]. I look forward to continuing contributing to efforts to employ single cell methods to better characterize complex biological processes[9,10].

Whereas droplet-based single cell sequencing technologies can capture the genotypic and/or phenotypic heterogeneity within a mixed cellular suspension, one must consider how such heterogeneity is distributed within tissue contexts. Understanding the different types of immune cells in the tumor microenvironment is one thing; characterizing how these different cells are distributed around or within the tumor is another thing entirely. Recently, droplet-based single cell methods have been complemented by emerging technologies to spatially-characterize biological

processes[11]. There are exciting opportunities to coopt these spatial profiling methods for forward genetic screening, providing a more sophisticated lens into the biological effects of specific perturbations[12].

5.2: Meeting the expanding analytical burden

Technological innovation and commercialization are driving down costs of next-generation sequencing and (spatial) single cell profiling methods, but the increasing prevalence of such data-rich scientific approaches will significantly increase the amount of data scientists need to sift through for biological insights[13]. Fortunately, new computational abilities are conferring previously untold power to uncover novel scientific insights from (once prohibitively) large datasets, including the co-development of hardware[14] and associated computing infrastructure that underlies recent advances in machine learning (ML) and artificial intelligence (AI). These methods are now being applied to a wide array of scientific arenas, from diagnostics (as shared in **Chapter 3**) to drug discovery[15]. In genomics[16], these powerful new analytical approaches will aid our transition from a linear understanding of biology to a more complex, non-linear one.

To these ends, ML methods have already made inroads in perturbational single cell screen analyses[17]. Similarly, these tools will be critical to better understand the complexities of gene regulation[18] as tackled in **Chapter 4**. Importantly, these computational models are only as good as the training data fed into them. Thus, functional genomic studies like that in **Chapter 4** will be important to train models for identification of *cis*-regulatory elements, inference of effects of genetic variants, and the like. Thus, functional genomics and computational biology will be mutually reliant on one another moving forward, each providing the other with the capacity to garner biological insights and ultimately inform the next generation of biomedicine.

5.3: References

1. Herzenberg, L. A. *et al.* The history and future of the fluorescence activated cell sorter and flow cytometry: a view from Stanford. *Clin. Chem.* **48**, 1819–1827 (2002).

2. Macosko, E. Z. *et al.* Highly Parallel Genome-wide Expression Profiling of Individual Cells Using Nanoliter Droplets. *Cell* **161**, 1202–1214 (2015).

3. Haque, A., Engel, J., Teichmann, S. A. & Lönnberg, T. A practical guide to single-cell RNA-sequencing for biomedical research and clinical applications. *Genome Med.* **9**, 75 (2017).

4. Buenrostro, J. D. *et al.* Single-cell chromatin accessibility reveals principles of regulatory variation. *Nature* **523**, 486–490 (2015).

5. Lareau, C. A. *et al.* Massively parallel single-cell mitochondrial DNA genotyping and chromatin profiling. *Nat. Biotechnol.* **39**, 451–461 (2021).

6. Lee, J., Hyeon, D. Y. & Hwang, D. Single-cell multiomics: technologies and data analysis methods. *Exp. Mol. Med.* **52**, 1428–1442 (2020).

7. Bock, C. *et al.* High-content CRISPR screening. *Nature Reviews Methods Primers* **2**, 1–23 (2022).

8. Cano-Gamez, E. & Trynka, G. From GWAS to Function: Using Functional Genomics to Identify the Mechanisms Underlying Complex Diseases. *Front. Genet.* **11**, 424 (2020).

9. Roth, T. L. *et al.* Pooled Knockin Targeting for Genome Engineering of Cellular Immunotherapies. *Cell* **181**, 728–744.e21 (2020).

10. Bapat, S. P. *et al.* Obesity alters pathology and treatment response in inflammatory disease. *Nature* **604**, 337–342 (2022).

11. Rao, A., Barkley, D., França, G. S. & Yanai, I. Exploring tissue architecture using spatial transcriptomics. *Nature* **596**, 211–220 (2021).

12. Teng, K. & Jackson, H. W. Genetic perturbations go spatial. *Cell Genom* **2**, 100120 (2022).

13. Muir, P. *et al.* The real cost of sequencing: scaling computation to keep pace with data generation. *Genome Biol.* **17**, 53 (2016).

14. Stone, J. E. *et al.* Accelerating molecular modeling applications with graphics processors. *J. Comput. Chem.* **28**, 2618–2640 (2007).

15. Pandey, M. *et al.* The transformational role of GPU computing and deep learning in drug discovery. *Nature Machine Intelligence* **4**, 211–221 (2022).

16. Libbrecht, M. W. & Noble, W. S. Machine learning applications in genetics and genomics. *Nat. Rev. Genet.* **16**, 321–332 (2015).

17. Norman, T. M. *et al.* Exploring genetic interaction manifolds constructed from rich single-cell phenotypes. *Science* **365**, 786–793 (2019).

18. Telenti, A., Lippert, C., Chang, P.-C. & DePristo, M. Deep learning of genomic variation and regulatory network data. *Hum. Mol. Genet.* **27**, R63–R71 (2018).

Publishing Agreement

It is the policy of the University to encourage open access and broad distribution of all theses, dissertations, and manuscripts. The Graduate Division will facilitate the distribution of UCSF theses, dissertations, and manuscripts to the UCSF Library for open access and distribution. UCSF will make such theses, dissertations, and manuscripts accessible to the public and will take reasonable steps to preserve these works in perpetuity.

I hereby grant the non-exclusive, perpetual right to The Regents of the University of California to reproduce, publicly display, distribute, preserve, and publish copies of my thesis, dissertation, or manuscript in any form or media, now existing or later derived, including access online for teaching, research, and public service purposes.

DocuSigned by:

Cody Mowery

62CA7AB636E643F...   Author Signature

3/19/2023

Date